Université de Montréal

Characterization of P3HT:thermoplastic blends prepared *via* direct-ink writing

Par

Myles Creran

Département de chimie, Faculté des arts et des sciences

Mémoire présenté en vue de l'obtention du grade de

M.Sc. en chimie

Décembre 2023

Université de Montréal

Département de chimie, Faculté des arts et des sciences

Ce mémoire intitulé

Characterization of P3HT:thermoplastic blends prepared *via* direct-ink writing

Présenté par

Myles Creran

A été évalué par un jury composé des personnes suivantes

Christian Pellerin
Président-rapporteur

Audrey Laventure
Directrice de recherche

Geraldine Bazuin
Membre du jury

Résumé

Les dispositifs optoélectroniques sont devenus un élément essentiel de la technologie moderne visant à exploiter des applications de niche pour l'électronique flexible à base de composés organiques. Jusqu'à présent, les films minces préparés à partir de composés polymères conjugués ont été les principaux concurrents pour les dispositifs optoélectroniques organiques. Avec l'apparition de nouvelles méthodes de mise en œuvre et de nouveaux besoins électroniques, les méthodes de fabrication additive des matériaux optoélectroniques suscitent de plus en plus d'intérêt. Malgré l'intérêt croissant et la variété des méthodes de mise en œuvre tridimensionnelles, on comprend encore mal l'impact de la technique de mise en œuvre sur l'organisation moléculaire des échantillons. Ici, une étude est présentée impliquant l'impression 3D assistée par évaporation de solvant et le poly(3-hexylthiophène) (P3HT) qui est bien décrit dans la littérature, et, dans ce cas-ci, mélangé à diverses matrices thermoplastiques.

Dans un premier temps, les matrices thermoplastiques employées, i.e. le polystyrène (PS), le polypropylène carbonate (PPC), le polyméthacrylate de méthyle (PMMA) et le polyoxyéthylène (PEO) sont évaluées en fonction de leurs propriétés rhéologiques et de leur imprimabilité en 3D, qui ne sont que très peu affectées par l'introduction du P3HT. Par la suite, le P3HT à régiorégularité élevée et faible est mélangé dans chacune des matrices thermoplastiques. L'organisation moléculaire des deux composantes dans les architectures imprimées a été évaluée par des techniques de spectroscopie UV-visible et de fluorescence. Les phases en présence ont été analysées à l'aide d'analyse calorimétrique différentielle à balayage, de microscopie optique polarisée et de diffraction des rayons X, ce qui a également permis d'analyser l'état d'agrégation du P3HT par rapport à celui retrouvé dans les films minces. Il est intéressant de noter que les propriétés optiques montrent peu ou pas de différence entre les architectures 3D et les films minces, ce qui indique vraisemblablement que l'efficacité d'un dispositif optoélectronique imprimé en 3D ne serait pas affectée par l'impression 3D assistée par évaporation de solvant. Cette étude pourrait permettre de mieux comprendre comment il serait possible de mettre au point des dispositifs optoélectroniques, y compris des photoconducteurs, des photovoltaïques

organiques, des transistors à effet de champ organiques, etc. à l'aide de techniques de fabrication additive, ce qui ouvrira la voie à une nouvelle ère en électronique organique imprimée en trois dimensions.

Mots-clés : Mélanges de polymères, optoélectronique, P3HT, thermoplastique, fabrication additive, impression 3D assistée par évaporation de solvant

Abstract

Optoelectronic devices have become a staple in modern day technology which aims to transition to flexible electronics that are developed from organic compounds. To date, 2-dimensional films of conjugated polymer compounds have been the main contender for organic optoelectronic devices. As new processing methods and electronic needs become present in the modern day, a focus on 3-dimensional processing methods of optoelectronic materials have become increasingly of interest. With the increasing interest and variety of 3-dimensional processing methods, there is little understanding of how the processing technique molecularly affects the final product. Herein is presented a study on the extrusion-based, direct-ink writing of the well understood poly(3-hexylthiophene-2,5-diyl) (P3HT) blended into a variety of thermoplastic matrices.

Initially the pristine thermoplastics of polystyrene (PS), poly(propylene carbonate) (PPC), poly(methyl methacrylate) (PMMA), and poly(ethylene oxide) (PEO) were evaluated based on their rheological and printable properties which are negligibly affected by the introduction of P3HT. Subsequently, after the blending of both high and low regioregular P3HT into each of the thermoplastic matrices, the printed architectures were further analyzed by X-Ray diffraction, UV-vis, and fluorescence techniques to assess the aggregation state of P3HT in comparison to 2-dimensional processed films. Interestingly, the electronic properties show little to no difference between 3-dimensional architectures and 2-dimensional films, which presumably indicates that the efficiency would not be affected by the direct-ink writing technique. This study could contribute to the beginning of producing optoelectronic devices, including photoconductors, organic photovoltaic and organic field effect transistors, in 3-dimensions resulting in a new age of electronics.

Keywords : Polymer blends, Optoelectronic, P3HT, Thermoplastic, 3D printing, Direct-ink writing

Table of Content

List of Tables

List of Figures

List of Abbreviations

AM: Additive manufacturing

CAD: Computer aided design

DIW: Direct-ink writing

DSC: Differential scanning calorimetry

G-code: Geometric code

GISAXS: Grazing incidence small angle X-ray scattering

GIWAXS: Grazing incidence wide angle X-ray scattering

HR: High regioregular

LR: Low regioregular

OLED: Organic light-emitting diodes

OFET: Organic field-effect transistors

OPV: Organic photovoltaics

P3HT: Poly(3-hexylthiophene-2,5-diyl)

PEO: Poly(ethylene oxide)

PMMA: Poly(methyl methacrylate)

PPC: Poly(propylene carbonate)

PS: Polystyrene

rr: regioregular

rra: regiorandom

XRD: X-ray diffraction

For Marlene Kunderman and Jazzmine Creran

Acknowledgements

To begin, there are many people that I appreciate and would like to acknowledge as without them, my progress in science would not be possible. First, to my supervisor, Audrey Laventure, and Nicolas Macia, thank you for supporting me through this adventure. Despite my difficulties being anglophone at a purely French institution, you both were always there for me whether it was for scientific concerns or my own personal problems. I'd also like to thank all of the Laventure group members that worked alongside me during my stay at U de M. Additionally, I would like to acknowledge the entire staff of Ye Olde Orchard Pub & Grill on Prince Arthur who always made me feel welcome as I wrote the majority of this thesis there. To Mr. Dutchak—my grade 10 mathematics teacher, you gave me a 7% on my first algebra exam where you announced my grade in front of numerous of my classmates—look at me now! As this may seem sarcastic, failure is a part of the journey which was taught to me from my baseball career to date. I genuinely wish I could name every player that I had the privilege of being on the diamond with at both the University of Calgary Dinos and at the Université de Montréal Carabins teams. But the list of these teammates may be too large for the acceptance of this thesis. Please know that each one of you hold a place in my heart. Specifically, there are two of my baseball coaches from the University of Calgary where I wish to have their names imbedded in this thesis for the future to come. To Geoff Freeborn and Drew Miller, you gave me chances and believed in me during times I couldn't even believe in myself and for that, I will never forget and will always love you both. To all of my friends and family, I love you and could not have achieved this without you. There are a few more names which I would like to specifically outline here. To Aiden Schreuder and Ryan Engbrecht—you both visited me numerous times in Montreal which gave me a taste of home resulting in our own personal holiday (Sendmas)—I love you guys. To Kaden Rideout, you'll never understand how much I appreciate your artistic enthusiasm when I get to see you—I love you buddy. I also would like to mention Hayley Cleveland—you were there for me amongst the hardest of times, and I will never forget that—thank you so much; you will always be loved and appreciated. To all of the aforementioned and more, as I move through my career in science, you will not be forgotten.

Chapter 1 – Introduction

1.1 Conjugated Polymers

Over the last 50 years, conjugated polymers—despite being considered "niche" materials waiting patiently for widespread implementation—have gathered widespread interest in research and development among many cross-disciplines in fields that reach out to chemistry.[1–4] Conjugated polymers are organic macromolecules that are constructed from a backbone containing unsaturated, π-character building blocks which promote electron delocalization.[1,5–8] The delocalization of electrons in the π-character of these macromolecules are their key feature, granting the allowance of electron mobilization when a bias is applied. This implies that these materials can be opto-electronically active, which upon exposure to certain wavelengths of light can transport or store charges.[1] This unique feature of semi-conductors indicates that conjugated polymer materials may be used as the photoactive layer in a variety of optoelectronic devices which include, but are not limited to, organic light-emitting diodes (OLEDs), organic photovoltaics (OPVs) and organic field-effect transistors (OFETs).[1,2,4,9]

The aforementioned organic electronic devices are of great importance as the desire for environmentally friendly and energy-efficient sources has never been greater.[10] Organic conjugated polymers, which can display semiconducting attributes, may potentially be one of the answers to the environmental-energy crisis since they could limit the use of non-renewable materials currently used as semi-conductors. Semi-conductors are materials considered being between a conductor and an insulator. These materials are defined by their shallow band gaps which can be tuned, in the case of organic semiconductors, by chemical modification. In contrast, conductive and insulating materials are defined by possessing no such band gap or a large gap, respectively (Figure 1). Said organic materials also offer the additional contribution of being relatively inexpensive compared to their inorganic counterparts as well as demonstrating elementary processability, with or without potentially harmful solvents.[10]

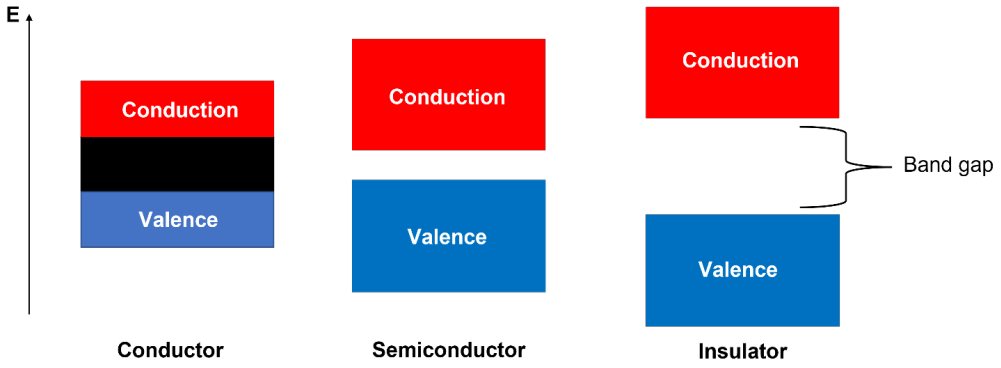

Figure 1. Visual description of the differences between conductors, semiconductors, and insulators.

The efforts to implement polymers into electronic devices can be traced back to the metal-semiconductor-metal (MSM) architecture used as a thin film diode, first described in 1987.[6] From these initial studies, the physical description of polymers as semiconductors was put together (Figure 2). The working principle from the rudimentary description of the polymeric semiconductor is as follows: The initial absorption of a photon leads to the promotion of an electron existing in the valence band (π-band) into the conduction band (π*-band), thus resulting in mobile electrons and electron holes. The emphasis is then put on "mobile" which leads to the occurrence of the physical phenomena of transportation of charge carriers, also known as conductivity.[6]

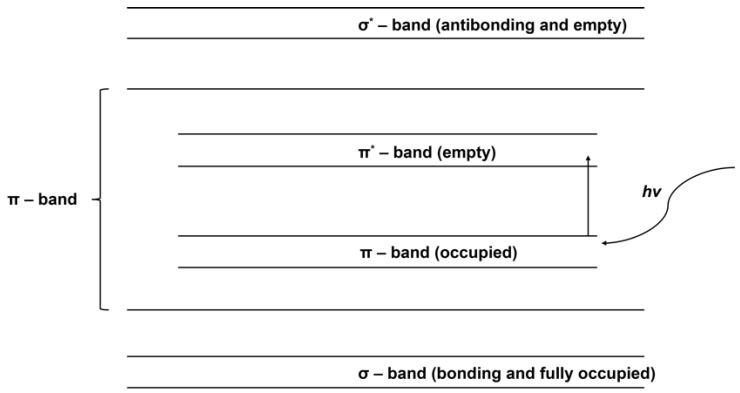

Figure 2. Schematic of the band diagram of π-conjugated molecules where the generation of a mobile electron in the π*-band and a mobile hole in the π-band due to the absorption of a photon (represented as hv) is displayed.

The initial discovery of electrical conductivity in polymers by Chemistry Nobel Prize award winners Alan Heeger, Alan MacDiarmid and Hideki Shirakawa in 2000 gave awareness to the possible idea of electronic plastic devices.[10–13] The field of polymer based organic electronic devices was driven by their parallel ties to inorganic semiconductors, most specifically, the silicon solar cells which reached critical acclaim when achieving efficiencies up to 22.8% and also in addition to the organic's light weight, mechanical flexibility and low manufacturing costs.[11,14] This field, gaining significant attention after the discovery of conjugated *trans*-polyacetylene, warranted the hypothesis of creating a "synthetic-organic metal" which would display complete electron delocalization.[8] Despite this exciting idea, Rudolf Peierls demonstrated as early as in 1955 an instability which described that a one-dimensional chain of equally spaced ions with each ion donating one electron to the electronic structure is in fact unstable. Thus, in practice there is an alternation in bond length between carbons, and the hypothesized "synthetic organic metal" is unatainable.[11]

In spite of this discovery, there were continuous efforts to construct low band gap polymer based organic semiconducting materials with the first legitimate discovery by Wudl *et al*.[15] in 1984 with poly(isothianaphthene) which demonstrated a band gap of 1.2 eV.[11,15] With the determination to construct devices out of organic materials which mimic the properties of inorganic counterparts, it is possible to envision such devices as organic photovoltaics (OPVs) or even organic light emitting diodes (OLEDs) assembled with modern conjugated organic polymers.[8] With the increase in discoveries of low band gap, conjugated polymers, the implementation of these materials within devices started.

As presented in Figure 1, high, medium and low band gap refers to the distance in energy between the valence and conduction energy levels. Where evidently, the high, medium and low band gap directly relates to the terms, insulator, semiconductor and conductor respectively. The band gap indicates how easily electrons may pass into the conduction band which is inversely proportional to the energy difference between valence and conduction bands. For instance, the organic, polymer based photovoltaic where the working principle is such that a photoinduced promotion of an electron into the conduction band creates an electron-hole pair that migrates to the electron donor and acceptor interface where it dissociates so the charges can travel to their

corresponding electrodes, leads to the creation of an electric current.[8,11,16] When studied further, this physical concept translates to more than only photovoltaics as these materials may be applied with the same device design for near-infrared photodetectors.[11,17]

Arguably one of the most prominent semiconducting polymers, poly(3-hexylthiophene) (P3HT), has been researched extensively for its applications in organic electronic devices.[6,9,10]

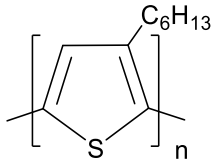

Figure 3. Chemical structure of poly(3-hexylthiophene) (P3HT).

Despite the front runner being P3HT, conjugated polythiophenes in general have had their share of investment based on their inclusion of environmentally friendly attributes.[10] As of recent, P3HT is considered the model polymer in cases considering charge transport with intended applications in a variety of organic electronic devices including OPV, OLED and organic field-effect transistors (OFET). In addition to the applications that P3HT may contribute to the scientific community and its charge-transport capabilities, P3HT is also considered to have advanced opto-electronic attributes as well as exhibiting favourable film morphology once applied to the processing of said material. Processability is a subject that will be discussed in further detail later in this memoir.[10]

In reference to the chemical structure displayed in Figure 3, the monomer that constructs P3HT—(3-hexylthiophene)—is not symmetrical. This asymmetry observed in the monomer which constructs P3HT suggests that possible regioregularities of P3HT are attainable. Literature reports have indicated in depth that the regiospecificity of P3HT has drastic effects on the opto-electronic properties exhibited by the material suggesting the importance of the control over the polymerization steps to synthesize this material or in fact, any conjugated opto-electronically active polymer resulting from an unsymmetrical monomer.[10,18] An example of the difference between regioregular and regioirregular (also known as regiorandom) P3HT is displayed in Figure 4 for the purpose of illustrating the difference between such moieties.

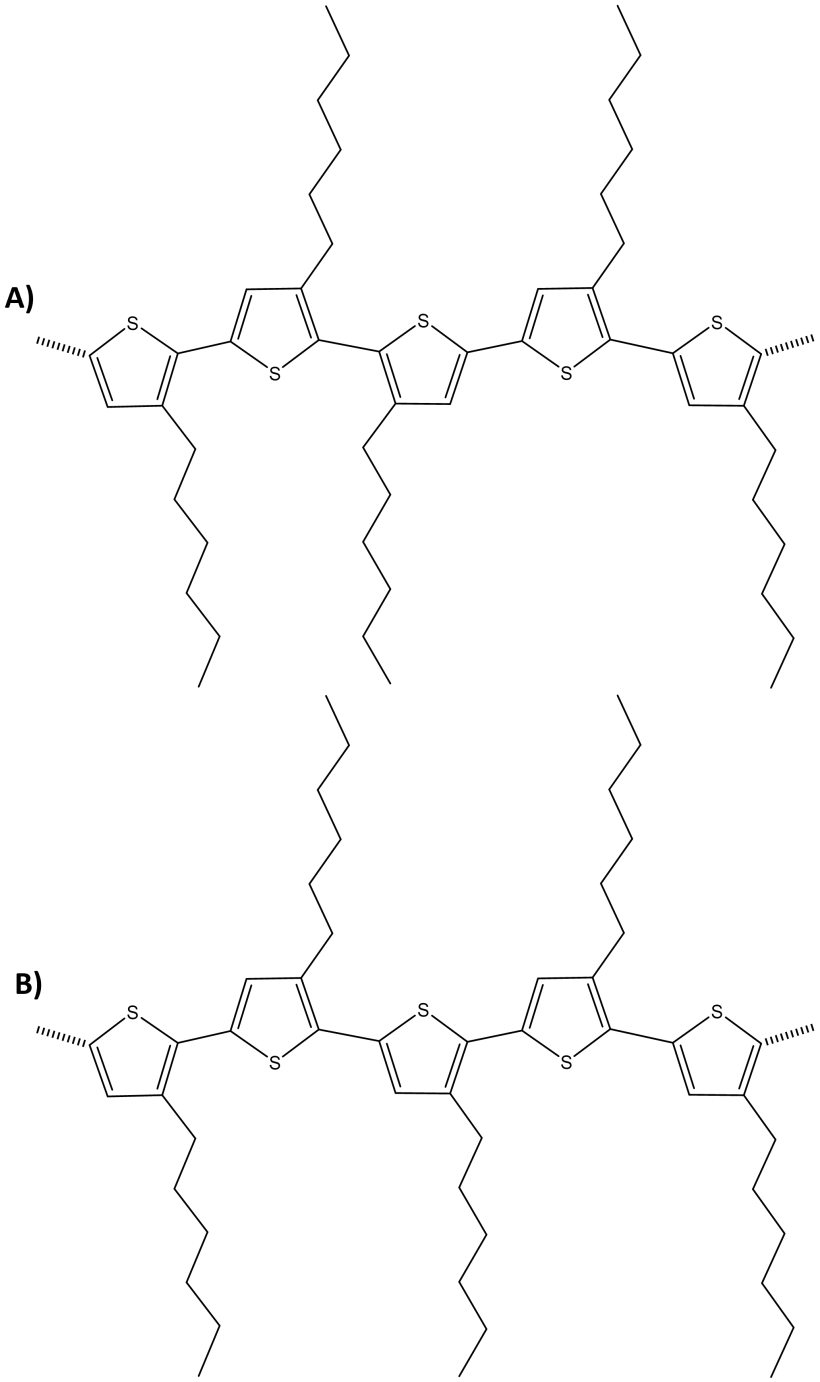

Figure 4. A) Regioirregular or regiorandom P3HT B) Regioregular P3HT.[10]

1.2 Photoconductor

Organic semi-conductors can also be used in simpler devices than those mentioned in the earlier sections. One of these devices is employed as a photoconductor device. A photoconductor is a device that converts light into a charge.[19] Fundamentally, a photoconductor is a homogenous layer of an opto-electronically active semiconducting material.[20] This device was first realized by Chester Carlson in 1942 *via* his attempts in designing and developing electrophotography which is used in devices more commonly known today as "copiers" where the process is essentially unchanged from the original Xerox 914 despite advances in modern materials applied to said process.[19] In addition to electrophotography, photoconductors have shown an additional importance when used as photodetectors.[20]

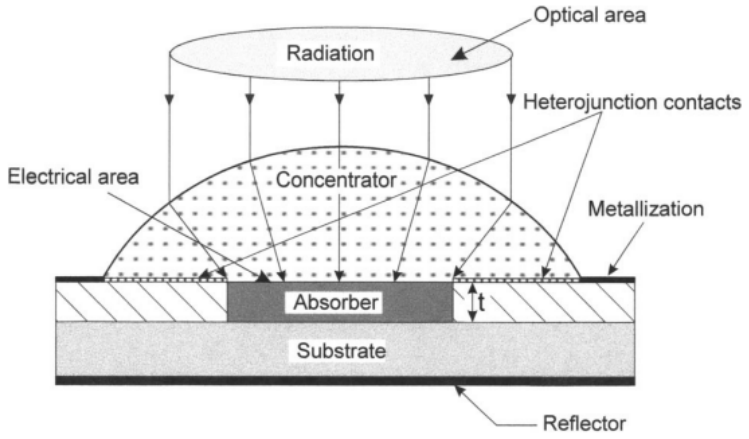

Figure 5. Schematic of a photodetector device, where the absorber corresponds to the layer of organic semi-conductor.[20]

The physical phenomenon that occurs within one of these devices is described by the absorption of incident radiation by free electrons, electrons bound to lattice atoms or electrons bound to impurity (dopant) atoms.[20] Currently, photodetectors are graded on two values known as the quantum efficiency (η) and the photoelectric gain (g), where the quantum efficiency describes the efficiency at which the radiation is absorbed by the material and is defined as the count of each electron-hole pair that is created per each proceeding photon. The photoelectric gain describes the number of charge carriers which cross the contacts per electron-hole pair generation and is defined as the ratio of the photoelectron lifetime to the transit time.[20]

$$R_i = \frac{\lambda \eta}{h\, c}\, q\, g$$

Equation 1. Spectral current responsivity where λ is the wavelength of incident electromagnetic radiation, η is the quantum efficiency, h is Planck's constant, c is the speed of light, q is the charge of the electron and g is the photoelectric gain. η and g are considered to be constant over the volume of the device.[20]

As discussed before, organic materials have fallen short to their inorganic counterparts, but organic semiconducting polymers may also be an answer to a new generation of photoconductors. Ideally, a photoconductive polymer should exhibit a few specific properties. First, it must be a good insulator when it's not in the path of incident light (in the dark) and must be capable of sustaining a strong electric field. Second, once irradiated with light, the materials must be capable of generating a high quantum efficiency. Third, the spawned charges must be able to flow through the polymer film.[21] Specifically, the imaging industry is one electronics application where organic polymers are considered superior to their inorganic counterparts (as illustrated in Figure 6) as photoconductive polymers are applied as photosensitive receptors or charge carrying materials in copy machines and laser printers.[19,21]

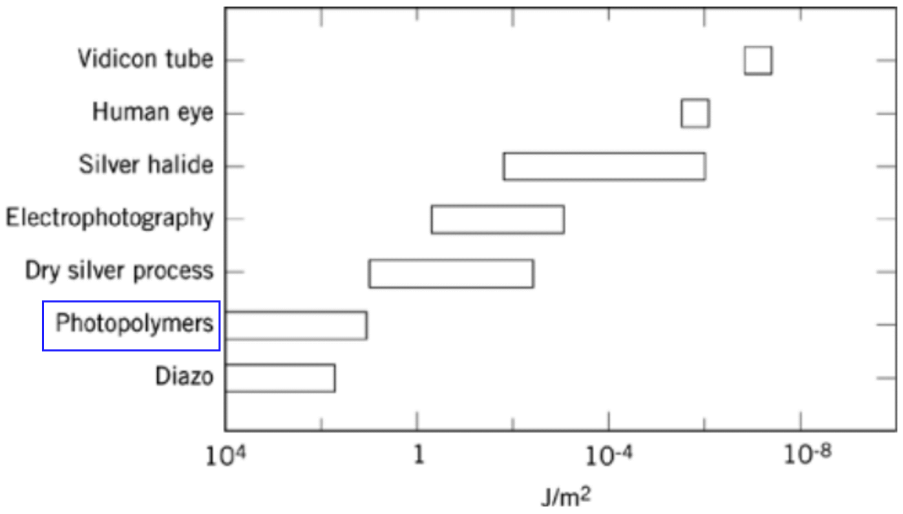

Figure 6. Sensitivities of common imaging techniques adapted from Strohriegl *et al*.[21]

Photoconductive polymers, as referenced to in Figure 6, may be categorized into five classes of materials: starting with polymers with pendant groups which do not transport charge

along the polymer backbone, but instead, charge carriers jump along the electroactive pendant groups which are covalently attached to the polymer. The second class to be discussed are molecularly doped polymers. In this case, the polymer does not directly participate in charge carrier transport but rather acts as a binder towards a photo-electronically active small molecule trapped within the polymer. Despite not being a part of the charge transport process, the polymer can influence the process *via* physical interactions between the polymer and small molecules. Next, there is liquid crystalline systems. Despite limited practical examples of liquid crystalline polymers, theoretically, ordered arrangements could provide sufficient overlap of *p*-orbitals and therefore allowing for charge transport.

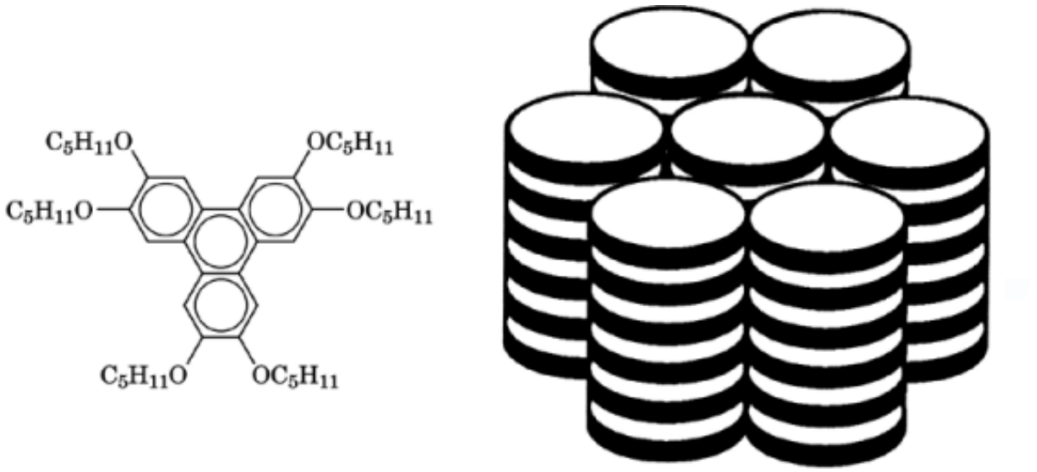

Figure 7. Molecular structure of hexapentyloxytriphenylene and a schematic of the ordered column arrangement that it will take after a mesophase transition at 69 °C.[21]

Small semiconducting materials known as nanoclusters, nanoparticles, and quantum dots—which are in the nanometer regime—may also be doped into polymers in order to develop another category of photoconductive polymers known as nanocluster/polymer composites.

Last but certainly not least and most pertinent to the herein report, are backbone conjugated polymers. The charge transport of this class is extremely dependant on the extent of π-conjugation along the backbone of the polymer.[10] This class is where P3HT falls—the principal material analyzed in this memoir, and selected due to the extensive understanding of this material in photoactive polymers.[21] Moreover, it is important to note that photoconductor-based

devices, compared to OPV and OLED, can work with a layer of semi-conductor that is considered relatively thick, which justifies our selection of studying 3D printing of P3HT for its potential use as photoconductors.

1.3 Polymer Processing

1.3.1 Conventional Techniques for Thermoplastic Processing

Currently the processing techniques applied to thermoplastic polymers—polymers that become pliable or malleable at a specific temperature known as the glass transition temperature (T_g)—can be categorized by extrusion, postdie processing, forming, and injection molding.[22] The most common technique would be extrusion based processing where, in general, a polymer is pushed through the end of a nozzle that may have many different types of geometry choices such as sheets, tubing, and fibres. Moving forward to the postdie techniques which include fibre spinning, film blowing and sheet forming. These processing techniques are considered to be "surface-free" processes where the shape of the material is determined more by the rheological (flow) properties of said material. The next processing technique discussed is known as forming. Techniques falling under this category include blow molding, thermoforming and compression molding. Essentially, the aforementioned techniques involve the process of warming a polymer to its glass transition temperature and then is manipulated into a mold by means of either mechanical force, pressure or pull *via* vacuum. The final generic category of thermoplastic polymer processing is that of injection molding. This technique involves the extrusion of a polymer out of a nozzle and directly into a mold.[22]

1.3.2 Challenges Associated with the Processing of Conjugated Polymers

The processing of polymers is unique as polymeric materials exhibit flow properties in comparison to low molecular weight fluids. These low molecular weight fluids can be characterized under the umbrella of Newtonian fluids which hold a single flow property, viscosity, as well as their density. Newtonian fluids are defined as follows: at constant temperature and pressure, the shear stress is proportional to the rate of shear and thus the constant of proportionality is the dynamic viscosity.[23] Polymeric materials are significantly more complicated

to understand as their viscosity function depends on the shear rate, time dependant rheological properties, and viscoelastic behaviour.[22] In addition, when conjugation is introduced into the attributes of the polymer, the processing capabilities are once again altered.[24] Conjugation within a polymer creates a brittleness within the material due to the lack of mobility and in turn impact the capability to be processed in solution as well as the mechanical attributes of the final device. The brittleness introduced by conjugation does not allow for the fluidity that is ideal for solution processing. The quality of the final processed device relies on the finalized organization of the conjugated polymer. Therefore, ideal processing of conjugated polymers is a challenge of molecular organization that must be investigated.

Due to this phenomenon, the physical properties of a polymeric material may have a significant variance between polymers and processing parameters suggesting a wider variety of applications. The next section is a review of the most prominent current and conventional methods of polymer processing that are used in industry today which also have the potential of targeting that of 2-dimensional electronic applications despite whether falling into the initial four processing techniques already aforementioned in this text.

1.4 Thin Film Processing

1.4.1 Spin-coating

Spin-coating, which is one of the most widely known processing methods for materials processing in thin films. This method has been widely employed for large scale production and reproduction of thin films. The technique is described by a solution that is dropped onto a rotating disc which then results in the ejection of material in each radial direction and the simultaneous evaporation of solvent which results in the final product being a thin film over the substrate.[25,26] Spin-coating has been a method for producing well-defined polymer films with appropriate morphology for approximately a century at the point of this memoir. Processing of various conjugated polymers *via* spin-coating technique has been achieved before in work completed by Jenekhe *et al*.[27] in 2005 which includes the processing of P3HT.

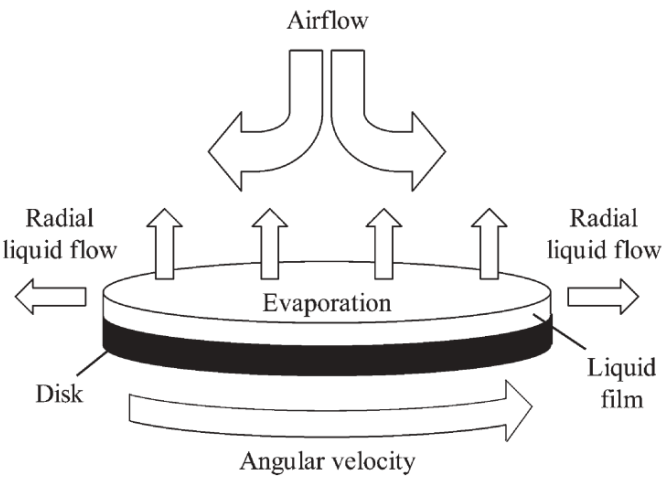

Figure 8. Schematic describing the spin-coating process.[25]

1.4.2 Dip-coating

The second processing method which is brought to the discussion of widely expressed processes is that of the dip-coating. Described as a facile and economical technique employed in industry by Yan *et al*.[28], the dip-coating approach involves the desired substrate to be immersed into solution of the desired coating and then removed from the bath of said desired solution. As elementary as this processing technique seems, there are many more physical parameters that will affect the final material than meets the eye. Such as, immersion time, withdrawal speed, repetition of dip-coating cycles, density, viscosity, and surface tension which all can reconstruct this seemingly rudimentary processes into something which can be manipulated into a highly diverse processing technique.[28] Despite the difficulty in polymer processing, high alignment of conjugated polymers has been achieved when using the dip-coating method. Recently in 2020, Pei *et al*.[29] attained high alignment in the isoindigo-based conjugated polymer (PII-2T) by exploitation of a unique dip coating method where the concentration during processing is varied to control aggregation and thus the resulting charge transport properties of the film.

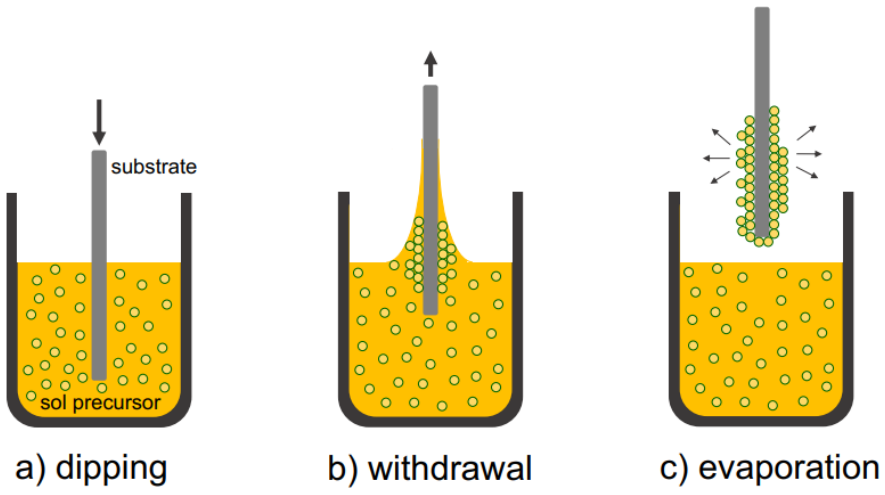

Figure 9. Schematic describing the dip-coating process.[30]

1.4.3 Blade-coating

Another commonly employed 2D processing technique is blade-coating, also known as doctor blading or doctor-blade coating. This technique is a simple process that allows for the formation of well-defined films which are prepared *via* placing a sharp blade at a specific distance from the flat substrate holding the material to be processed. The blade is then pushed linearly over the substrate, leaving a thin film of the desired sample on the substrate.[26] In a review of processing techniques for the fabrication of polymer solar cells published by Krebs *et al*.[26], the doctor blading technique was described as "parsimonious". Therefore, the doctor blading technique is a facile and cost-effective way to compare thin films created by new and more advanced techniques to the simple blade coated films. The aforementioned content should be noted by the reader, as the comparison of films formed *via* advanced techniques with films created by blade-coating will be an essential topic later in this memoir in Chapter 5, especially as the processing of P3HT *via* blade-coating is quite well understood and commonly employed. For example, Dorling *et al*.[31] implemented blade-coating to process their P3HT with the crystallizable solvent 1,3,5-trichlorobenzene to realize an OPV device where they found that blade-coating induced additional alignment in P3HT.

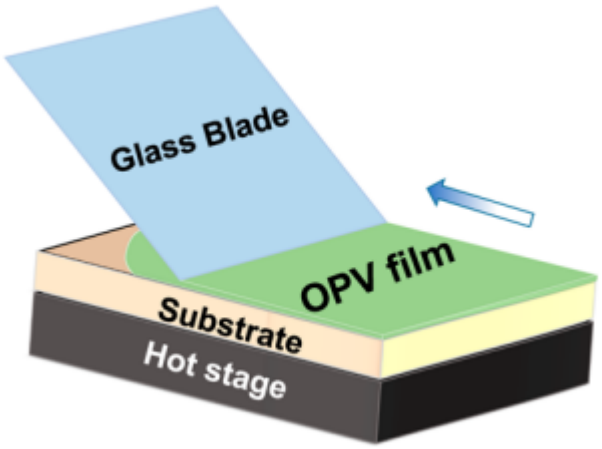

Figure 10. Illustration describing the blade coating processing technique used by Ade *et al*.[32] for the processing of polymer based photovoltaics.

1.4.4 Slot-die Coating

The final processing method that will be discussed in detail during the review of 2D processing techniques is known as slot-die coating, which is considered a widely used, versatile process for the production of thin, uniform films. The standard process involves the flow of a liquid through a fixed slot gap which is then delivered onto a moving substrate. Subsequently, the evaporation of the solvent results in the formation of a thin film.[26,33] Slot-die coating holds a significant advantage over the previously discussed—arguably elementary—processing techniques in that the slot-die coating process is a pre-metered process. Therefore, the thickness of the coated liquid layer (wet thickness) can be set beforehand and precisely controlled *via* the flow rate and coating speed. In addition, this suggests that in comparison to other processing methods, slot-die coating is highly efficient in materials usage resulting in lower levels of material waste.[26,33,34] Slot-die coating is of significant importance for polymer processing and more specifically conjugated polymer processing with reasons due to practicality in real world settings such as for OPV where the final device requires high throughput printing techniques in order to produce cells with high enough surface area to produce useful amounts of energy. This places slot-die coating in a very interesting area of polymer processing as it allows for the production of large area thin films since it is considered to be compatible with roll-to-roll coating techniques. In recent years—due to the interest in slot-die coating—work has been completed on a variety of

polymeric devices produced from this technique. For example, Reynolds *et al*.[35] managed to produce an OPV device from the blue-green coloured, low band gap polymer, PGREEN and (6,6)-phenyl-C_{61}-butyric acid methyl ester (PCBM) which was one of the first to be produced by slot-die coating without the use of an absorbing layer created from P3HT:PCBM showing the versatility of their technique.

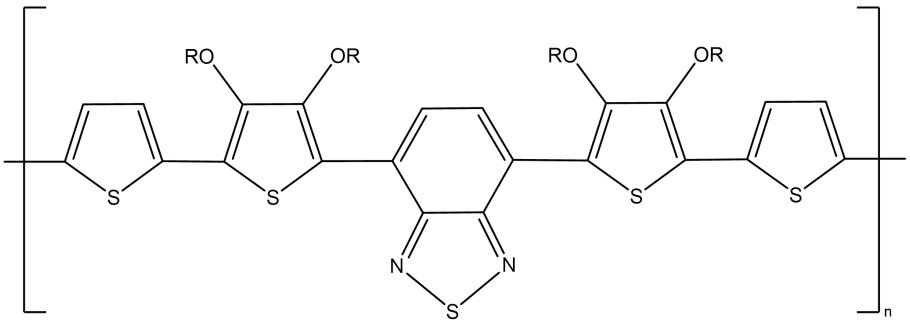

Figure 11. PGREEN structure where R is 2-ethylhexyl.[35]

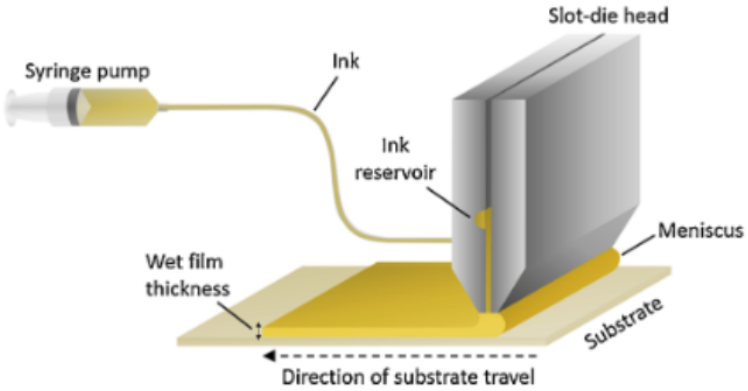

Figure 12. Schematic describing the slot-die coating process.[34]

In industry to date, a wide variety of reliable polymer processing techniques have been employed to produce 2D polymer thin films for various devices and applications. Throughout the past section, an emphasis has been put on the processing of "2D polymers". As materials scientists existing in three spatial dimensions and imagining futuristic devices, seeking out 3D devices and in turn, utilizing 3D processing techniques is necessary. Chemically, we must then assess the

impact of the addition of a z-component (out-of-plane) on the molecular organization of the organic conjugated compound.

1.5 Polymer Processing in 3D

Setting sights on futuristic organic electronic devices, the consideration of an additional dimension to form 3D devices is imminent and essential. Introduced in the 1980s and arguably the most recognized method of producing customized 3D objects made from metals, ceramics as well as polymers is known in the scientific community as additive manufacturing (AM) with alias known to be public as 3D printing. Additive manufacturing is the process of taking a virtual 3D model from a computer aided design (CAD) and digitally slicing it so that the instrument, *via* a Geometric code (G-code) can build the physical object layer by layer without the need for a mold or any etching process.[36] There are a variety of AM categories that each bring unique processes to the discussion which will be detailed in more length during this section.[37]

1.5.1 Vat Photopolymerization

The review of additive manufacturing techniques begins with vat polymerization which branches out to more specific techniques known as stereolithography and digital light processing. These techniques are very similar to each other as they both utilize photopolymerization to selectively cross-link photopolymerizable resins layer by layer—which all AM techniques utilize—to control the building of a free standing 3D object.[36] A major advantage to this technique is the high spatial resolution acquired due to the focusing power of the beam used for the photochemical polymerization.[36] Evidently, this processing technique is limited as it can only be applied to resins which are photochemically active in order to create free standing 3D objects. In terms of vat photopolymerization, there are few publications to date that report the processing of conjugated polymers due to the potentially complex redox chemistries as well as usually the conjugated polymers absorb heavily in the same region where the photoinitiator absorbs.[38] Despite this, some groups have been able to overcome the challenges of processing conjugated polymers *via* vat photopolymerization. For example, Soman *et al*.[39] managed to process poly(ethylene glycol) diacrylate-polyaniline (PEGda-PANI) conductive hydrogel by photopolymerization.

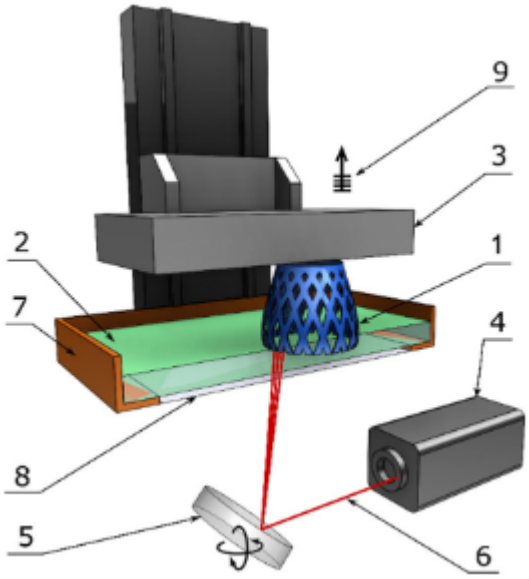

Figure 13. Description of a stereolithography instrument where numbers 1-9 are respectively the printed part, liquid resin, building platform, UV laser source, XY scanning mirror, laser beam, resin tank, window, and layer by layer elevation.[40]

1.5.2 Powder Bed Fusion

Powder bed fusion is a selective process that consists of powder deposition, powder solidification then the lowering of the bed platform by one layer to then repeat the process. The solidification process is performed by laser radiation where the source is absorbed causing softening, melting and finally solidification of the particles who interact with the laser.[36] Powder bed fusion can also be separated into sub-categories including direct metal laser deposition, selective laser sintering, selective laser melting, electron beam melting and selective heat sintering.[37] The variations in the powder bed fusion process allow for the production of complex materials. Despite this advanced technique displaying high quality production of 3D objects, there are drawbacks involving the economics to utilize such instruments as parts can be expensive and some of these techniques require high vacuum operation.[37] In terms of polymer processing, Nolte *et al*.[41] developed a technique using ultrashort laser pulses at 1030 nm to process ultra-high

molecular weight polyethylene which surpassed the properties of this material processed with the conventional CO_2 laser.

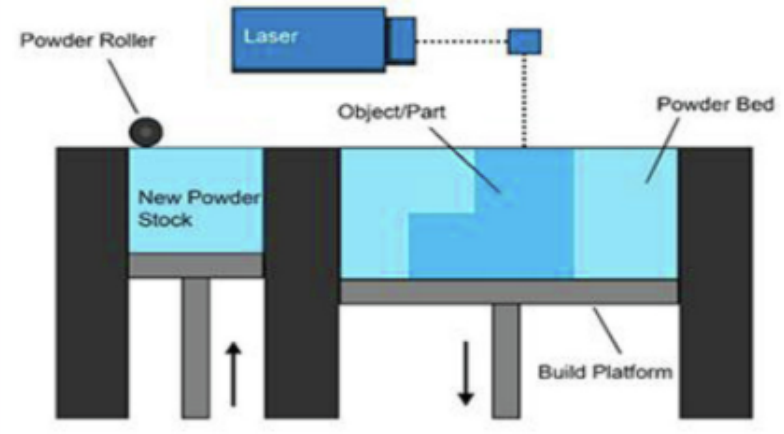

Figure 14. Schematic of the selective laser melting/sintering processing technique.[37]

1.5.2 Material and Binder Jetting

The next classification of additive manufacturing is known as material and binder jetting which can be separated into classes of inkjet printing, aerosol jet printing and powder binding processes. For the case of the commonly applied inkjet printing process, a thermal "drop on demand" technique is used which involves thermally inducing a liquid ink to form a bubble within the reservoir resulting in the propulsion of a droplet out of the printing head. There are cases where instead of thermal induction driving the printing process, a piezoelectric actuator is employed instead.[36] Additionally, some of the leading producers in AM device producers—Stratasys and 3D Systems—have been successful in producing AM techniques that combine the advantages of high build speed with large build volume that material jetting exhibits and high spatial feature resolution that lithography exhibits creating inkjet lithography 3D printers.[36,42] Literature does have some reports of jetting conjugated polymers: Holdcroft *et al*.[43] managed to process poly(3-(2-(2-tetrahydropyranyloxy)ethylthiophene) (PTHPET) containing a near-infrared sensitive dye.

1.5.3 Extrusion

The succeeding processing method is known as material extrusion based additive manufacturing and will be the technique that is most relevant in the presented memoir. Material extrusion AM is the deposition of melts or solutions through a moving extrusion head or moving printing bed surface where the *x*, *y* and *z* movements are computer controlled.[36] Like the other 3D processing methods discussed in this section, material extrusion AM can be separated into many techniques such as fused filament fabrication, fluid dosing and deposition, direct-ink writing and more.[36,44]

The specific technique of interest herein is direct-ink writing (DIW). DIW is a unique and versatile technique as it allows for the processing of any material that is engineered to have the suitable rheological behaviours known as shear-thinning and thixotropy which will be discussed in further detail in the next section.[44] The exact process is that a viscoelastic ink is extruded through a computer driven nozzle where the ink is pushed out *via* changes in air pressure or mechanical pressure. After the deposition of a single layer, the nozzle can vary in the *z* direction to add subsequent layers, defining this process as a layer-by-layer technique.[44] The unique aspect of DIW is that one governs the ability to customize the printing inks to print a wide variety of 3D structures with a variety of characteristics and properties. In addition to the rheological properties that have an influence on the printability of an ink, there are a variety of machine parameters that also play a major role such as nozzle size and printing speed. The combination of these factors have a grand determination on the accuracy and resolution of the final 3D printed object.[44] in addition, it has been noted in literature that the shear forces experienced during the DIW process may induce molecular alignment which is of significant interest especially in the context of organic optoelectronic devices in promoting charge transport.[45]

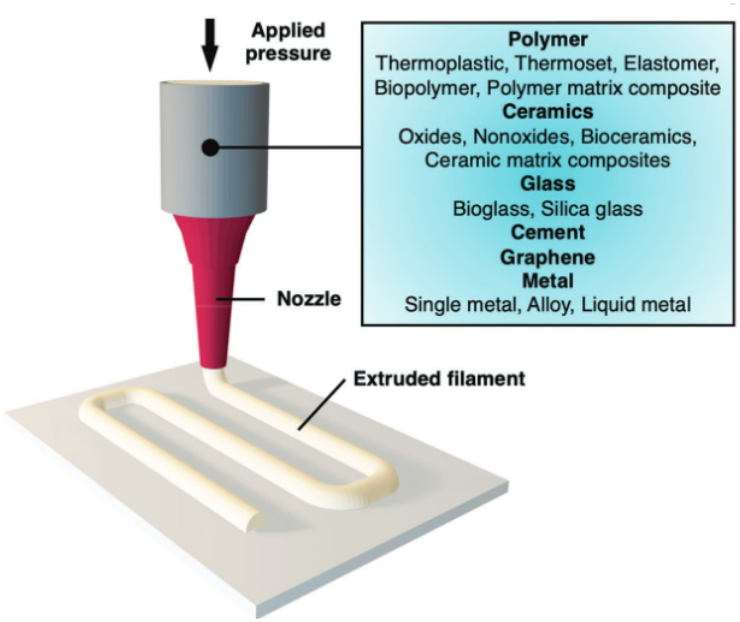

Figure 15. Direct-ink writing schematic with additional 3D ink information[44]

As discussed previously, many electronic devices benefit from utilization in 3D architectures including—but not limited to—bio-interfaces, OPVs, and energy storage apparatus suggesting that the 3D printing of electronically active materials is paramount. To give context, there is a significant mechanical mismatch between inorganic electronic devices and biological tissue for electronics at the bio-interface. This is just one example of how conjugated polymers printed in 3D can potentially out-perform their inorganic counterparts. In general, extrusion based 3D printing—including direct-ink writing—is an exceptional option for 3D printing conjugated polymers which is a technique that allows for the engineering of inks in a wide variety of ways to allow for not only creating suitable inks for printing at ambient conditions but also suitable materials for device fabrication while avoiding the degradation of organic conjugated compounds.[46]

In practicality, various works are being completed to engineer inks to be appropriate candidates for direct-ink writing as well as possessing device functionality. Mecerreyes *et al*.[47] designed a graft copolymer made up from the conducting polymer poly(3,4-ethylenedioxythiophene) (PEDOT) and a biocompatible polymer known as polylactide (PLA) with the means of manufacturing bioelectronics. In another case, Zhu *et al*.[48] was capable of exploiting

direct-ink writing for controlled microscale deposition of the conjugated polymer poly[2,5-(2-octyldodecyl)-3,6-diketopyrrolopyrrole-alt-5,5-(2,5-di(thien-2-yl)thieno[3,2-b]thiophene)] micro-ribbons down to a scale of 5 µm for applications in organic transistors displaying the high resolution DIW printing may produce. For depth into the inspiration of this project, direct-ink writing of conjugated polymers has successfully been completed in various literature. For example, Price *et al*.[49] managed to print conductive polyaniline structures.

1.6 Assessing Printability *via* Rheology

To engineer inks that will have ideal outcomes when printed *via* direct-ink writing, one must understand rheological properties of the material before the printing process as well as to be able to measure the print fidelity of a material once it has been printed. Rheology is defined as the deformation and flow of a material during the influence of applied forces.[50] During the extrusion process—such as in direct-ink writing—the ink experiences a shear force whilst moving through the nozzle so that it must change in molecular organization then finally relaxing after leaving the nozzle.[50] Rheological properties that are of concern in this process include viscosity, shear-thinning and thixotropy. Understanding a material's rheological properties before the printing process is a goal in the extrusion-based AM world as it may allow for the prediction of the quality of an ink. There is then a procedure that can be used to quantify the print fidelity of an ink which will also be discussed.

First, one must understand the definition of viscosity which is as follows: the resistance of the flow of a fluid when experiencing an applied force. In the case of polymers, the main attributes in consideration of viscosity are the concentration as well as the molecular weight.[50] It is a general assumption that an ink with higher viscosity would yield a better final print, or better printability—as the solidification of the ink after extrusion would be more satisfactory—but this is contradictory as higher viscous inks tend to have higher shear stress. Viscosity can be described as the ratio between the shear stress and shear rate, bringing us to our second property to define.[50]

$$\mu = \frac{\sigma}{\dot{\gamma}}$$

Equation 2. Viscosity in terms of shear rate and stress where viscosity is μ, shear stress is σ and shear rate is $\dot{\gamma}$.

Fluids that display a linear relationship between shear stress and shear rate are described as *Newtonian* fluids while fluids displaying divergence from linearity are termed *non-Newtonian*. *Non-Newtonian* fluids can display unique properties that may be time-independent as well as time-dependent. Time-independent properties include shear-thinning or shear-thickening behaviour which is, respectively, the decrease or increase in viscosity when a shear force is applied. Polymers often display shear-thinning behaviour which corresponds to the shear-induced disentanglement and following, alignment, of polymer chains resulting in the ease of flow during extrusion. *Non-Newtonian* time-dependent flow properties include thixotropy where viscosity decreases with time at some constant shear rate and following, will return to its original viscosity after rest while a rheopectic material will display the opposite flow behaviour.[50] In terms of extrusion based AM, thixotropic flow behaviour is favourable as allowing for a viscous, shear-thinning material to return to its original viscosity in order to solidify will result in a more favourable print-product.[46]

There are a variety of challenges to process π-conjugated compounds, including conjugated polymers. Therefore, the most modern and ideal way of processing such compounds would be to blend the conjugated polymer (in this case P3HT) into thermoplastic polymers thus to make the material processible. The inks created after blending P3HT with thermoplastic matrices would fall under the category of *non-Newtonian* fluids.

1.7 Assessing Print Fidelity

To have high print fidelity in order to obtain high quality prints for the intended application, printability has been quantified and displayed by Chen *et al*.[51] where one may use a *uniformity factor (U)* to compare the width of printed strands to their ideal theoretically uniform strands as input in the CAD file. *Via* microscope technologies, one can image and measure a printed filament to compare to the ideal dimensions of the previously discussed computer aided

design. For an ideal uniform filament, one can calculate the uniformity factor which ideally would equal 1 and is mathematically and visually represented in the equation and Figure 16 below.

$$U = \frac{width\ of\ printed\ strand}{width\ of\ theoretical\ straight\ strand}$$

Equation 3. Equation for the calculation of the *uniformity factor*.[51]

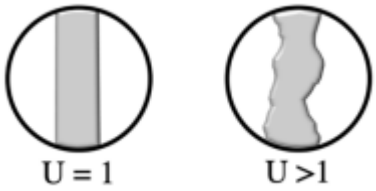

Figure 16. Schematic displaying uniformity in printed strands.[51]

1.8 Probing Molecular Organization at Different Scales

Exploring the molecular organization of conjugated polymers with optical spectroscopy and microscopy, as well as their semicrystalline behaviour with X-ray diffraction and thermal characterization techniques, one may gather information on how these macromolecules behave before, during and after processing. At first glance, there is an unmistakable anisotropic charge transfer behaviour when considering conjugated polymer systems—including P3HT—which makes the ability to control and/or probe the alignment of these systems significantly more relevant to engineering an optoelectronic device.[52] For example, and again, in the case of P3HT, there is a significantly larger charge mobility along the polymer chain direction or through interchain transport *via* π-π stacking compared to the direction along the alkyl side chains which is visually represented below.[52,53]

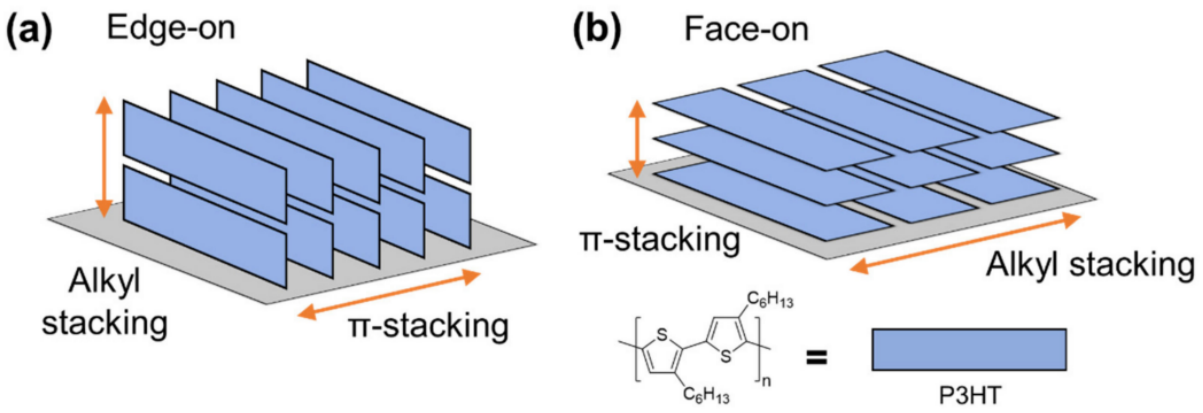

Figure 17. Stacking illustration of P3HT aggregates. **(a)** edge-on stacking and **(b)** face-on stacking.[53]

1.8.1 UV-visible Spectroscopy

Due to the electronic properties differing depending on the orientation of the P3HT chains within the aggregates, which is represented in Figure 17, UV-vis spectroscopy may be exploited as a powerful tool to probe the type of aggregates found in the soli-state of P3HT.[54] Deconvolution of a UV-vis spectrum of P3HT aggregates in solution or solid state with a Franck-Condon fit—i.e. comparing the $A_{0\text{-}0}$ and $A_{0\text{-}1}$ transitions—can reveal the percent of P3HT involved in aggregation, the nature of the aggregates, as well as the conjugation length.[54]

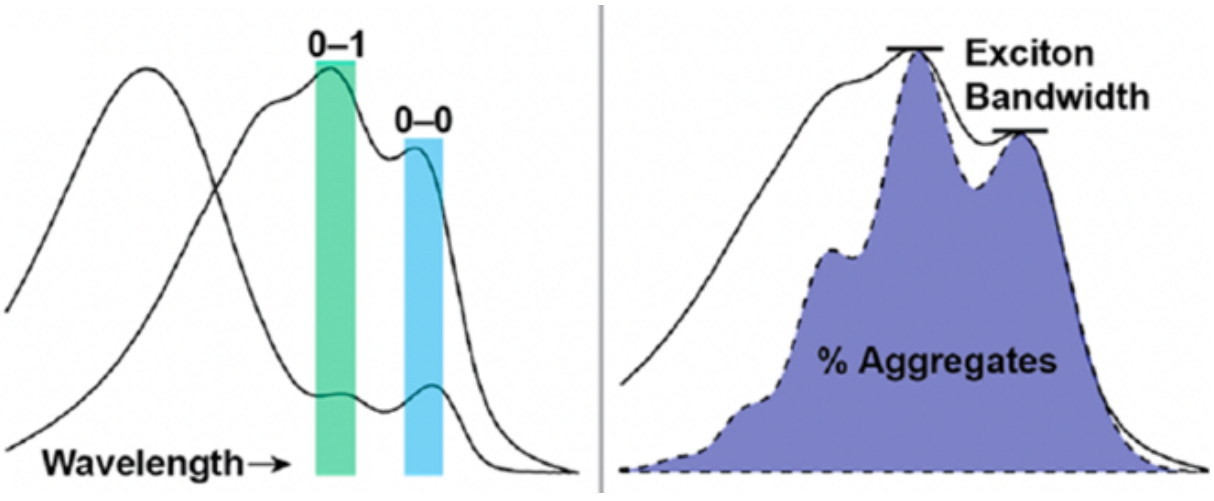

Figure 18. Depiction of a UV-visible spectrum analyzed *via* a Franck-Condon fit to extrapolate aggregate percentage as well as exciton bandwidth.[54] Here, one may compare the intensities of the absorption of $A_{0\text{-}0}$ and $A_{0\text{-}1}$ peaks which correlate to the exciton bandwidth.

Displayed in Figure 18, the ratio of the $A_{0\text{-}0}$ transition to the $A_{0\text{-}1}$ transition can be used to give a better depiction of the molecular environment. For example, a stronger $A_{0\text{-}0}$ transition compared to a $A_{0\text{-}1}$ transition is associated with a lower exciton bandwidth and therefore a higher conjugation length, an increase in the planar behaviour of the polymer backbone and an increase in the J-aggregate behaviour in relation to the H-aggregate.[54] Therefore, UV-vis spectroscopy is a necessary tool, giving a depth of insight into the supramolecular chemistry of the molecular environment of P3HT aggregates which are present when processing P3HT for optoelectronic devices. Moreover, UV-visible spectroscopy can be used to calculate a dichroic ratio. Dichroism defined by Maleki *et al*.[55] as "the difference in absorbance between two linearly polarized beams of light possessing electric vectors in two orthogonal directions".[55]

$$R = \frac{A_{||}}{A_{\perp}}$$

Equation 4. Dichroic ratio, where $A_{||}$ and $A_{\perp}$ represent the absorption of light polarized parallel and perpendicular to the experimental axis.[55]

This property displayed by conjugated polymers is noteworthy as it can give information about the directional aggregation of P3HT within the matrix which is of significance to the application of electronic devices. The capability of observing the directional aggregation of P3HT is of significance to the application of electronic devices as the direction of electron transfer will drastically affect the efficiency of the device.

1.8.2 Fluorescence Spectroscopy

Generically, it would be expected that the fluorescence spectrum of P3HT—or any substance for that matter—would be the mirror image of the absorbance spectrum. But one must consider quantum mechanical factors such as the Franck-Condon principle which states that transitions between electronic states correspond to vertical diagrammatic lines on a graph that positions energy on the *y* axis and internuclear distance on the *x* axis. This is based on the fundamental principle that an electron can transition between states significantly faster than a molecule can vibrate and rotate.[56] Therefore the internuclear distance does not change during the electronic transition but can change whilst the vibrational states relax from some higher state

within the excited state to the lowest state in the excited state. After careful examination of Figure 19, a difference in dipole moment between relaxed and excited states indicating that there is a configuration difference in a molecule after excitation. This is of significant interest in this study as when studying the fluorescence spectrum of P3HT within a thermoplastic matrix, one can obtain information on how the P3HT aggregates behave and interact with its surroundings when processed in a variety of different matrices.

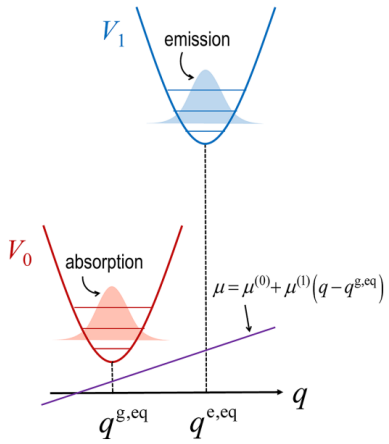

Figure 19. Scheme displaying the Frank-Condon principle where the ground and excited potential energy surfaces are displayed along an internuclear distance axis and including the linearized dipole moment function.[57]

1.8.3 Optical Microscopy

Optical microscopy, including fluorescence and polarized microscopy, can be utilized to visually observe the aggregation of P3HT within the thermoplastic matrices. The optical requirements for fluorescence microscopy analysis include the delivery of light radiation at an appropriate wavelength for the sample specimen, the capability of separating the excitation light from the sampled emission and collecting as much of the fluorescence as possible, then the allowance for fine detail observation.[58] As P3HT is the fluorescent specimen within the printed samples, fluorescence microscopy can show how P3HT is spread and aggregated throughout the matrices. The fluorescence microscope used in our experiments is capable of standard transmission microscopy, fluorescence microscopy, and additionally, polarized microscopy.

Conjugated polymers such as P3HT interact with polarized light such that the modulation of the polarized light may reveal the polarization direction as well as segmental alignment.[59]

1.8.4 X-Ray Diffraction

As P3HT is a semicrystalline polymer, X-ray diffraction techniques may be useful in addition to UV-vis spectroscopy to understand the aggregation of P3HT within a system, but also to determine if it impacts the nature of the phase of the thermoplastic matrix. Also, in terms of a photoelectric device, the nature of the local packing is necessary to understand as it also defines the charge transport behaviour of the material.[53,60] Ideally for these systems, one would explore the crystallinity *via* grazing incidence wide angle X-ray scattering (GIWAXS) and/or grazing incidence small angle X-ray scattering (GISAXS). The combination of these techniques can give information including domain size, domain shape, phase separation and purity in the case of GISAXS and for GIWAXS, crystallinity, crystal orientation and size.[61]

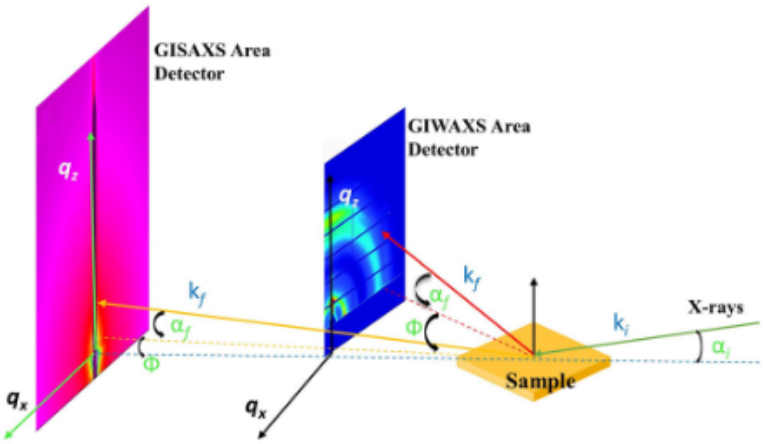

Figure 20. Schematic describing the difference in geometry of GIWAXS and GISAXS.[61]

It is pertinent that crystallinity is monitored as crystallites formed in semicrystalline polymer films can adopt different orientations known as “edge-on” or “face-on” which are visually displayed in Figure 21. The orientation of the crystals will adopt a majority face-on orientation if the preferential π-π stacking is in the *z* direction and therefore will adopt a majority edge-on orientation if the π-π stacking is in the *x-y* plane.[61] The reasoning for this significance is that the orientation of the crystallites will affect the charge mobility as aforementioned in section

1.8.1. Lastly, it is important to mention that the phase behavior observed in X-ray diffraction will be confirmed *via* differential scanning calorimetry measurements, as described in detail in Chapter 3.

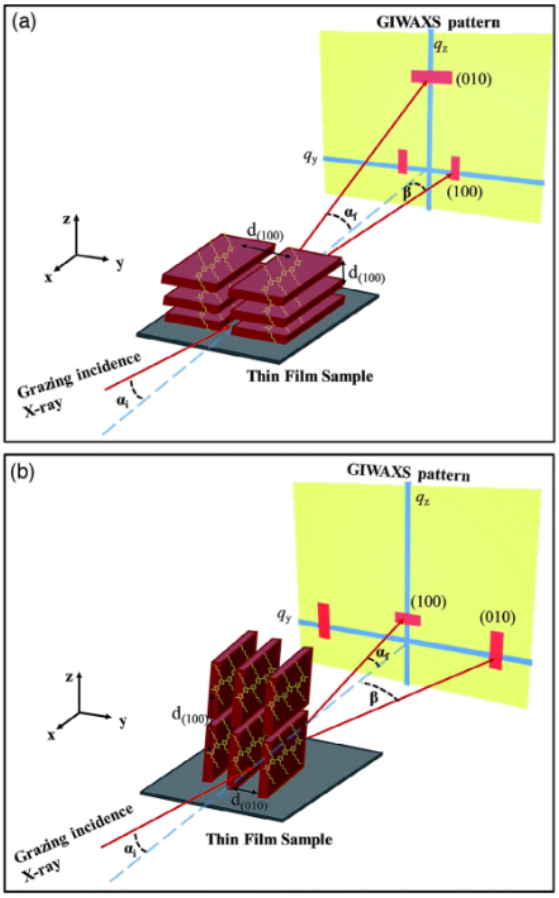

Figure 21. Schematic of how grazing incidence X-rays identify orientation in semicrystalline polymers.[61]

1.9 Objective

1.9.1 Overview

For context, the presented project explores the processing of conjugated polymers (P3HT) *via* direct-ink writing for optoelectronic devices. Due to the need for a matrix to make conjugated polymers processible, the ink to be processed will act as a *non-Newtonian* fluid and therefore the understanding of rheological properties is pertinent. In order to design 3D electronics, the

printability and print fidelity will be assessed to form materials in as high resolution as possible. Then, because of the physical environment the ink experiences whilst enduring the direct-ink writing process, the molecular aggregation and percolation of P3HT within the matrix must be assessed by microscopic, UV-vis, fluorescence and X-Ray diffraction techniques.

1.9.2 Model System

Herein, the systems selected for analysis involve the thermoplastic matrices of atactic PS, atactic PMMA, PPC, and PEO where varying concentrations (0.5% and 1.0%) of low and high regioregular P3HT are imbedded into each matrix and these materials are printed using direct-ink writing in a solvent of $CHCl_3$. The first three thermoplastics were chosen in view of determining how P3HT behaves in matrices that display various polarities and rheological behaviour. In addition, PEO was included to compare the behaviour between amorphous and semi-crystalline polymer matrices. The justification for the use of P3HT is due to the abundance of literature which studies its conductive nature *via* 2D processing methods but rarely in 3D. Initially, the pure thermoplastics matrices are studied for their printability and rheological attributes to discover the optimal printing setting as it is presumed that such low concentrations of P3HT would not affect the shear-thinning and thixotropic nature of the thermoplastics. Subsequently, each thermoplastic:P3HT combination was printed and the aggregation nature of the P3HT was analysed to determine the optimal printing environment for a photoconductive device.

1.9.3 Goals

The first goal of this project is to establish the proof-of-concept attempt at using direct-ink writing additive manufacturing to successfully print a photoconductor. By using the optoelectronically active polymer, P3HT, and mixing it into a thermoplastic matrix, one is able to create processible photoactive inks. The thermoplastic matrices make the ink more easily solution processible as well as allow for the conformability in the final device. As briefly mentioned above, the thermoplastic matrices used in this memoir are the amorphous atactic polystyrene (PS), poly(propylene carbonate) (PPC), atactic poly(methyl methacrylate) PMMA and the semicrystalline poly(ethylene oxide) PEO. As already mentioned, P3HT is the photoactive material

of concern but regioregular (rr-P3HT) as well as regiorandom (rra-P3HT) P3HT are applied to the printing process for comparison.

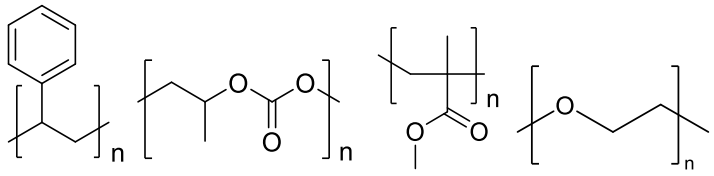

Figure 22. From left to right, molecular structures of polystyrene (PS), poly(propylene carbonate) (PPC), poly(methyl methacrylate) PMMA and poly(ethylene oxide) PEO.

Referring back to the discussion of DIW AM, the exploitation of the shear forces experienced during the extrusion process may induce alignment within the P3HT aggregates. Therefore, it is predicted that by utilizing extrusion-based 3D printing techniques, one may induce alignment within the P3HT aggregates and therefore have an increase in the charge mobility of the final device. The supramolecular chemistry of the system is evidently of major concern which is also why such a wide variety of matrices is chosen to study as well as including both rr-P3HT as well as rra-P3HT with means of optimizing the device. In order to gain an understanding of the molecular environment of P3HT embedded within the matrices, UV-vis and fluorescence spectroscopy, thermal characterization, optical microscopy as well as X-ray diffraction are employed to probe the supramolecular chemical environment generated upon the 3D printing of the P3HT:thermoplastic architectures.

This study is pertinent to the advancement of 3D printing technologies which may in fact be the future of materials processing. In addition, this study could reveal unknown aspects of the control over supramolecular organization for organic conjugated polymers – both of which are essential areas of study for the progress of engineering and physical chemistry.

Chapter 2 – Organic Photovoltaics for Indoor Light to Electricity Conversion[1]

2.1 Overview

Herein is a review of possible applications which may be relevant to the printed architectures discussed in Chapters 4 and 5. The processing of photoactive materials to form photoconductive devices is inherently important to the future of electronic devices and specifically organic photovoltaics (OPV) for solar energy conversion. Photovoltaic devices—whose physical chemistry will be established later in this Chapter—are essential to combat the current energy crisis. In addition, implementing organic materials—especially polymeric materials—can be advantageous to the economics, processibility, biocompatibility, and mechanical properties of the final processed device. Making a change from inorganics to these organic optoelectronic materials could potentially lead to a new age of flexible and biocompatible electronics.

To date, optoelectronic polymers have been processed by a variety of 2D techniques for applications in electronics including organic photovoltaics and organic field-effect transistors.[67] Although as of recently, additive manufacturing (3D printing) has gained widespread interest due to the possibility of processing materials in three dimensions. Due to the advantages of the processibility of polymers compared to their inorganic counterparts, they have become ideal candidate for 3D printing. Later in this chapter the modern processing of optoelectronic polymers will be discussed heavily but the reader is encouraged to conceptualize how processing the same materials in 3 dimensions could advance the quality of the current organic electronics we use today.

[1] Sections 2.2 to 2,6 were included in the following article, written by Myles Creran, Bryon Larson, Gregory C. Welch and Audrey Laventure : Pecunia, V. *et al*. Roadmap on Energy Harvesting Materials, Journal of Physics : Materials, 2023, 6, 042501.

2.2 Status

Organic photovoltaics (OPV) are a widely investigated clean energy (light to electricity) conversion technology in academia.[68–70] Recently, the technology has been commercialized with various products available to the general public. Key advantages compared to traditional silicon-based photovoltaics include solution processability of the photoactive layer and charge transport interlayers components, which enable ultra-low-cost manufacturing *via* coating and printing techniques, a high degree of OPV module flexibility/conformability and form factors (i.e. shapes and sizes), and tunable light harvesting properties. Limitations include the power conversion efficiency (PCE) and operational lifetimes, both inhibiting wide-spread utilization.

Owing to the high molar absorptivity of organic molecules in the visible region of the electromagnetic spectrum (i.e. white light) and the exciton-based processes involved in organic photovoltaics, they have been predicted to be capable of converting indoor light into useable electricity.[71–73] Indeed, the global indoor light harvesting market is expected to grow from $140M in 2017 to >$1B (USD) by 2023, with a projected demand for such devices by then exceeding 60 million per year. While the output power is by default low (micro watts per cm^2) such devices are suitable for low power, wireless electronic sensors for the Internet of Things (IoT). Potential application has been recently demonstrated with an OPV device reaching 25% efficiency under 1000 lux (i.e. a standard LED light bulb).[74]

The organic semiconductors (p- and n-types, π-conjugated compounds) that comprise the photoactive layers of OPVs are ideally suited for utility in harvesting light from artificial sources including LEDs and incandescent bulbs. Fine control of the chemical structure of these compounds allows for tailoring of optoelectronic properties. Design rules related to the p- and n-type organic semiconductors are now well established and optical absorption of photoactive blends can be matched to specific light emission and energy levels optimized to minimize energy loss and maximize operating voltages.[75] In addition, such materials can be (1) prepared *via* atom-economical synthetic procedures rendering them low-cost and accessible and (2) be processed into photoactive films from halogen-free solvents using roll-to-roll compatible coating methods facilitating a transition from laboratory-to-fabrication, as shown in Figure 23B.[76]

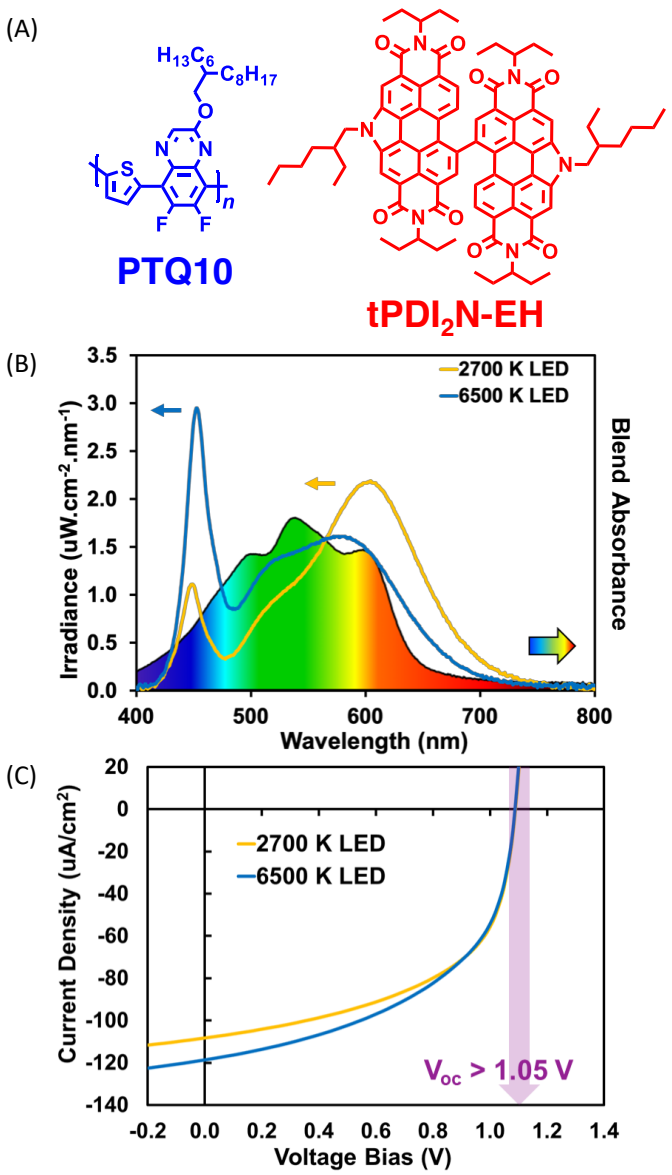

Figure 23. (A) Chemical structures of reported organic semiconductors with demonstrated utility as effective LED light harvesters. PTQ10 is a donor polymer (p-type) and tPDI$_2$N-EH is a non-fullerene acceptor (n-type). Both materials can be made on scale and are processible from halogen-free solvents. (B) Optical absorption spectrum of a PTQ10:tPDI$_2$N-EH bulk-heterojunction film (rainbow) overlapping with the irradiance of warm and cool LED emission. (C) Current-voltage curves of a OPV device with a PTQ10:tPDI$_2$N-EH bulk-heterojunction exhibiting a high open-circuit voltage, a result of tailored electronic energy levels. Reproduced from Ref. 76 with permission from the Royal Society of Chemistry.

2.3 Current and Future Challenges

2.3.1 Materials Design

Most reports on iOPVs have simply used known materials developed for outdoor (1 sun, i.e. 100 mW/cm^2) environments. Thus, there is a great opportunity to develop new custom-made photoactive materials with matched optical absorption to the emission from specific light sources (approximately 400-700 nm). In the design of such organic semiconductor materials, minimizing energy loss and maximizing operating voltages is far more important than reaching higher and higher PCEs as the intended use is to run low power devices. Materials should adopt a facile synthesis and be processible from halogen-free solvents, and thus be compatible with large area roll-to-roll coating. In this case, classic organic semiconductors that have fallen out of favor such as P3HT and PCDTBT may find new life owing to a low-cost synthesis and strong absorption of indoor lighting.

2.3.2 Accurate Photovoltaic Measurements

Standardization of OPV characterization is easier when the reference spectrum is always our Sun (outdoor PV). The task of standardizing non-solar light conversion is a challenge that must be overcome so that reliable power output specifications to design IOT or sensors around are known. Translational equations are used by institutions like NREL, EST-JRC, and AIST to interpret device output under a given reference condition.[77] When the reference condition is not the sun (the case for the majority of iOPV intended uses), existing translational equations are invalid. Since new translational methodologies don't exist yet for indoor PV standards, substantial uncertainty exists in reported indoor PCEs to date, especially when lux meters, as opposed to spectral radiometric equipment, are used to establish incident power. One major current challenge is that the traceable reference cells that are used to measure indoor light power, were calibrated against 1 sun when certified, and therefore don't apply to the indoor spectrum.

2.3.3 Device Engineering

Given the different environmental operating constraints of indoor *vs.* outdoor light harvesting, iOPV requires new design criteria (many ways relaxed relative to outdoor OPV) for

device stack materials that are tailored specifically for indoor conditions. Indeed, oxide UV-soaking does not happen inside, reinforcing the need to use different charge transport layer materials.

2.4 Advances in Science and Technology to Meet Challenges

Matching the indoor light emission wavelength range to the absorbance spectrum of the photoactive layer of the iOPV device can be achieved by a rational design and/or blending of the p- and n-type organic π-conjugated compounds. To meet this challenge faster, the conventional experimental trial-and-error approach would benefit from pairing up with computational simulations and predictions. Feedback loops could also be developed where the results of molecular design and/or processing conditions act as inputs, while output designs and conditions are suggested *via* artificial intelligence tools. Once the formulation of the photoactive layer is selected, another major challenge lies in its processing, especially since processing can dramatically affect the resulting microstructure of the film, and thus, its absorption profile. It needs to be compatible with industrially relevant coating techniques, such as blade- and slot-die coating (c.f. Figure 24) and be conducted in ambient conditions (no spin-coating nor glove-box processing). Photoactive layer formulations that present a performance that is thickness independent also need to be targeted.

A way to ensure a proper comparison of device performance is to move away from PCE and instead compare W/m^2 values produced directly against appropriate reference incident total irradiance spectra. The latter will require the most effort to produce, since many indoor reference spectra, in W/m^2, will need to be collected, but afterwards new reference cells can be certified against these spectra and then the traditional translational equation methodologies can be applied.

Alternatives to charge transport layers requiring post-processing high temperature annealing and UV activation or soaking are required for iOPV prepared on flexible (mostly polymer-based) substrates and operating with indoor light. Such charge extracting interfaces design is a paramount to ensure iOPV operational lifetime in a context where the absence of UV light, humidity and temperatures swings in indoor conditions impact far less the photoactive

layers than under 1 sun conditions. Formulations that can be coated using roll-to-roll compatible techniques without requiring a high temperature annealing, like SnO_2 nanoparticles, need to be further developed. Module fabrication (different form factors) and circuit integration would greatly benefit from electrical engineering inputs, where connection of devices (series or parallel) can tune the module power delivery.

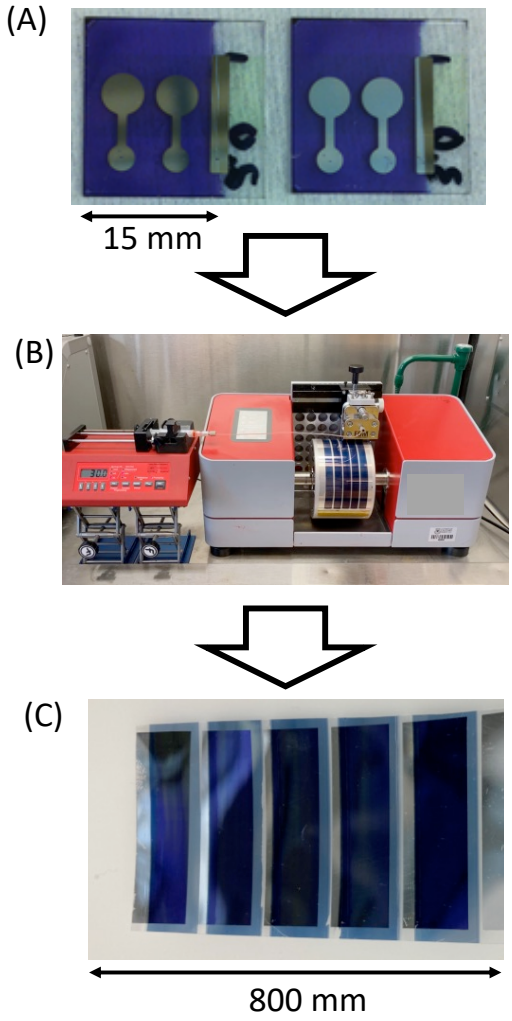

Figure 24. Required transition for OPV application in indoor light recycling. (A) Common lab-scale OPV devices made *via* spin-coating. (B) Affordable roll-coaters for research and development. (C) OPV module (5 cell) made *via* roll-coating using halogen free solvents with current photoactive and interlayer materials. Photos original from Welch lab.

2.5 Concluding Remarks

Overall, the organic photovoltaic for indoor light conversion to electricity presents several challenges for the scientific community that are yet to be tackled. Seizing this opportunity to develop the next generation of iOPV calls for interdisciplinary research efforts, leading to advances within the materials chemistry, device engineering and metrology landscapes. Moreover, three key concepts need to be kept in mind during this endeavor towards a lab-to-fab transition for iOPV devices: scalability, sustainability, and standardization. The scalability and the sustainability of the photoactive layer and charge transport interlayer compounds synthesis and of their thin film coating processes, and the standardization of the device performance evaluation. These key concepts stand as *sine qua non* conditions to ensure a perennial technology transfer from research and development to a widespread adoption of iOPV as power sources for wireless, low-voltage devices.

2.6 Acknowledgements

M.C. thanks the Centre Québécois sur les Matériaux Fonctionnels (CQMF, a Fonds de recherche du Québec – Nature et Technologies strategic network) and A.L. thanks the Canada Research Chairs program for financial support. G.C.W thanks the University of Calgary. This work was authored in part by the National Renewable Energy Laboratory, operated by Alliance for Sustainable Energy, LLC, for the U.S. Department of Energy (DOE) under Contract No. DE-AC36-08GO28308 with writing support for BWL by ARPA-E DIFFERENTIATE program under grant no. DE-AR0001215. The views expressed in the article do not necessarily represent the views of the DOE or the U.S. Government.

Chapter 3 – Experimental section

3.1 Formulations of Polymer Solutions

Printing inks were prepared by dissolving the individual matrices with the desired w/w% (0.5% or 1.0%) of either high regioregular or low regioregular P3HT (74,000 g/mol, determined by the supplier, Ossila) in 4 mL of chloroform. Combinations are shown in Table 1. The molecular weights of the thermoplastic polymers are as follows: 280,000, 540,000, 200,000, and 400,000 g/mol for PS, PMMA, PPC, and PEO respectively. PMMA and PPC were purchased from Scientific Polymer Products while PS and PEO were provided by Sigma Aldrich.

Table 1. Quantities of low and high regioregular P3HT for each matrix

	45% PS (1.8 g)	40% PPC (1.6 g)	35% PMMA (1.4 g)	5% PEO (0.2 g)
0.5% P3HT	9.04 mg	8.04 mg	7.02 mg	1.00 mg
1.0% P3HT	18.18 mg	16.16 mg	14.14 mg	2.02 mg

3.2 Printing

The inks are then transferred into 5 mL screw lock syringes where a G16 nozzle (internal diameter of 1.194 mm) is attached. Subsequently, the syringes are attached securely to the head of the Hyrel EHR printer. A computer aided design (CAD) is then formed by computationally converting a 1 cm cube into 3 cm x 3 cm x 0.03 cm dimensions followed by slicing with 10% infill to form a snake design and a geometric code (G-code). Another set of prints were completed with an infill percentage of 40% for the use in X-ray diffraction, UV-vis and fluorescence spectroscopy experiments. The extrusion width is then adjusted to the gauge thickness + 10% which is 1.313 mm. The print is then completed with one pre-skirt (trace around the circumference of the printing area) at a speed of 10 mm/s.

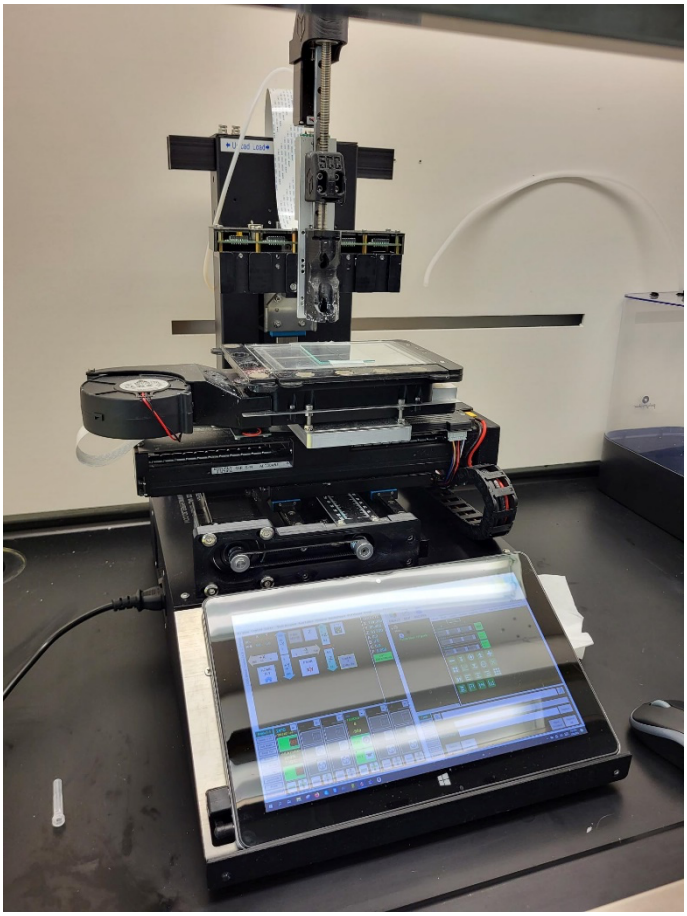

Figure 25. Hyrel EHR printer.

3.3 Blade-coating

Thin films were created by using the blade-coating technique. The same inks used for printing were dropped onto a glass slide and a toothpick was used to spread by hand the ink across the slide.

3.4 Profilometry

Print fidelity of the printed architectures was quantitatively assessed *via* profilometry with the Bruker DektakXT. The DektakXT was set to the “hills and valleys” setting with an appropriate sensitivity depending on the thickness of the printed architectures. For each matrix-P3HT blend, a profile was taken of 3 printed lines situated on the right, middle and left of the print. For every

single profile, the resolution was ca. 5 μm·pt^{-1}. The DektakXT was also used to take a 3D map of a single print for the sake of a visual representative figure.

3.5 Stereomicroscopy

The print fidelity was also qualitatively assessed *via* stereomicroscopy with the Motic SMZ-171.

Figure 26. Motic SMZ-171 stereomicroscope.

3.6 Differential Scanning Calorimetry

The thermal behavior of the printed architectures was investigated by differential scanning calorimetry (DSC). A TA Instruments Q2000 DSC instrument calibrated with high-purity indium was used. DSC samples were prepared by collecting 2-4 mg of the printed material and were sealed in Perkin-Elmer standard aluminum pans. An identical empty DSC pan was used as the reference. The measurements were performed in the temperature range 0-100 °C (PEO), 0-150 °C (PMMA), -40-80 °C (PPC) and 20-150 °C (PS) at a heating rate of 10 °C·min^{-1} under a constant flow of 50 mL·min^{-1} of nitrogen. Only first heating scans were shown. Thermogravimetric

analyses were conducted prior to DSC scans on the samples to determine the onset temperature of the degradation (not shown).

3.7 Rheology

Rheology experiments on the inks were completed at room temperature on a AR200 rheometer to measure the shear-thinning and thixotropy of each matrix as well as each matrix mixed with 1.0% P3HT. For shear-thinning, the shear rates were ramped from 1 to 1000 s^{-1} for 1 minute measuring a data point ever second. For thixotropy measurements, the shear rate was changed every 15 seconds, 5 times, from 0 to 200 s^{-1} measuring 5 data points per session.

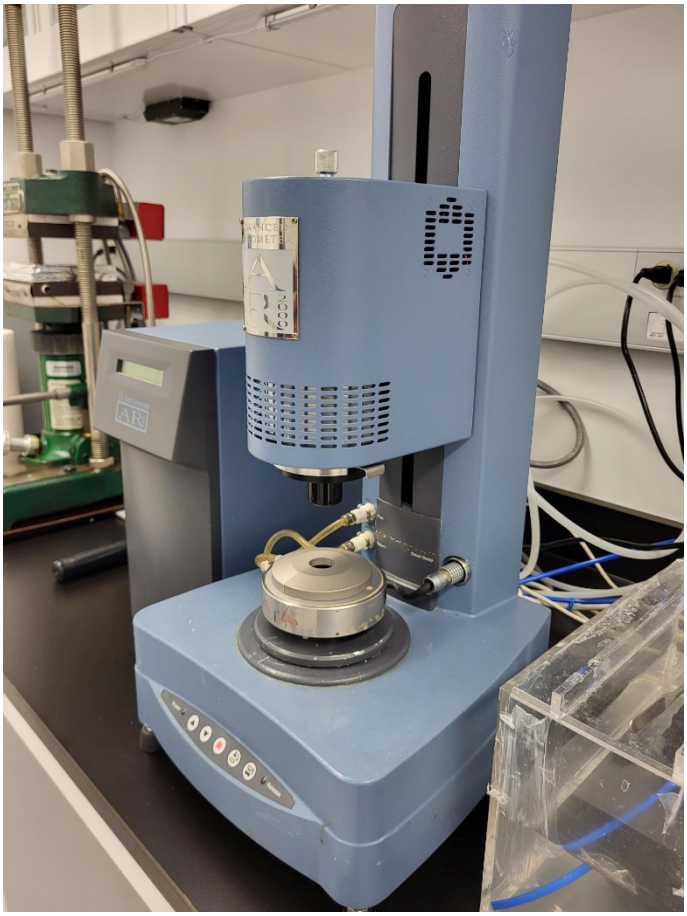

Figure 27. AR200 rheometer.

3.8 UV-visible Spectroscopy

Diffuse reflectance UV-vis measurements of all architectures as well as corresponding thin films that were prepared *via* doctor blade coating method were taken with an Agilent Technologies Cary Series UV-Vis-NIR Spectrometer. For all measurement, the attached integration sphere was used, and a spectral range of 400-800 nm was selected.

3.9 Fluorescence Spectroscopy

Steady-state fluorescence emission spectra were collected using a PTI QuantaMaster 8000 fluorimeter. The samples which were printed on a glass slide were cut to fit inside the cuvette holder of the fluorimeter and to be positioned at an angle of approximately 40 ° from the excitation light. The excitation wavelengths are 475 nm for PS, 525 nm for PEO, 400 nm for PMMA and 525 nm for PPC. For each sample, the excitation and emission slits were set to 3.0 nm. The samples were excited at a wavelength corresponding to their respective absorption maxima, and their emission were recorded in an appropriate range considering the excitation wavelength.

3.10 Optical Microscopy

A Zeiss optical microscope was used to take bright field, cross polarized (90°), as well as epifluorescence images of each printed architecture. For each architecture and every type of image, images were collected at both 5X and 10X magnification.

3.11 X-ray Diffraction

Wide angle X-ray diffraction measurements were done using a Bruker diffractometer operated at 40 kV and 40 mA, using the Cu Kα radiation A scattering background was subtracted (from the glass substrate) from the signal of the prints.

Chapter 4 – Printability assessment of thermoplastic matrices

4.1 Overview

Before attempting to print photoactive materials embedded in thermoplastic matrices, the capability of 3D printing thermoplastics from solution using the direct-ink writing method must first be assessed. In past literature, there has been a variety of interest in blending polymers to meet multiple requirements which originally would not be attainable from the individual materials alone. Specifically in polymer optoelectronics, it can be advantageous to blend semiconducting polymers which obtain the optoelectronic properties with thermoplastics who hold more flexible mechanical properties which can enhance the final mechanical properties of the device as well as assist in ease of processing. The thermoplastic matrices do also confine the conjugated components, which contribute the enhance the electronic properties of the blends.

For example, Nielsen *et al*.[62] compared the percolation in blends of poly(3-hexylthiophene) (P3HT) with both isotactic semicrystalline polystyrene and amorphous polystyrene for the use in optoelectronic devices. It was discovered was that the concentration of the semiconductor could be reduced to as little as 3 wt% without losing efficiency or observing degradation of the final device. In another case, Reichmanis *et al*.[63] spin coated films of P3HT with the insulating polymers polystyrene and polyisobutylene resulting in the acquiring of highly ordered nanofibers of P3HT throughout the blends. It was noted that the enhancement in aggregation properties of the P3HT was due to the unfavourable interactions between the P3HT and the other polymers. Past works have definitively found an inverse relationship between mechanical ductility and electron mobility (molecular ordering) in conjugated polymer systems which is detrimental to the goal of creating flexible electronics. An additional Reichmanis *et al*.[64] case resolved this inversion by blending P3HT with poly(dimethylsiloxane) (PDMS), which, after predeposition processing, formed a stretchable material with high mobility as displayed in Figure 28.

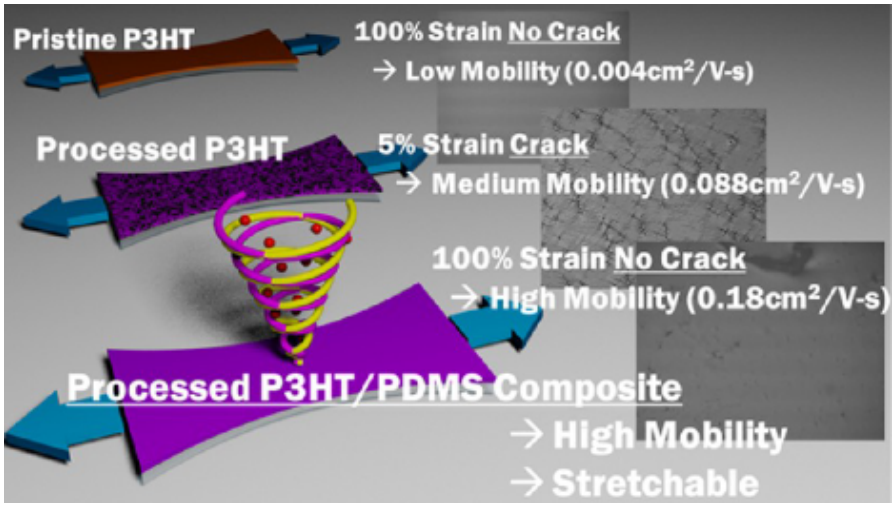

Figure 28. Property comparison between pristine and processed P3HT to a processed P3HT:PDMS composite.[64]

4.2 Objective

Overall, the objective of the work conducted in this chapter is to evaluate the potential of using thermoplastics as matrices to enable the printing of conjugated polymer. Direct-ink writing was the chosen method of processing. Despite that printing from the molten state would manufacture architectures with higher resolution, one must print in solution to print a conjugated polymer.

As mentioned in Figure 22 in Section 1.9.3 the four thermoplastic matrices are of interest in this section which include three amorphous polymers—polystyrene (PS), poly(propylene carbonate) (PPC), poly(methyl methacrylate) (PMMA)—and one semicrystalline—poly(ethylene oxide) (PEO).

4.3 Experimental

The exact experimental methods are described in Chapter 3. To assess the printability of the thermoplastic solutions, rheology measurements, including shear-thinning and thixotropy tests are conducted. The 3D printing is then conducted using the direct-ink writing method. Post printing, profilometry, contact angle, stereo- and optical microscopy measurements are done to compare the agreement between the ink's rheology and their actual printability. The thermal

properties of the resulting printed architectures are also evaluated *via* differential scanning calorimetry (DSC) and to assess the phases in presence *via* X-ray diffraction (XRD).

4.4 Results and Discussion

4.4.1 Justification of the Selection of Matrices

Thermoplastic matrices utilized included PS, PMMA, PPC and PEO. The justification for this selection is the analyses and comparison between the three amorphous polymers—PS, PMMA and PPC—which all differ in their own rheological properties as well as their polarity. In addition, a semicrystalline matrix (PEO) was chosen for its comparison to the amorphous polymers. It is expected that the amorphous polymers would be associated with a higher level of printability as their flexible nature would allow for more uniform architectures. Conversely, it is assumed that printing the semicrystalline PEO would result in poorer quality architectures as semicrystalline polymers are significantly more rigid. In addition, it is expected that the semicrystalline matrix would confine P3HT, increasing the amount of aggregation.

4.4.2 Assessing the Printability of the Matrices

Rheological measurements were conducted to assess their fluid dynamics and correlate it to a behavior that is ideal for 3D printing. Said attributes include shear-thinning as well as thixotropy. Shear-thinning is required for printing as the fluid must become less viscous or "thinner" when a shear force is applied. In addition, thixotropic behavior is required for printable inks as it is necessary to have inks return to their initial viscosity in order for an ink to remain intact after printing.[44] This reasoning is due to the processes the ink undergoes whilst enduring direct-ink writing. Initially, the ink is pushed into the nozzle where it experiences a shear force. Here, the ink must present a shear-thinning behavior in order to correctly flow out of the nozzle. If the inks were to be shear thickening, there would be little to no flow out of the nozzle. Once the ink flows through the nozzle it is deposited onto the print bed. Here, it must return to its initial viscous state quickly in order to solidify in the desired shape architecture, hence, it must display thixotropic behaviour.

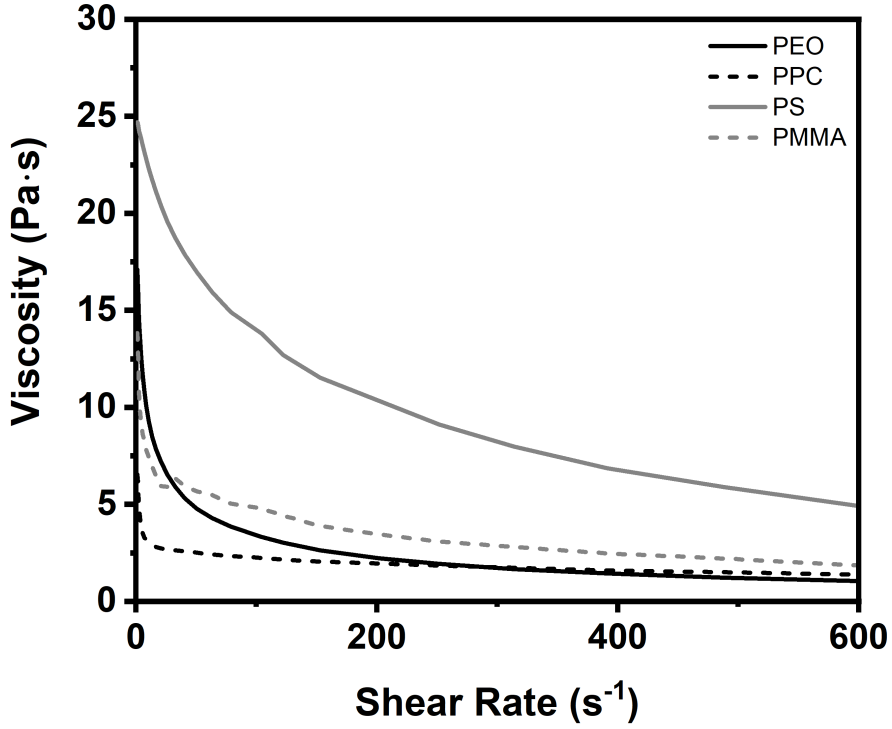

Figure 29. Shear-thinning of the four thermoplastic matrices in $CHCl_3$ at room temperature: PEO 5 w/v%, PPC 40 w/v%, PS 45 w/v% and PMMA 35 w/v%.

Figure 29 displays the shear-thinning nature of all four pristine matrices. Initially, there are differences in the viscosities between each ink where the inks from most viscous to least viscous are PS, PEO, PMMA and then PPC. As demonstrated, PPC and PMMA reduce in viscosity initially at a significantly higher rate in comparison to PS and PEO. This is most likely due to the greater steric hindrance between PS chains and PEO's capability of creating intermolecular interactions. Both of these factors would make it more difficult for PS and PEO to become thinner upon shearing.

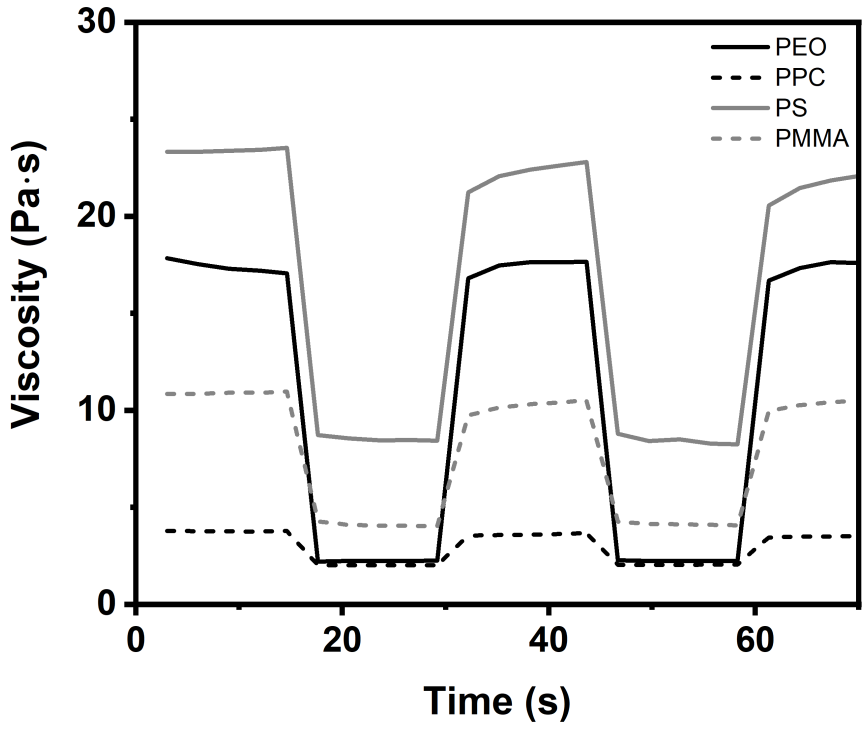

Figure 30. Thixotropy test of the four thermoplastic matrices in $CHCl_3$ at room temperature: PEO 5 w/v%, PPC 40 w/v%, PS 45 w/v% and PMMA 35 w/v%.

Figure 30 visually displays the thixotropic nature of each of the pristine thermoplastic matrices. It should be noted that the initial viscous behaviour for each matrix is consistent with the previously discussed shear-thinning data. Perceivably is the thixotropic nature of each matrix that displays each of them returning back to relatively near the initial viscosity after the applied shear force is removed. The ink was cycled between 0 and 200 s^{-1}, thus when the viscosity is high, the shearing is at 0 s^{-1} and when it is low, the shearing is at 200 s^{-1}. Analytically, one can analyze this data *via* recovery percentage which was calculated by comparing the viscosity at 80% of its total possible velocity during initial shearing to the velocity some time later while the ink is recovering. For PEO, PPC, PS, and PMMA the recovery percentage after 15 seconds (comparing the viscosity after 15 s to the original viscosity) was 45, 73, 67, and 64% respectively. Due to the slight cross-linked nature of PPC, it is expected that it would have the highest recovery percentage. Then, PS and PMMA have very similar recovery percentages due to their similar amorphous nature.

4.4.3 Print Fidelity (Profilometry and Stereomicroscopy)

Print fidelity was evaluated by two different methods. Initially and analytically, by profilometry. Profiling the architecture can precisely find the width of each printed strand which is then compared to the computer aided design's ideal printed width. Furthermore, the ideal and actual width can then be translated into the uniformity factor (U) as mentioned in Equation 3. When a printed architecture exhibits a uniformity factor closer to a value of 1, it is then stated that the original ink has a higher print fidelity.

As presented in Table 2 from lowest to highest printability was PMMA, PPC, PS, and PEO with *U* values of 0.63 ± 0.03, 0.72 ± 0.05, 0.74 ± 0.02, and 0.76 ± 0.10 respectively. This is a similar relation to the aforementioned rheological behaviour including the rate at which the viscosity drops in the shear-thinning tests. The comparison of the uniformity factor and recovery percentage is not necessarily a quantitative comparison but what stands out uniquely enough is that PEO has the highest uniformity factor but lowest recovery percentage of all the matrices. It might have been expected that a faster recovery would lead to a better print. However, perhaps the semicrystalline nature is what gives PEO its printable nature in comparison to the amorphous thermoplastics, as the PEO crystallize upon its solidification (resulting from the evaporation of the solvent) and thus retain its shape. Clearly the uniformity factors displayed in table 2 are far from the ideal value of 1 which is also consistent with the poor contact angle measurements. In this case, the poor printability nature displayed by the solution processing in direct-ink writing will still be used for a proof of concept for the future ability of processing conjugated polymers in the thermoplastics.

Table 2. Uniformity factors of the printed architectures

	PPC	PS	PMMA	PEO
Uniformity Factor	0.72 ± 0.05	0.74 ± 0.02	0.63 ± 0.03	0.8 ± 0.1

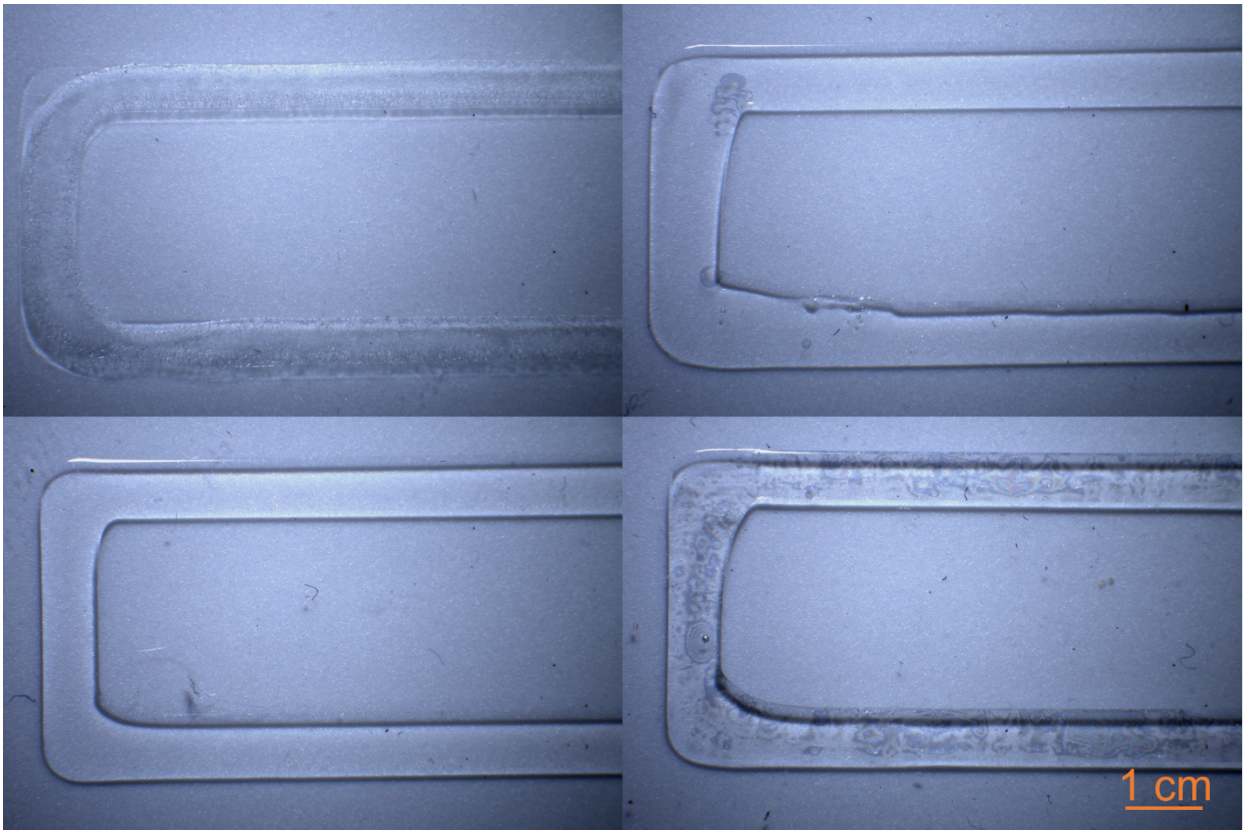

Figure 31. Stereomicroscopy pictures of each matrix. Top left is PEO, top right is PMMA, bottom left is PPC and bottom right is PS.

The print fidelity of each matrix was also evaluated visually from images taken on a stereomicroscope. The advantage the stereomicroscope is that one may observe 3D textures over low magnification which is inherently beneficial for the work presented. As shown in Figure 31, the pictures of the amorphous polymers (PMMA, PPC, and PS) all have glossy textures that clearly have a pronounced, 3D aspect in all x, y, and z directions based on the shadows. In contrast, PEO seems to flatten itself to the glass slide after solvent evaporation and solidification leading to a uniformity factor closer to 1 and has a very textured characteristic due to its semicrystalline behaviour, which is consistent with the contact angle of each matrix.

4.4.4 Differential Scanning Calorimetry

Differential scanning calorimetry (DSC) is a technique which can be used to analytically confirm the phase transitions temperatures of polymers. In this work it is specifically used for

confirmation of the glass transition states of the amorphous polymers as well as the melting point of PEO.

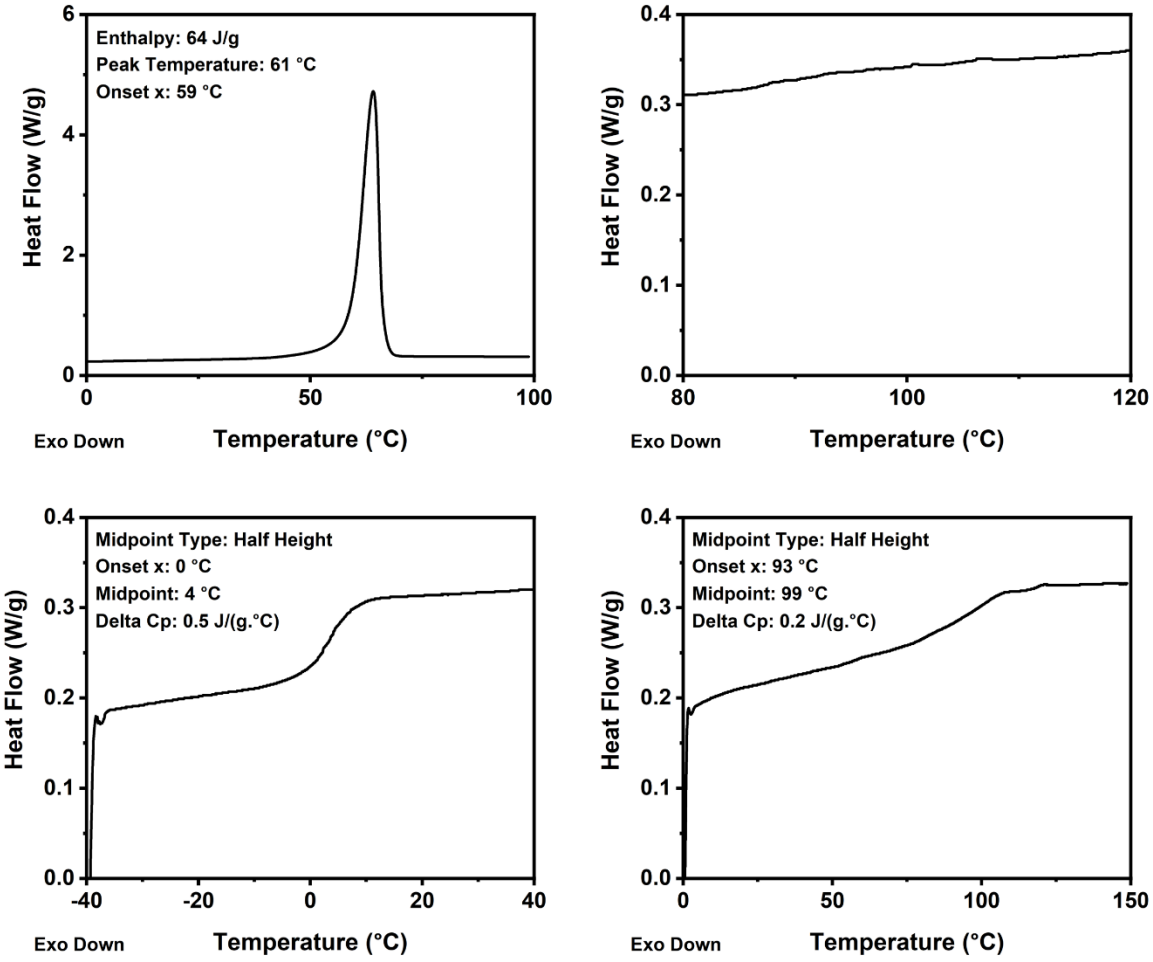

Figure 32. The DSC curves of printed architectures of PEO (top left), PMMA (top right), PPC (bottom left), and PS (bottom right). No T_g was visible for PMMA.

In these DSC experiments, the first scan of heating is used for the analysis. This is specifically so that one can see the thermal history of the material thus being able to see how the polymer is affected thermodynamically by the direct-ink writing process. As presented above, there are three glass transition temperatures and one melting temperature which corresponds to the three amorphous polymers and the one semicrystalline. The transition temperatures for PEO, PPC, and PS are 60, 4, and 99 °C respectively. PEO displays a melting point within a range expected for this compound. Clearly the glass transition of PS is significantly more gradual in

comparison to the one held by PPC. In addition, there is no visible glass transition for PMMA despite multiple attempts to re-run the measurement.

4.4.5 X-ray Diffraction

X-Ray Diffraction patterns were analyzed to confirm the amorphous and/or the semi-crystalline behaviour of each thermoplastic polymer. The crystalline behaviour of a polymer can affect the final post-processed material which is of significant importance to device manufacturing.[62] The crystalline properties of a polymer may change how additives behave within the matrix. On these grounds, it is important to understand the amorphous and/or the semi-crystalline behaviour of a printed thermoplastic before additives are introduced to the system.

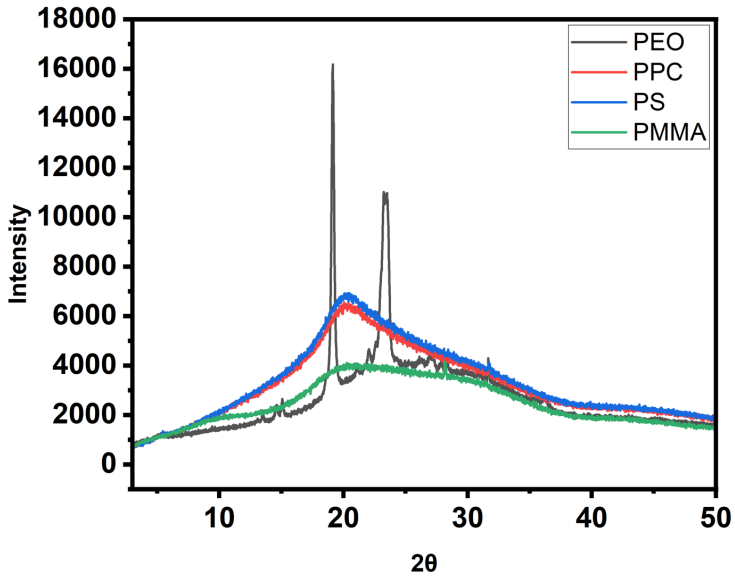

Figure 33. XRD patterns of 3D printed thermoplastic matrices. A different colour scheme was chosen for clarity of this data.

Figure 33 presents the absence/presence of crystallinity of each matrix from XRD patterns. The broad peaks attributed to PPC, PS and PMMA confirm the amorphous behaviour of such polymers which of course, is expected. In contrast, PEO displays significant sharp peaks near a 2Θ of 20 and 24°. The sharp peaks confirm that the printed PEO sample continues to display semicrystalline behaviour even after 3D printed and solidification of the trace that was printed.

4.4.6 Optical Microscopy

Optical microscopy was utilized to characterize visually the 3D printed architectures, but also to confirm their amorphous and/or semi-crystalline nature. The images shown below include bright field and cross polarization pictures. The classical bright field microscopy is useful in its sense of giving an idea of the density throughout the printed architecture which can give perspective on potential imperfections. In terms of cross polarization microscopy, polarized light can reveal the potential crystalline regions within the printed architectures making it advantages for studying the final processed material.

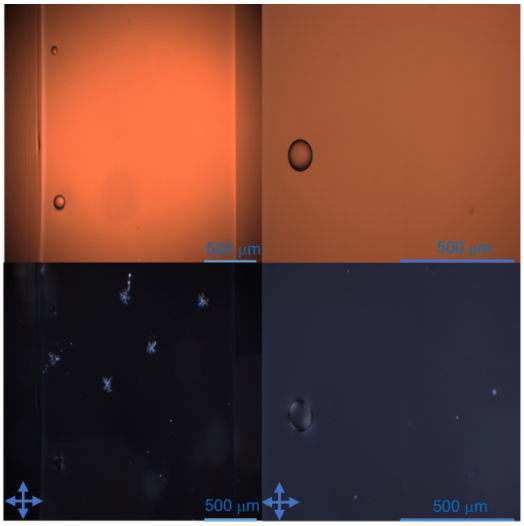

Figure 34. Optical microscope pictures of a PMMA printed architecture. The left side has a magnification of 5X and the right is 10X. The top pictures are bright field microscopy. The bottom pictures are microscopy with a cross polarization at 90°.

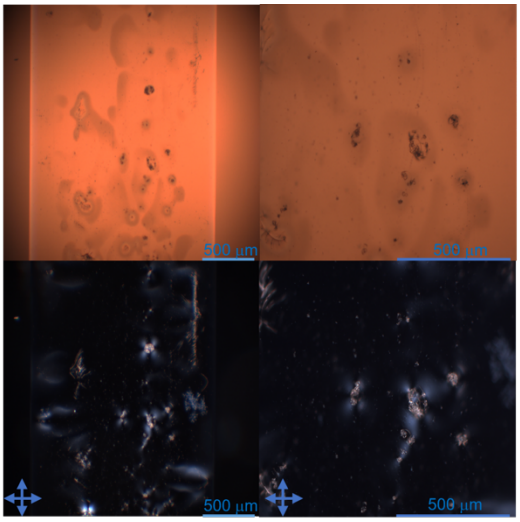

Figure 35. Optical microscope pictures of a PS printed architecture. The left side has a magnification of 5X and the right is 10X. The top pictures are bright field microscopy. The bottom pictures are microscopy with a cross polarization at 90°.

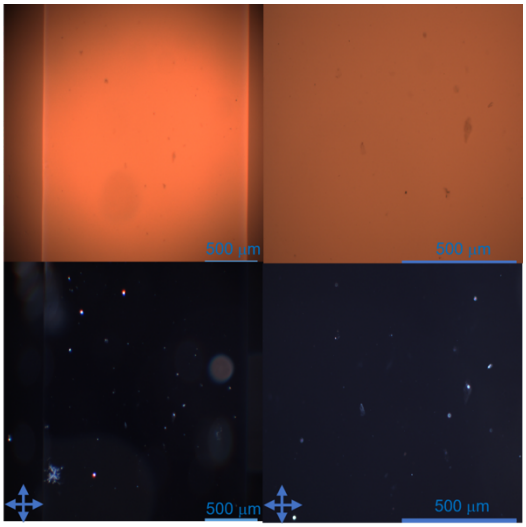

Figure 36. Optical microscope pictures of a PPC printed architecture. The left side has a magnification of 5X and the right is 10X. The top pictures are bright field microscopy. The bottom pictures are microscopy with a cross polarization at 90°.

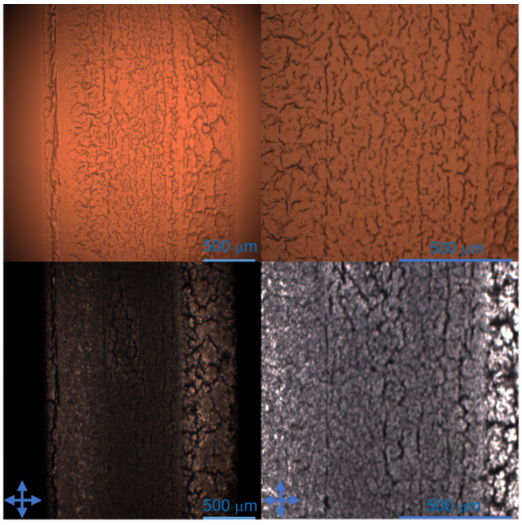

Figure 37. Optical microscope pictures of a PEO printed architecture. The left side has a magnification of 5X and the right is 10X. The top pictures are bright field microscopy. The bottom pictures are microscopy with a cross polarization at 90°.

Above are all of the figures which hold bright field as well as cross polarized pictures of each printed thermoplastic polymer. The polarized pictures can reveal certain defects within the prints. For example, the bright field pictures of PMMA and PPC display how smooth in textured the prints are which is consistent with the stereomicroscope pictures. But the polarized images display certain bright spots which could potentially be air pockets within the dried amorphous polymer. In addition, the bright field images of polystyrene show how streaky the polymer is after printing which is then additionally confirmed by the bright spots in the polarized images. Finally, the bright field images of PEO show how textured of a landscape each architecture has which again is consistent with the stereomicroscopy images. Additionally, the polarized images confirm that these textures are crystalline regions which inherently is due to the semicrystalline nature of the polymer.

4.5 Conclusion

At this point there is no linear relationship of print fidelity and rheological parameters that suggest that any of the thermoplastics is an ideal printing ink. There is no clear relation between the rheological parameters such as shear-thinning, thixotropy and recovery percentage—which are used to predict the print fidelity—with the final printability (uniformity factor) of the material.

That being noted, the uniformity factor is the ultimate deciding factor as to what is an exceptional printed architecture. Therefore, the polymer that displays the highest uniformity factor of all of the polymers is PEO, thus expected to be the best matrix of the four tested for a conjugated polymer. In addition, the semicrystalline nature of PEO may display confinement of a conjugated polymer additive they may induce greater electronic qualities. Despite the poor recovery percentage as well as low contact angles which PEO displays, this can be attributed to the semicrystalline nature of PEO as well as the poor processing nature of direct-ink writing in solution compared to fused filament printing. Although, as mentioned before, direct-ink writing was chosen over printing from the melt because the final objective was to print architectures with a conjugated polymer which must be completed by solution processing. Therefore, the lower quality of printed architectures must be sacrificed in order to process the desired optoelectronic materials.

Chapter 5 – Preparation and Characterization of P3HT-thermoplastic 3D Printed Blends

5.1 Overview

Now that the direct-ink writing capabilities of thermoplastic matrices have been established, the major goal of introducing a conjugated polymer—more specifically, P3HT—into the matrix can be investigated. More precisely, two different concentrations (0.5 and 1.0 wt%) of P3HT with high and low regioregularity have been introduced into each thermoplastic matrix that was studied in Chapter 4. Once the processing was completed, the molecular organization of P3HT in each case is analyzed in order to compare its optoelectronic properties to the conventional 2-dimensional (coating) processing techniques of the current day, i.e. bar-coating.

In order to complete this objective, each concentration (0.5 and 1.0 wt%) of both high and low regioregular P3HT was introduced into each thermoplastic-based ink and subsequently printed *via* direct-ink writing. The inks and architectures were studied for their printability, rheological and thermal properties in the exact same way the pristine thermoplastic matrices were *via* profilometry and stereomicroscopy, shear-thinning and thixotropy analyses, contact angles evaluation, and differential scanning calorimetry. In addition, to investigate the molecular organization and aggregation of P3HT and thermoplastic matrices after the printing, experiments involving X-Ray diffraction, optical microscopy, UV-visible and fluorescence spectroscopy were completed. Specifically, the UV-vis and fluorescence spectroscopy were conducted to compare the nature of the P3HT aggregates in the printed architectures as well as in 2-dimensional thin films, revealed by the ratio of two specific absorbance bands, $A_{0\text{-}0}/A_{0\text{-}1}$ and two specific fluorescence intensity bands, $I_{0\text{-}0}/I_{0\text{-}1}$ corresponding to the first and second electronic transitions which correspond to the aggregation state of the polymer.

5.2 Objective

The general objective of this work is to assess the impact of the 3D printing on the molecular organization of the matrices and the P3HT in the P3HT-thermoplastic blends architectures by comparing it to P3HT-thermoplastic bar-coated films.

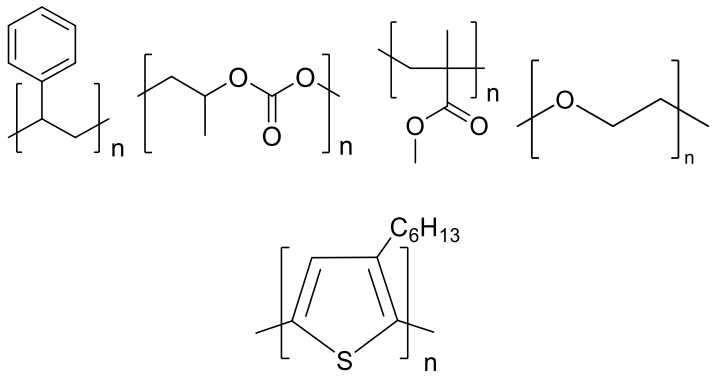

Figure 38. Top: molecular structures from left to right, PS, PPC, PMMA, and PEO. Bottom: molecular structure of P3HT.

Four thermoplastic matrices are of interest in this section which include three amorphous polymers—polystyrene (PS), poly(propylene carbonate) (PPC), poly(methyl methacrylate) (PMMA)—and one semicrystalline—poly(ethylene oxide) (PEO). These thermoplastic matrices were blended with 0.5 and 1.0 wt% of both high and low regioregular P3HT.

5.3 Experimental

The exact experimental methods are described in Chapter 3.

5.4 Results and Discussion

5.4.1 Assessing the Printability of the Matrices

These experiments were completed in addition to the rheological experiments done in Chapter 4 in order to analyze how P3HT impacts the rheological behaviour of the matrices, which in turn would affect the printability. In addition, this will give insight into how the regioregularity of a polymer would impact the rheology and printability of an ink.

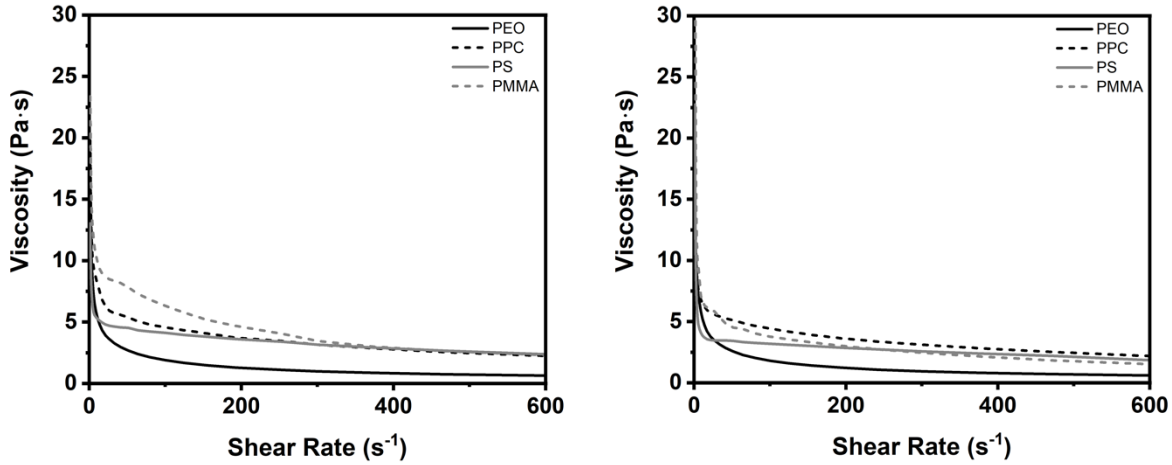

Figure 39. Shear-thinning of high (left) and low (right) regioregular 1.0% P3HT in each thermoplastic matrix.

In Figure 39 the shear-thinning of inks of the variety of matrices with 1.0% high and low regioregular P3HT are shown. The addition of P3HT does impact the rheological properties of the inks but it is assumed that the difference between the addition of 1.0% and 0.5% P3HT would be negligible. Thus, the 1.0% P3HT solutions were solely analyzed. Each ink displays shear-thinning behaviour and the patterns of least viscous to most viscous are PEO, PMMA, PPC, and PS for both high and low regioregular P3HT but in general, all of the matrices with high regioregular P3HT are slightly more viscous in comparison to the low regioregular. This is consistent as the high regioregular P3HT would induce more rigidity into the ink and reduce flow which subsequently increases viscosity.

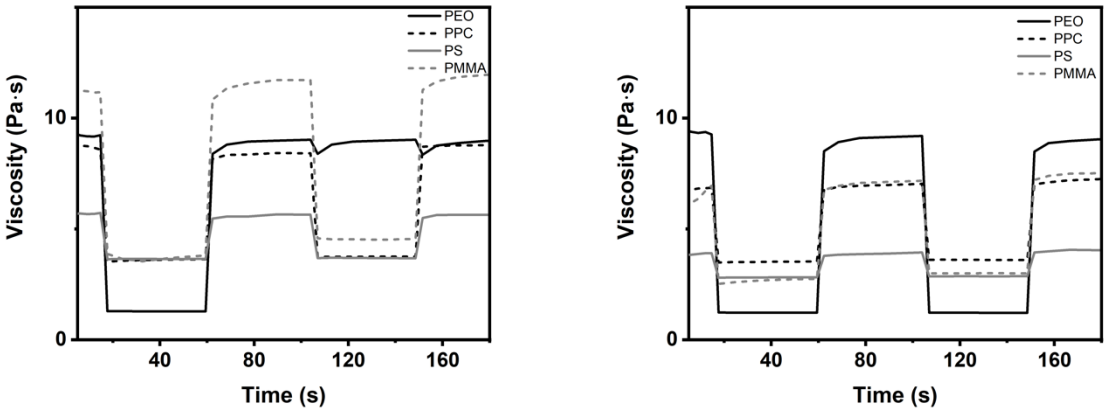

Figure 40. Thixotropy of high (left) and low (right) regioregular 1.0% P3HT in each thermoplastic matrix.

Figure 40 shows the thixotropy analyses of each matrix with both high and low regioregular P3HT are shown. The initial viscosities displayed here are consistent with the ones already discussed during the shear-thinning experiments. There is significant difference in recovery between the high and low regioregular samples. The recovery percentage after 45 seconds for the high regioregular samples with the matrices of PEO, PPC, PS, and PMMA were 91, 95, 95, and 97% respectively. In terms of the low regioregular samples, the recovery percentages were 92, 98, 97, and 97% for PEO, PPC, PS, and PMMA respectively. But it is also evident after investigation of the figures above that when using high regioregular P3HT, the recovery of each ink continuously drops over multiple outbreaks to the shear force. Inherently, when using amorphous matrices, the recovery percentages were higher when blending with low regioregular P3HT.

5.4.2 Print Fidelity

Table 3. Uniformity factors of printed architectures with both high regioregular (HR) and low regioregular (LR) P3HT

Variable	PPC	PS	PMMA	PEO
0.5% HR P3HT	1.36 ± 0.06	1.4 ± 0.1	1.60 ± 0.05	1.5 ± 0.1
0.5% LR P3HT	1.42 ± 0.09	1.43 ± 0.06	1.6 ± 0.2	1.40 ± 0.06
1.0% HR P3HT	1.53 ± 0.02	1.5 ± 0.1	1.8 ± 0.3	1.6 ± 0.1
1.0% LR P3HT	0.86 ± 0.03	1.04 ± 0.08	1.5 ± 0.1	1.1 ± 0.9

In Table 3 the uniformity factors of the printed matrices with 1.0% and 0.5% P3HT (both high and low regioregular) are presented. In all cases except for 1.0% LR P3HT in a matrix of PPC the uniformity factor is above 1. As the most ideal printability is demonstrated by a uniformity factor that approaches a value of 1, this is not ideal. This may suggest that the introduction of any type of P3HT into a matrix will result in a greater level of ink spreading. The best prints for each matrix which are analytically confirmed *via* uniformity factor are all held by 1.0% LR P3HT. The uniformity factors are as follows: 0.86 ± 0.03, 1.04 ± 0.08, 1.47 ± 0.12, and 1.07 ± 0.85 for PPC, PS, PMMA, and PEO respectively. When considering an absolute value difference from a uniformity factor of 1, the most printable to least printable inks are PS, PEO, PPC, and PMMA. In terms of regioregularity, it is consistent with the evident fact that the increase in flexibility and miscibility of the low regioregular P3HT would allow for an increase in the printability of the material.

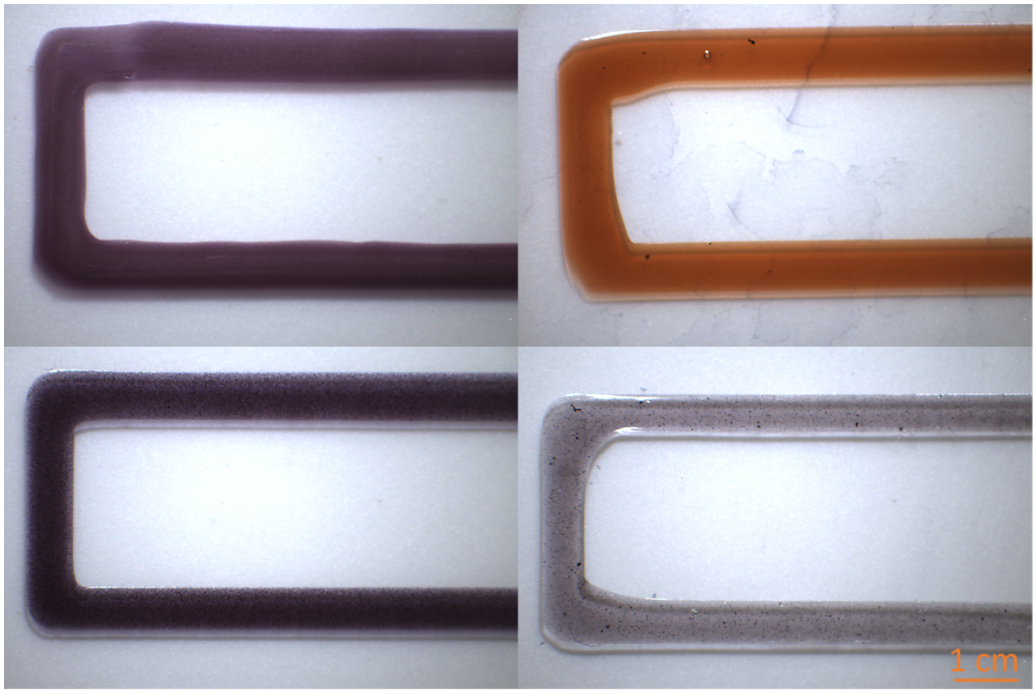

Figure 41. Stereomicroscopy pictures of each matrix with 0.5% high regioregular P3HT. Top left is PEO, top right is PMMA, bottom left is PPC, and bottom right is PS.

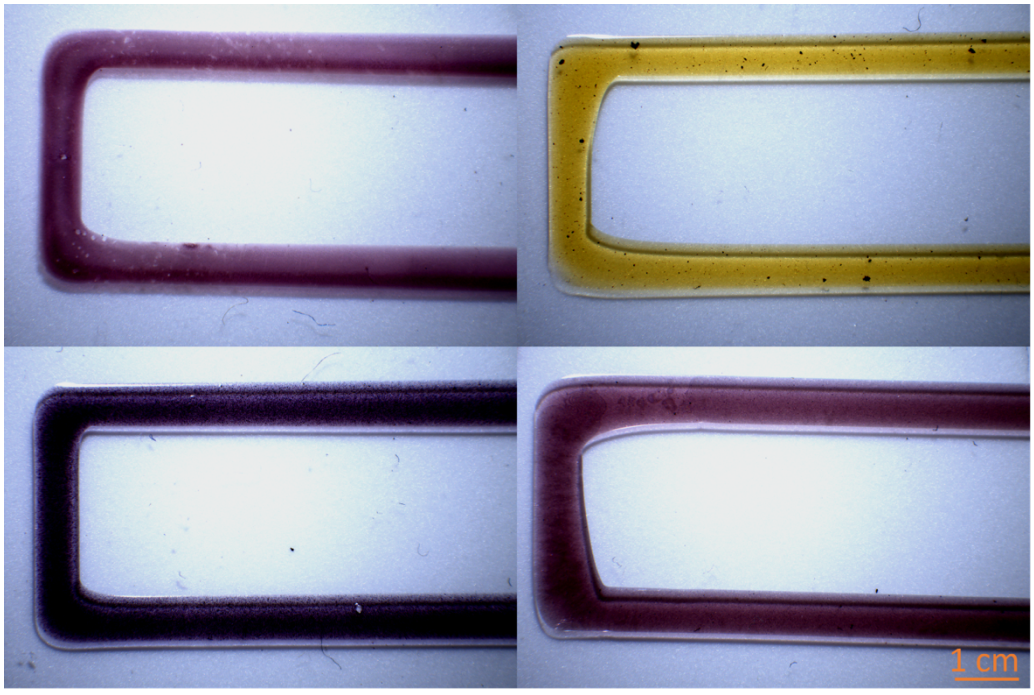

Figure 42. Stereomicroscopy pictures of each matrix with 0.5% low regioregular P3HT. Top left is PEO, top right is PMMA, bottom left is PPC, and bottom right is PS.

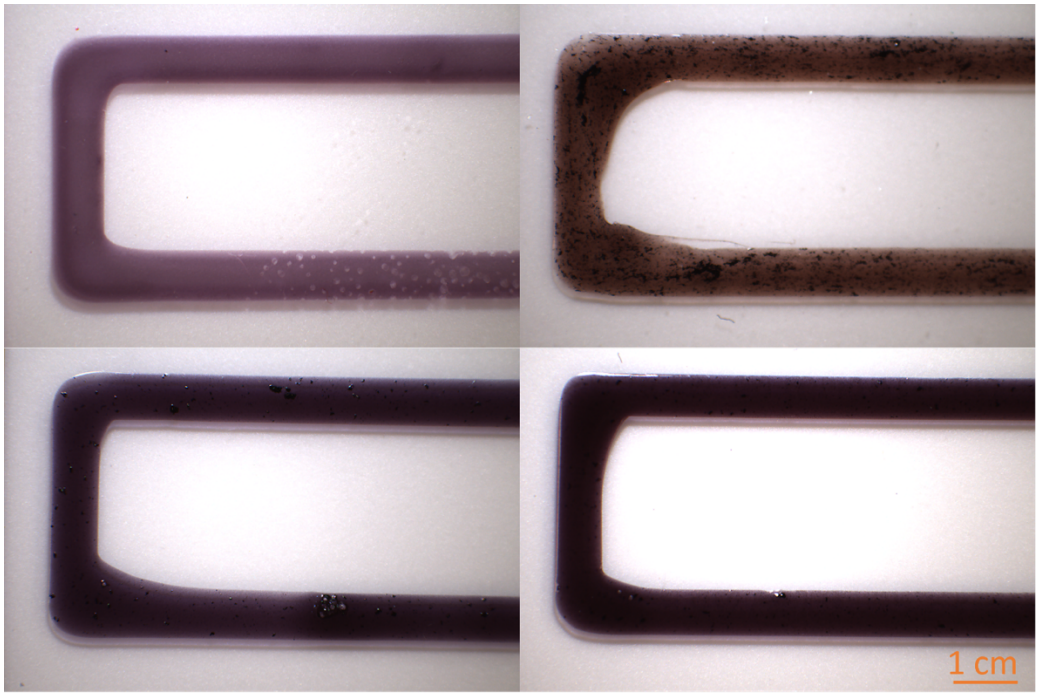

Figure 43. Stereomicroscopy pictures of each matrix with 1.0% high regioregular P3HT. Top left is PEO, top right is PMMA, bottom left is PPC, and bottom right is PS.

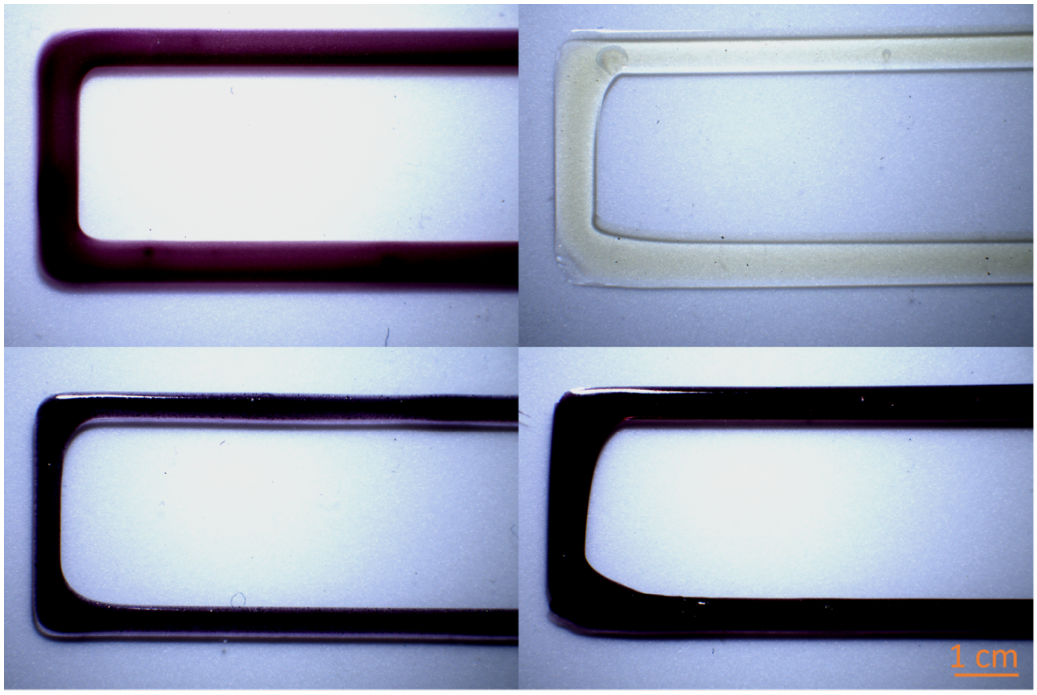

Figure 44. Stereomicroscopy pictures of each matrix with 1.0% low regioregular P3HT. Top left is PEO, top right is PMMA, bottom left is PPC, and bottom right is PS.

Subsequently the print fidelity of each matrix was evaluated visually by stereomicroscopy which has the advantage of observing 3D textures over low magnification which is inherently beneficial for this work. As set forward in Figures 41, 42, 43, and 44, images of each matrix with varying concentrations of high and low regioregular P3HT additives are displayed. As a generality, the 1.0% P3HT samples are darker coloured in comparison to the 0.5% which is optically consistent with the higher concentration of P3HT. In addition, high regioregular samples usually have more obvious small aggregates of P3HT in the matrices than the low regioregular which is understandable based on the higher miscibility the low regioregular P3HT distributes. The evaluation of the solubility may be done using $(\delta_A - \delta_B)^2$, where δ corresponds to the solubility parameter.

According to the solubility parameters reported in Table 4, it is possible to predict the preferential segregation of the P3HT either in the solvent of the formulation (chloroform) or in the polymer matrices. In all cases, P3HT would be in the aggregated state in the matrix, except for the PMMA, which correlates with the optical observation, where the samples are orange, indicative of a non-aggregated P3HT state.

Table 4. Solubility parameters comparison

Component of Blend	δ Solubility Parameter ($MPa^{1/2}$)	Comparison P3HT in solvent vs. matrix	Preference
Chloroform Solvent	18.7	-	-
P3HT	19.1	-	-
PMMA	19.0	0.2 vs. 0.01	PMMA
PPC[66]	20.4	0.2 vs. 1.7	$CHCl_3$
PS	18.3	0.2 vs. 0.6	$CHCl_3$
PEO	20.8	0.2 vs. 3.9	$CHCl_3$

Most notably, the PMMA samples are unique in their colour as well as their ability to not follow the generalities shown by the other matrices. PMMA has shown a more brown, orange or yellow colour in comparison to the usual purple colour which P3HT presents in the other matrices. The orange colour is due to the less aggregated form of P3HT rather than the aggregated form which would be purple. Uniquely, the colour of the PMMA samples become darker when increasing concentrations of high regioregular P3HT but actually become lighter when increasing concentrations of low regioregular P3HT. This will be analyzed more in depth further on in this work where UV-vis and fluorescence spectroscopy are employed.

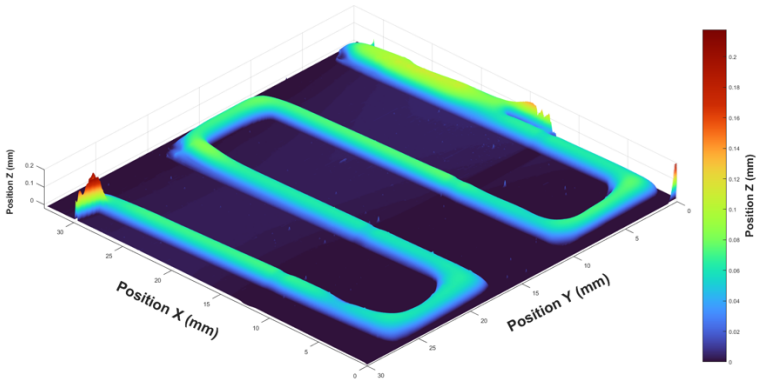

Figure 45. Representative profile of a low regioregular 1.0% P3HT in PMMA printed architecture.

Figure 45 shows a representative profile of a printed architecture. This visually shows the depth and width of the 3D printed figurines. This representation gives an idea of the layout of each print for the reader, where one can see that it is relatively uniform along the printed traces.

5.4.3 UV-vis Spectroscopy

UV-vis spectroscopy is useful for quantitatively probing the aggregation of P3HT within each matrix. Due to the solid-state nature and thickness of the printed architectures, diffuse reflectance UV-vis spectroscopy within an integration sphere was employed by opposition to transmission spectroscopy. After experimental measurements, the $A_{0\text{-}0}/A_{0\text{-}1}$ transitions were analyzed which directly reflect the aggregation states of P3HT. Subsequently the $A_{0\text{-}0}/A_{0\text{-}1}$ transitions of the printed architectures were compared to the transitions of P3HT processed in the same matrices but by the 2D processing coating method of blade coating. This method is

necessary to learn the differences and potential benefits of 3D processing conjugated polymers in contrast to 2D processing methods.

The ratio of the A_{0-0} transition to the A_{0-1} transition can be used to calculate the exciton bandwidth as well as give a better depiction of the molecular environment as displayed in Figure 18. For example, a stronger A_{0-0} transition compared to a A_{0-1} translates to a lower exciton bandwidth which indicates a higher conjugation length and an increase in the planar behaviour of the polymer backbone.[54] Therefore, UV-vis spectroscopy adds a depth of insight into the supramolecular chemistry of P3HT aggregates present.

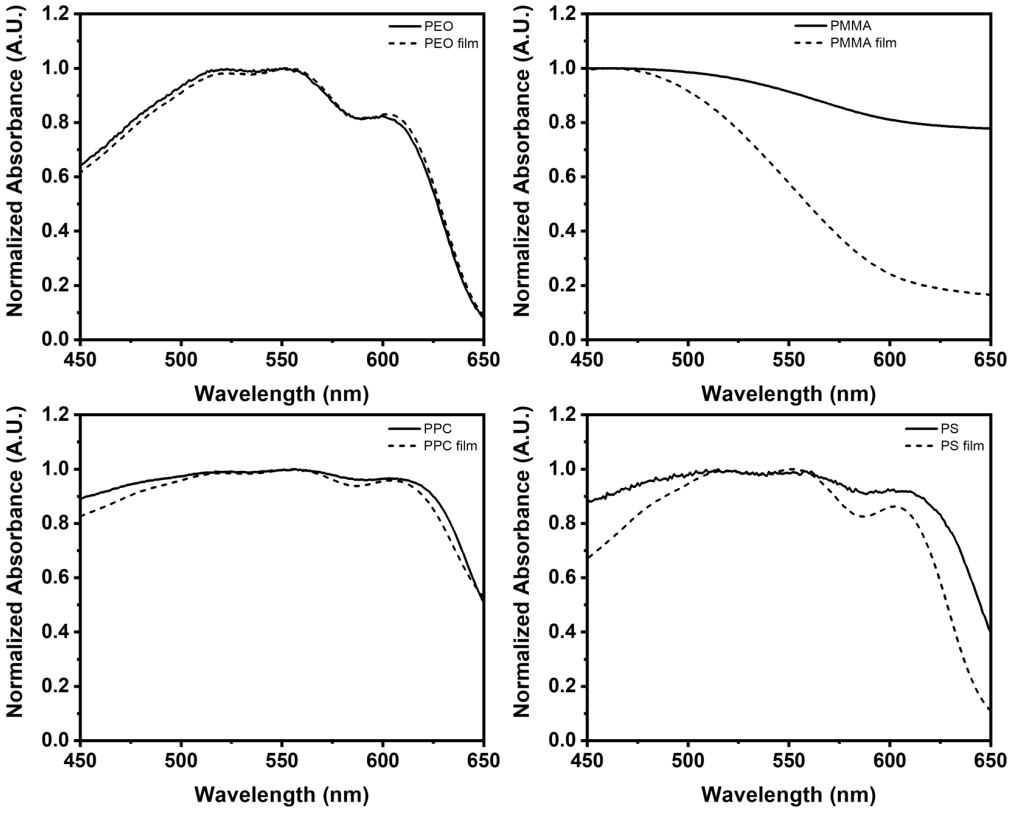

Figure 46. Normalized UV-vis spectra of each thermoplastic matrix with 0.5% high regioregular P3HT printed *via* direct-ink writing compared to 2D films. The solid line relates to the 3D printed architectures whilst the dashed line refers to the 2D films. While the Y axis is presented in absorbance, the actual measurement was recorded in reflection percentage and converted to absorbance.

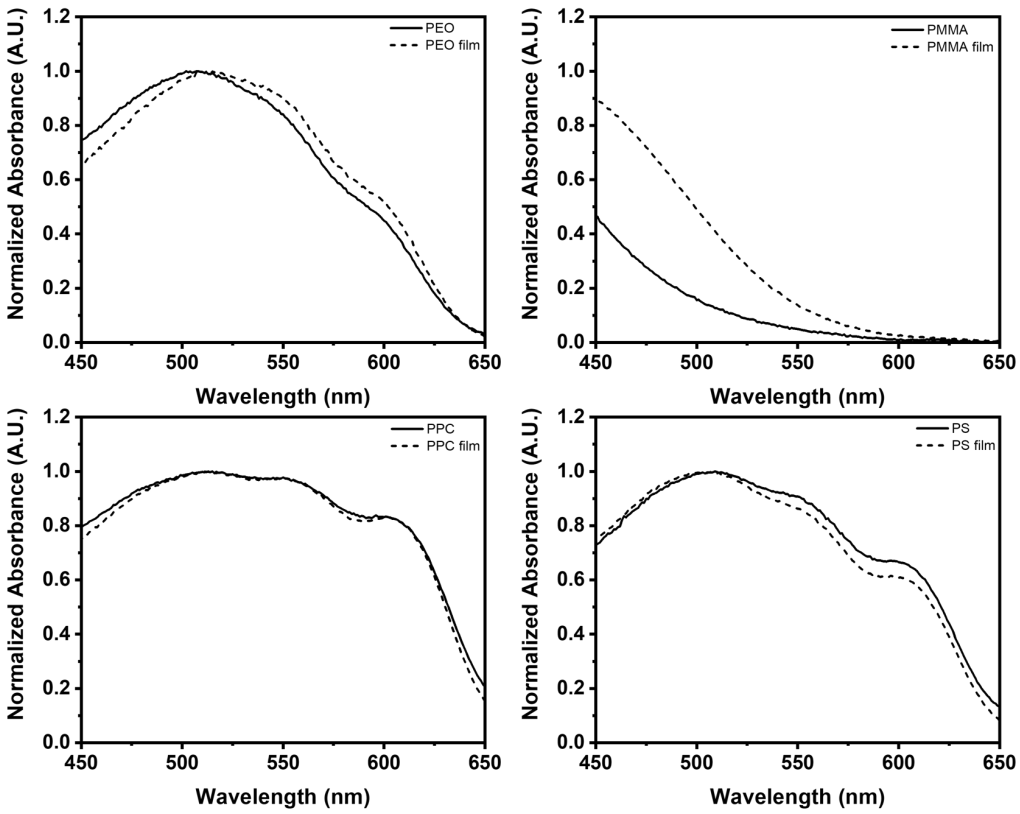

Figure 47. Normalized UV-vis spectra of each thermoplastic matrix with 0.5% low regioregular P3HT printed *via* direct-ink writing compared to 2D films. The solid line relates to the 3D printed architectures whilst the dashed line refers to the 2D films. While the Y axis is presented in absorbance, the actual measurement was recorded in reflection percentage and converted to absorbance.

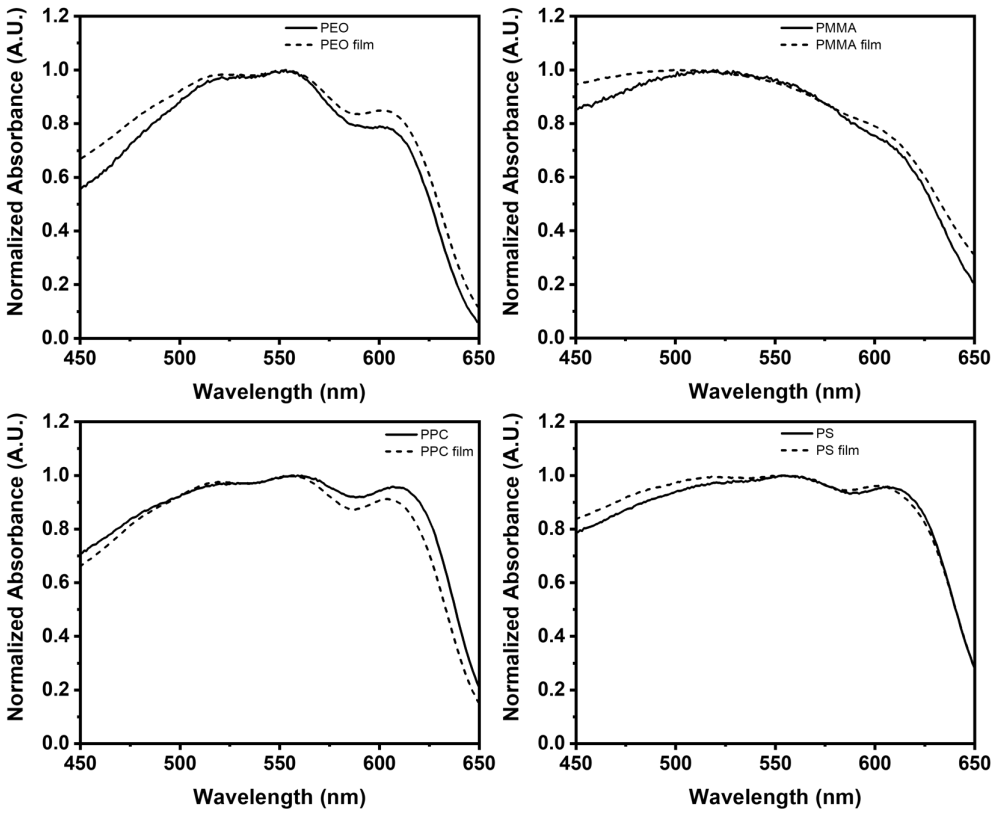

Figure 48. Normalized UV-vis spectra of each thermoplastic matrix with 1.0% high regioregular P3HT printed *via* direct-ink writing compared to 2D films. The solid line relates to the 3D printed architectures whilst the dashed line refers to the 2D films. While the Y axis is presented in absorbance, the actual measurement was recorded in reflection percentage and converted to absorbance.

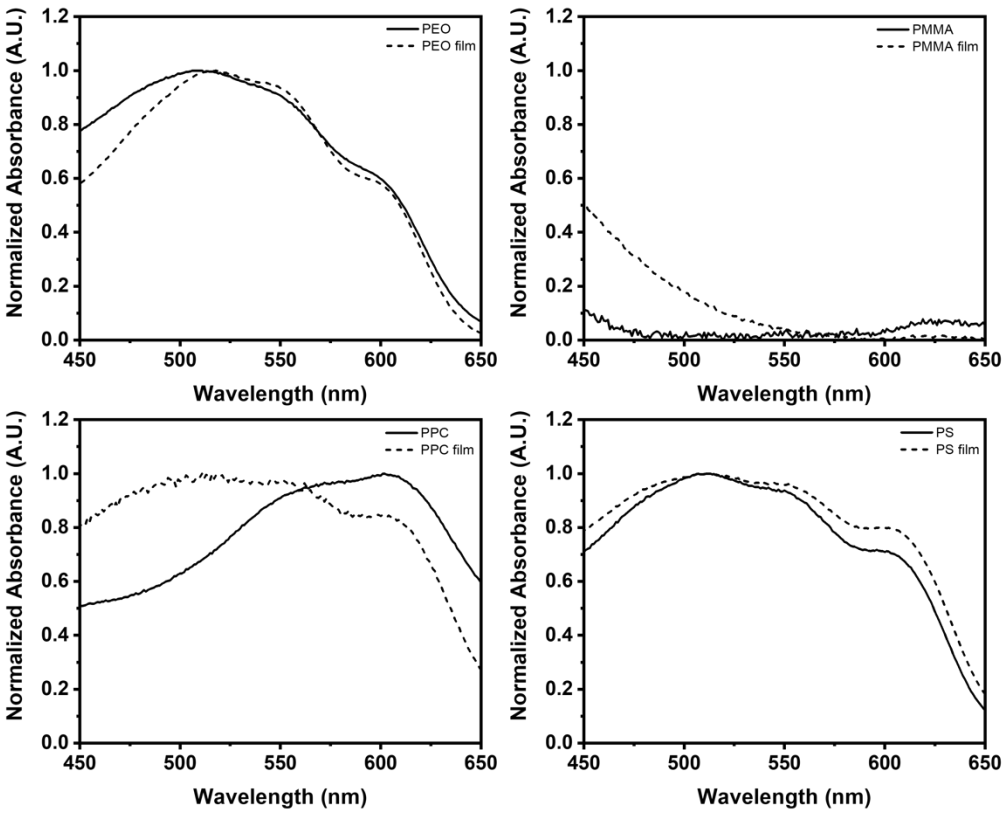

Figure 49. Normalized UV-vis spectra of each thermoplastic matrix with 1.0% low regioregular P3HT printed *via* direct-ink writing compared to 2D films. The solid line relates to the 3D printed architectures whilst the dashed line refers to the 2D films.

Above—in Figures 46, 47, 48, and 49—the normalized UV-vis spectra of the matrices with varying concentrations of high and low regioregular P3HT are presented; each with their corresponding 2D processed films. Before the quantitative analysis of the A_{0-0}/A_{0-1} transitions, it should be noted that in comparison between high and low regioregular P3HT printed architectures, the A_{0-0} peak is more pronounced in high regioregular samples as well as non-existent in the PMMA samples. This is consistent with the increase in the miscibility observed in the PMMA matrix as well as the low regioregular samples. Higher miscibility will lead to less P3HT aggregates due to the increased spreading of the P3HT throughout the matrix. Additionally, blending low regioregular P3HT will form less aggregates than high regioregular because of the lack of intramolecular interactions leading to crystallinity.

Table 5. $A_{0\text{-}0}/A_{0\text{-}1}$ transitions of P3HT in printed architectures with both high regioregular and low regioregular P3HT

Variable	PPC	PS	PMMA	PEO
0.5% HR P3HT	1.09	1.07	n/a	1.08
0.5% LR P3HT	1.09	1.09	n/a	1.10
1.0% HR P3HT	1.09	1.10	n/a	1.09
1.0% LR P3HT	1.06	1.09	n/a	1.09

Table 6. $A_{0\text{-}0}/A_{0\text{-}1}$ transitions of P3HT in 2D processed films with both high regioregular and low regioregular P3HT

Variable	PPC	PS	PMMA	PEO
0.5% HR P3HT	1.09	1.09	n/a	1.09
0.5% LR P3HT	1.09	1.10	n/a	1.09
1.0% HR P3HT	1.09	1.08	n/a	1.09
1.0% LR P3HT	1.10	1.09	n/a	1.09

In Table 6, the $A_{0\text{-}0}/A_{0\text{-}1}$ transitions of P3HT in both the printed architectures as well as the 2D thin films are presented. Noticeably there is little to no variation in the transition ratios between the varying matrices as well as between 3D and 2D processed materials. This is indicative of direct-ink writing having the quality of processing materials which would have very similar optoelectronic efficiencies to those which are processed *via* current 2D techniques. Thus, supporting the possibility of 3D processed optoelectronic devices.

5.4.4 Fluorescence Spectroscopy

Fluorescence spectroscopy was implicated to compliment the UV-vis experiments. Due to the fluorescent nature of P3HT, one may observe the $A_{0\text{-}0}/A_{0\text{-}1}$ as well as the $I_{0\text{-}0}/I_{0\text{-}1}$ transitions.

Theoretically, these transitions within the two separate experiments should be an exact mirror image of each other. Although the literature suggests that ,due to absorbance being an excitation process and fluorescence being a relaxation process, fluorescence is more sensitive than UV-visible spectroscopy to the environment of the molecule is in.[56] Therefore, absorbance (UV-vis) spectroscopy would give more information about the aggregates themselves whereas fluorescence spectroscopy would give more information about how the P3HT aggregates interact with the matrix in which they are processed.

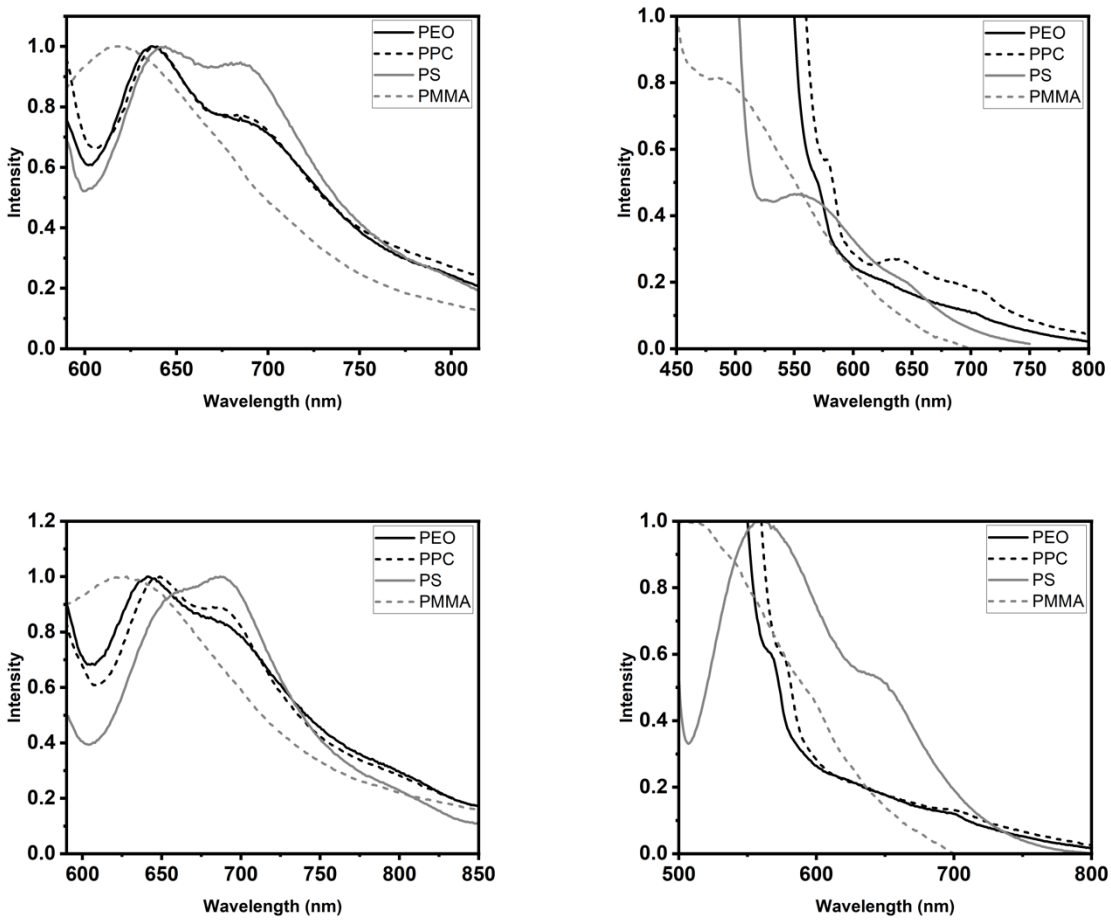

Figure 50. Normalized fluorescence spectra of each thermoplastic:P3HT blend. Top row is 0.5% samples and bottom row is 1.0%. Left side is high regioregular while right is low regioregular.

Table 7. $I_{0\text{-}0}/I_{0\text{-}1}$ transitions of P3HT in printed architectures with both high regioregular and low regioregular P3HT

Variable	PPC	PS	PMMA	PEO
0.5% HR P3HT	0.93	0.94	n/a	0.93
0.5% LR P3HT	0.91	0.86	n/a	0.91
1.0% HR P3HT	0.94	0.96	n/a	0.93
1.0% LR P3HT	0.82	0.87	n/a	0.81

Table 7 presents the $I_{0\text{-}0}/I_{0\text{-}1}$ fluorescence transitions. In comparison to the $A_{0\text{-}0}/A_{0\text{-}1}$ transitions, they are noticeably lower values. This indicates that the matrices allow for more relaxation pathways once P3HT is excited. It is also distinguishable that the low regioregular matrices have lower $I_{0\text{-}0}/I_{0\text{-}1}$ values than high regioregular P3HT samples. This is most likely due to the higher miscibility the low regioregular P3HT shows within each matrix. The higher miscibility allows for more interactions with the matrices and thus allowing for more relaxation pathways. Also, the $I_{0\text{-}0}/I_{0\text{-}1}$ transitions in the high regioregular samples tend to increase with an increase in concentration whilst the low regioregular samples tend to decrease with an increase in concentration. This is consistent with the miscibility and solubility differences that the low and high regioregular P3HT samples possess.

5.4.5 Differential Scanning Calorimetry

Differential scanning calorimetry (DSC) is used to confirm the phase transitions of polymers and see how they are affected by the presence of P3HT. In this chapter specifically, it is used to confirm the glass transition temperatures of the amorphous polymers and the melting point of PEO after the inclusion of small amounts of P3HT.

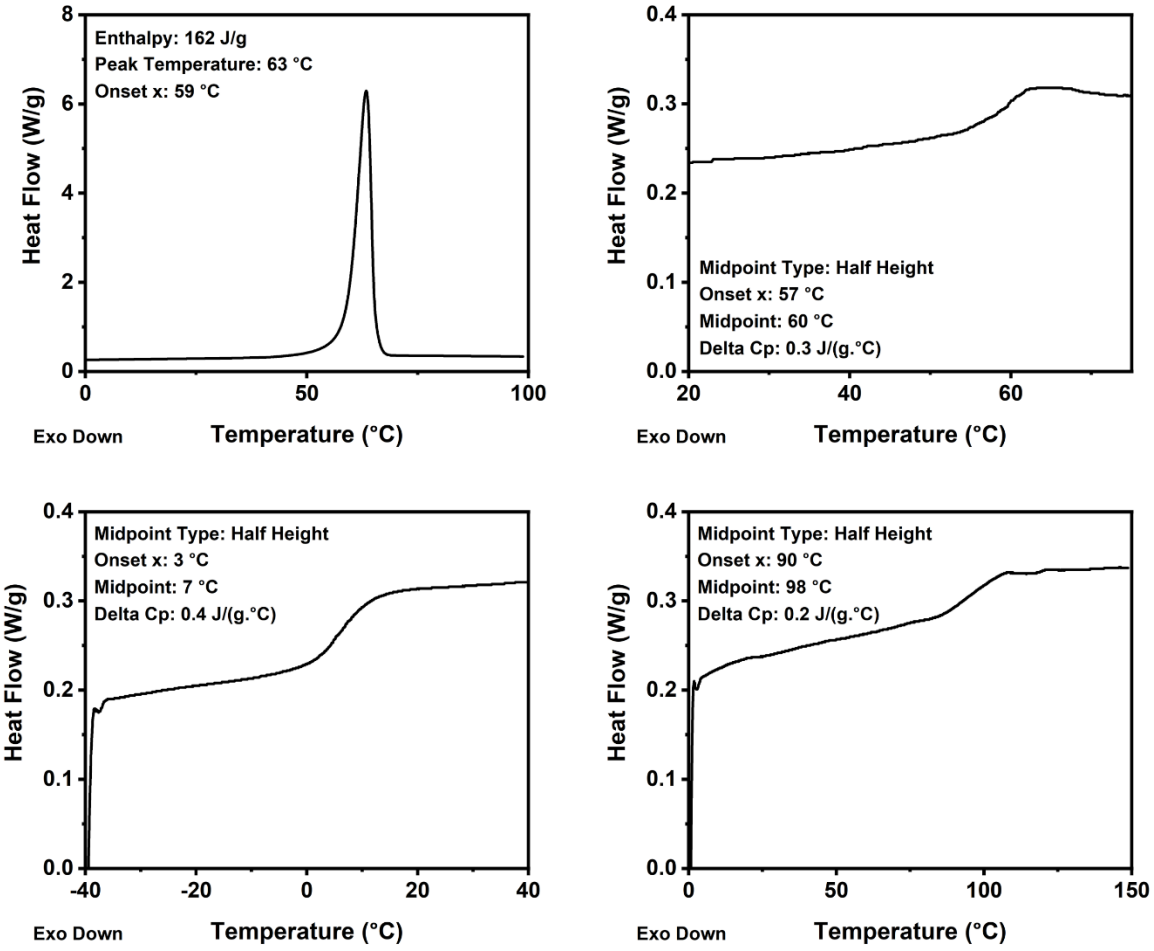

Figure 51. The DSC curves of printed architectures of PEO (top left), PMMA (top right), PPC (bottom left), and PS (bottom right) with 0.5% high regioregular P3HT.

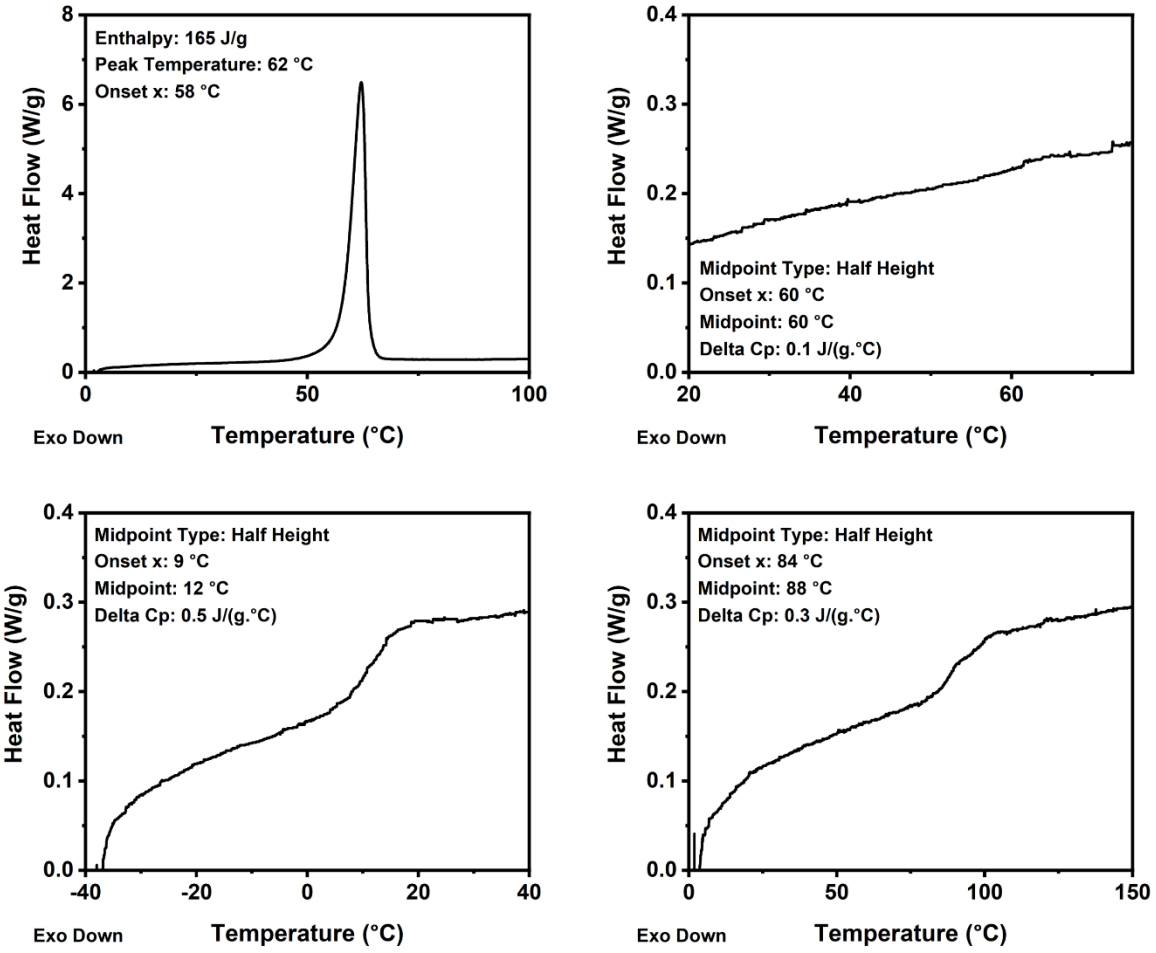

Figure 52. The DSC curves of printed architectures of PEO (top left), PMMA (top right), PPC (bottom left), and PS (bottom right) with 0.5% low regioregular P3HT.

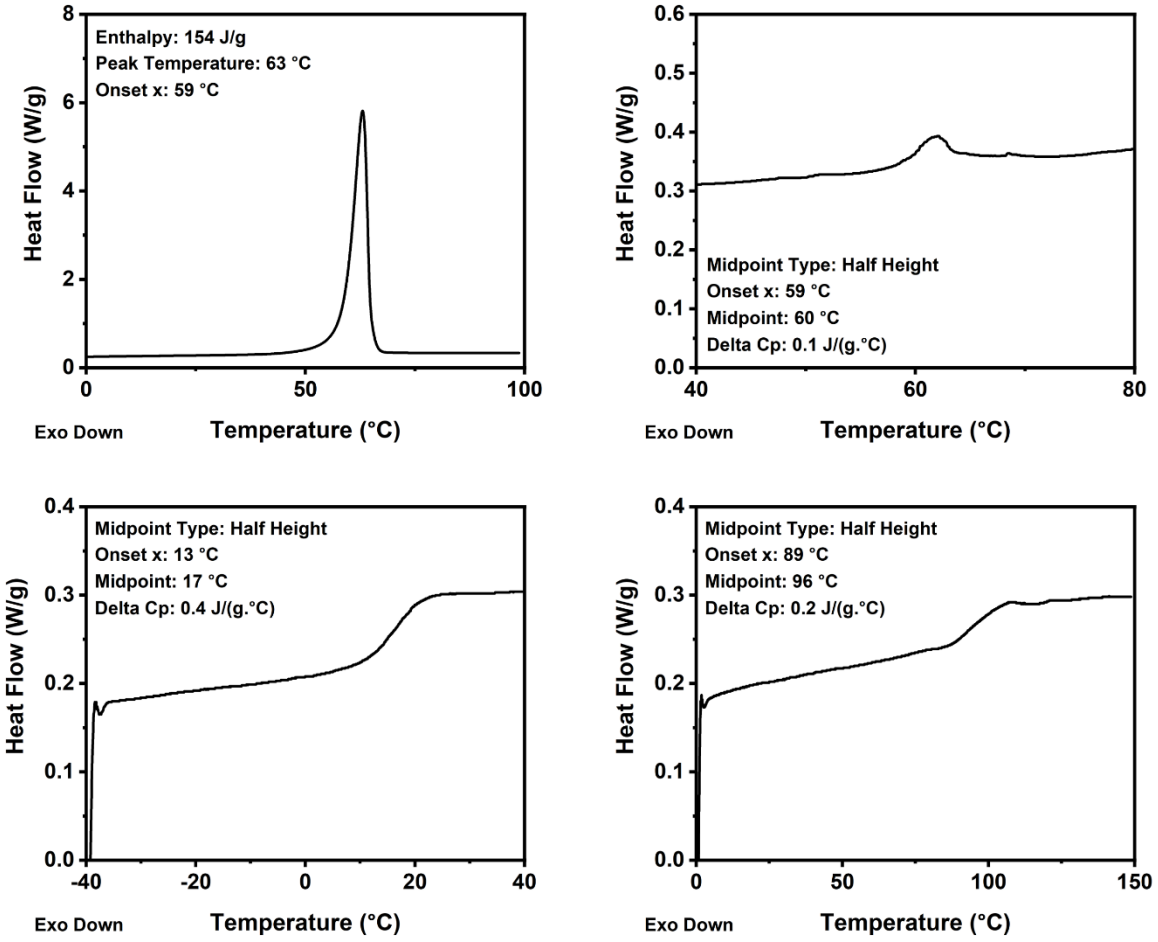

Figure 53. The DSC curves of printed architectures of PEO (top left), PMMA (top right), PPC (bottom left), and PS (bottom right) with 1.0% high regioregular P3HT.

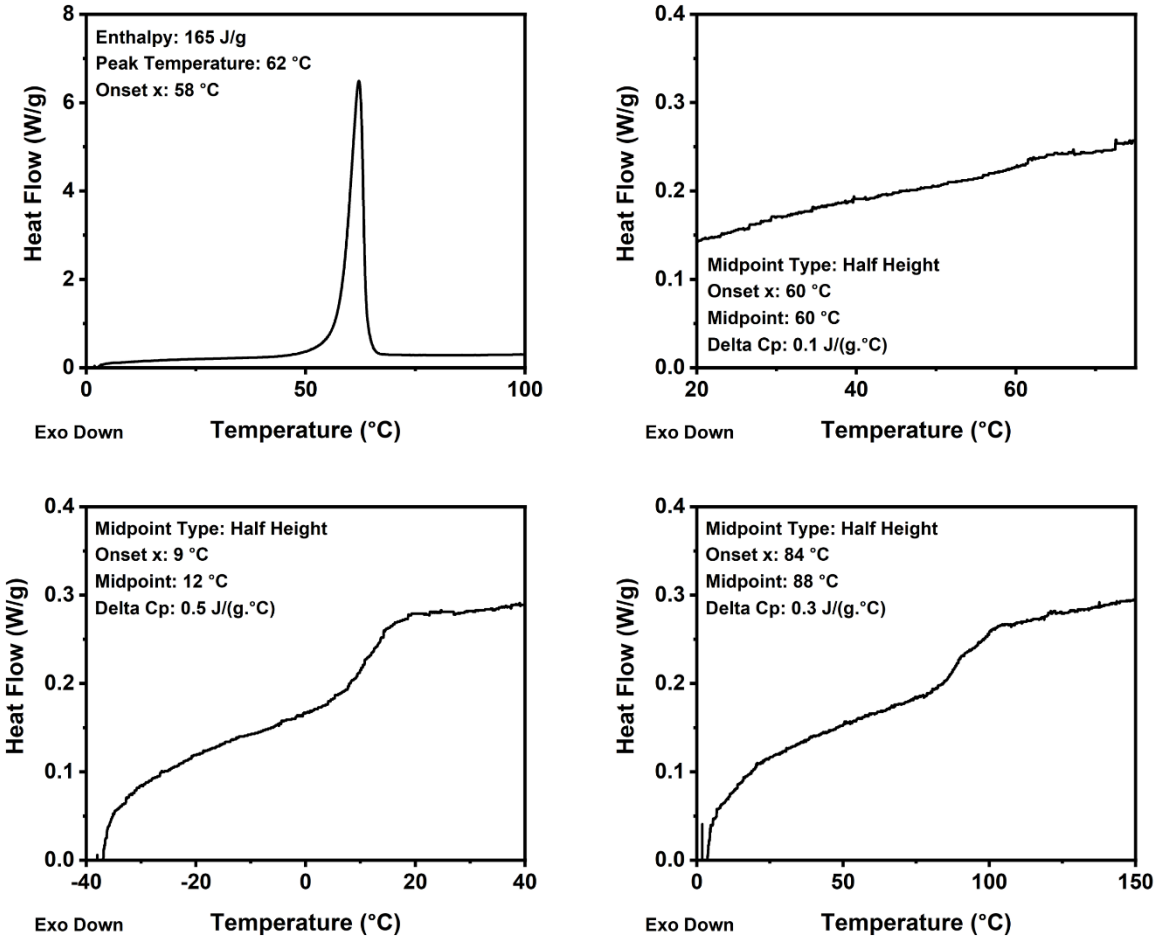

Figure 54. The DSC curves of printed architectures of PEO (top left), PMMA (top right), PPC (bottom left), and PS (bottom right) with 1.0% low regioregular P3HT.

The first scan of heating is used for the analysis of DSC data so that one can witness the thermal history of the material that it experienced during the printing process. Figure 51-54 show that there are three glass transition temperatures and one melting temperature in each set of printed architectures, which corresponds to the three amorphous polymers and semicrystalline one. Again, the glass transition of PMMA and PS are more gradual in comparison to PPC's.

Table 8. Transition temperatures for each blend of Matrix:P3HT

Variable	PPC	PS	PMMA	PEO
0.5% HR P3HT	7°C	98°C	60°C	63°C
0.5% LR P3HT	12°C	88°C	60°C	62°C
1.0% HR P3HT	17°C	96°C	60°C	63°C
1.0% LR P3HT	11°C	74°C	59°C	60°C

The inclusion of P3HT drastically impacts the glass transition temperature of PMMA which is probably due to the high miscibility between the two polymers. The strong interactions between them would greatly affect the thermodynamic properties. The varying concentrations as well as between high and low regioregular P3HT decreases the expected glass transition of PMMA which can also be attributed to the interactions between the polymers which are independent of the regioregularity. PPC and PS do show significant change between glass transition temperatures whilst varying concentration and regioregularity. This is most likely due to the unfavourable interactions between P3HT and these polymers. The PEO being semicrystalline like P3HT, the P3HT do not induce the decrease of the PEO crystallites melting temperature. There are only two outliers which include 0.5% P3HT with PPC where the low regioregular sample glass transition is larger than the high regioregular P3HT as well as 0.5% P3HT with PMMA as the high and low regioregular samples transition at the same temperature. In the case of PMMA, it can be related to how miscible PMMA and P3HT are. In relation to the 1.0% P3HT:PMMA samples, the difference between low and high regioregular tests is only 1°C, which is negligible. PPC has a higher transition temperature when low regioregular P3HT is used for the 0.5% samples but the inverse is seen when 1.0% P3HT is implemented. This again is most likely due to the cross-linked behaviour which would alter the thermodynamics for when P3HT is added into the matrix. In the range of temperatures that was scanned, there was no evidence of P3HT melting.

5.4.6 X-ray Diffraction

X-Ray diffraction patterns were analyzed to assess how the P3HT would impact the crystallinity of each matrix. The crystalline behaviour of a polymer may affect the final post-processed material which is of importance to device manufacturing.[62] Depending on the extent of crystallinity a polymer holds, the mechanical properties of the final processed device may be affected. In addition, the crystalline properties of a polymer may change how additives behave within the matrix—including P3HT. Thus, it is required that the printed architectures be observed under XRD to understand how P3HT may alter the crystallinity of the final post-processed material.

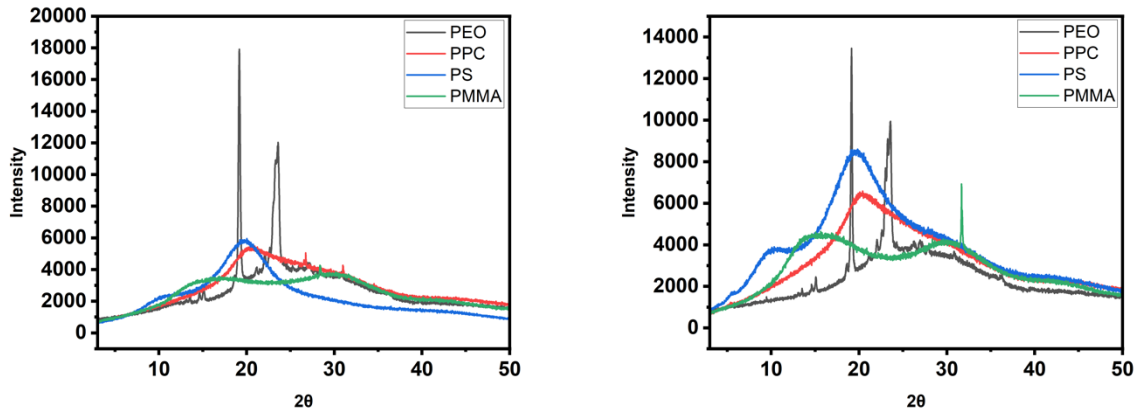

Figure 55. XRD patterns of 3D printed thermoplastic matrices with 1.0% regioregular P3HT. Left is high regioregular and right is low regioregular samples.

Figure 55 shows the XRD patterns for 1.0% high and low regioregular P3HT. Generally, the shape of each pattern of both high and low regioregular P3HT embedded in the matrices is unaltered from the P3HT. One peak appears in the PMMA matrix just over 30 2Θ in the low regioregular samples which is not a crystalline peak but a spike in the data as PMMA is the most amorphous sample with the highest miscibility with P3HT.

5.4.7 Optical Microscopy

Bright field and polarized optical microscopy were once again employed, in addition to epifluorescence microscopy to analyze on a macroscopic scale the phases in presence in the printed architectures. The combination between the three of these techniques allows for creating a visual perspective of the nature of P3HT in each matrix. Due to P3HT's semicrystalline and fluorescent nature, the polarized and fluorescent microscopy techniques may display how P3HT aggregates within a thermoplastic matrix.

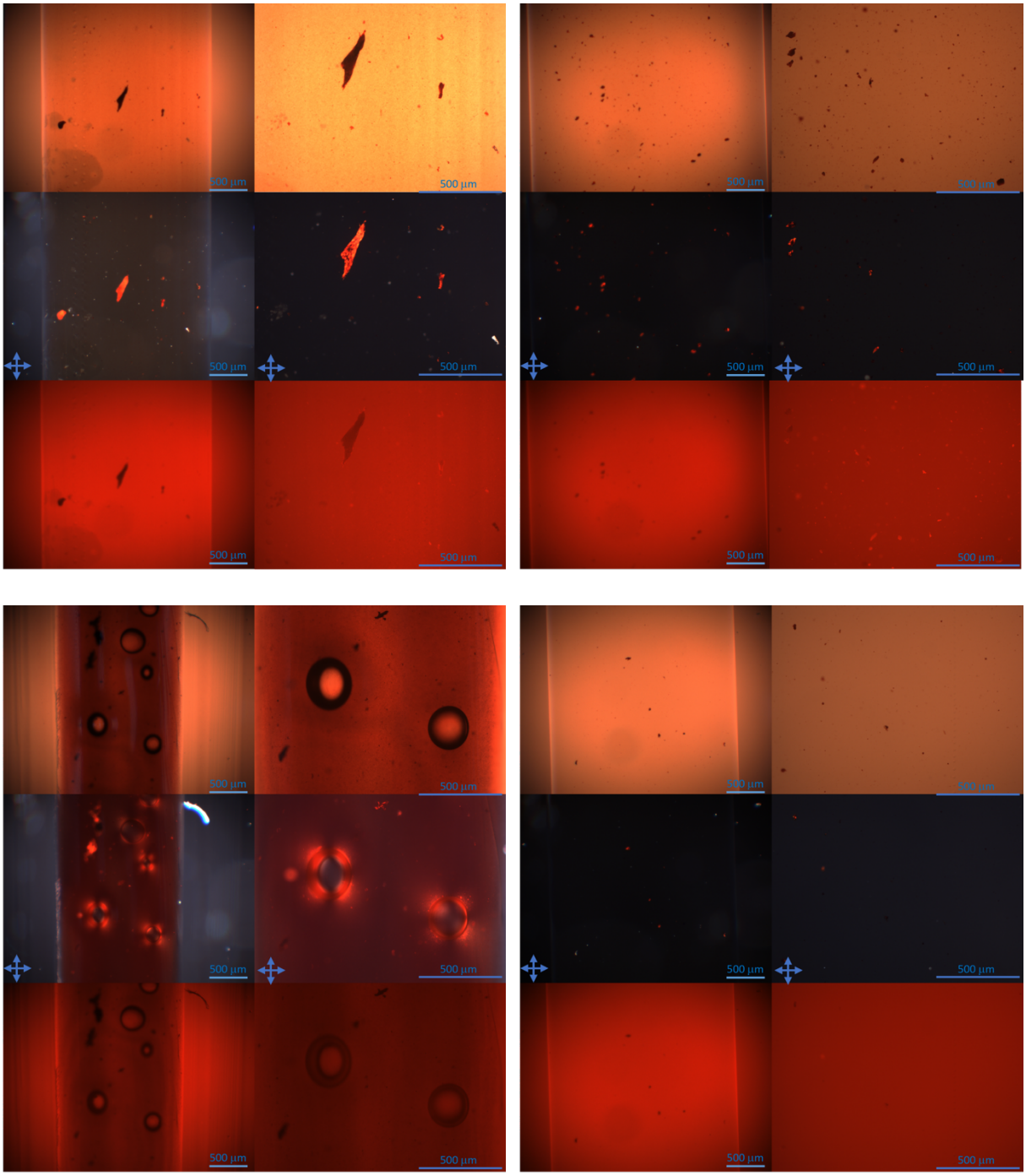

Figure 56. Optical microscope pictures of PMMA printed architectures. Top panels have 0.5% P3HT and the bottom have 1.0%. Left is low regioregular samples while the right is high regioregular. The left side within each of the four panels has a magnification of 5X and the right is 10X. Top pictures of the panels are bright field microscopy, middle pictures are cross polarized at 90° and the bottom pictures were completed with an epifluorescence filter.

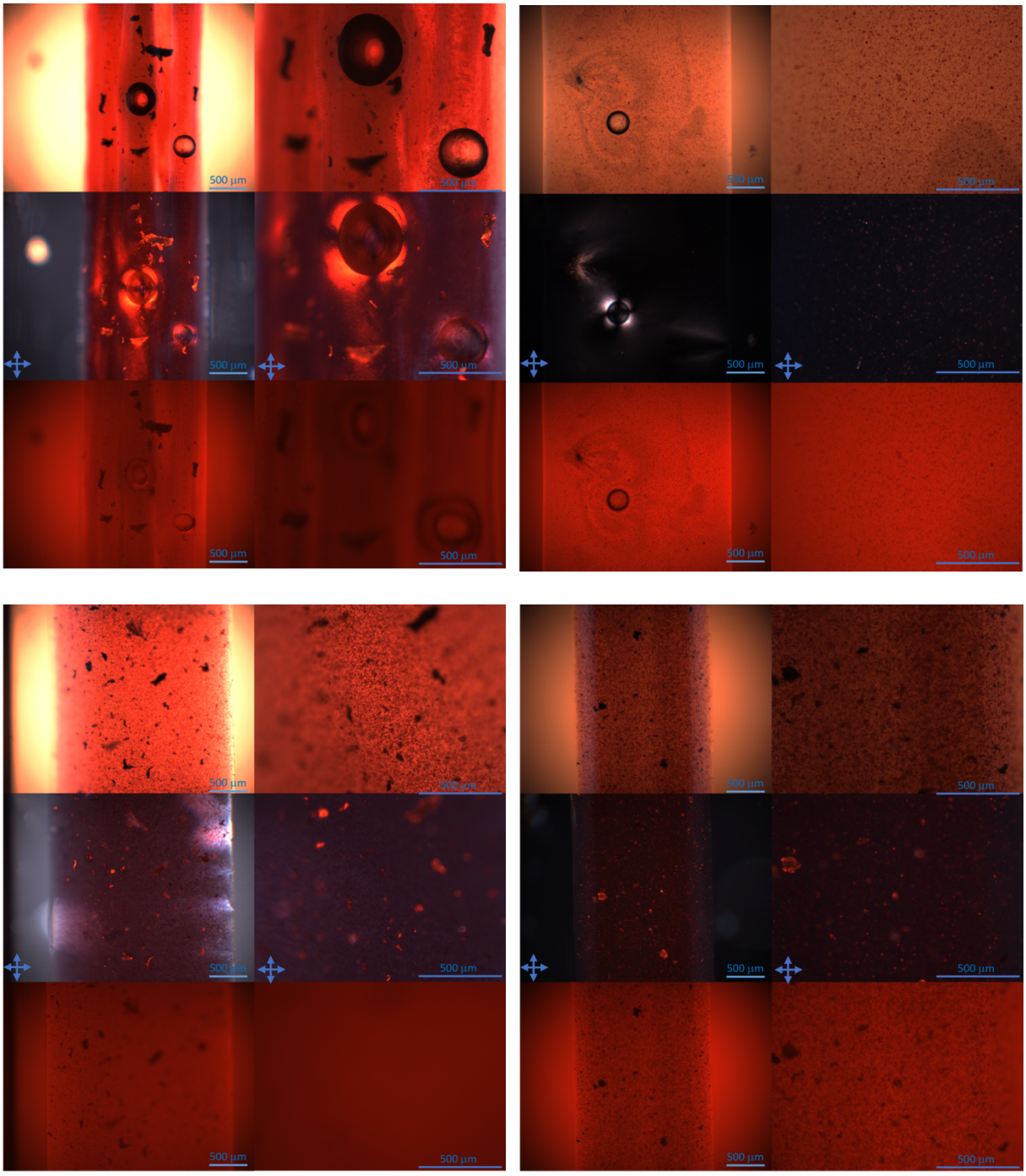

Figure 57. Optical microscope pictures of a PS printed architectures. Top panels have 0.5% P3HT and the bottom have 1.0%. Left is low regioregular samples while the right is high regioregular. The left side within each of the four panels has a magnification of 5X and the right is 10X. Top pictures pf the panels are bright field microscopy, middle pictures are cross polarized at 90° and the bottom pictures were completed with an epifluorescence filter.

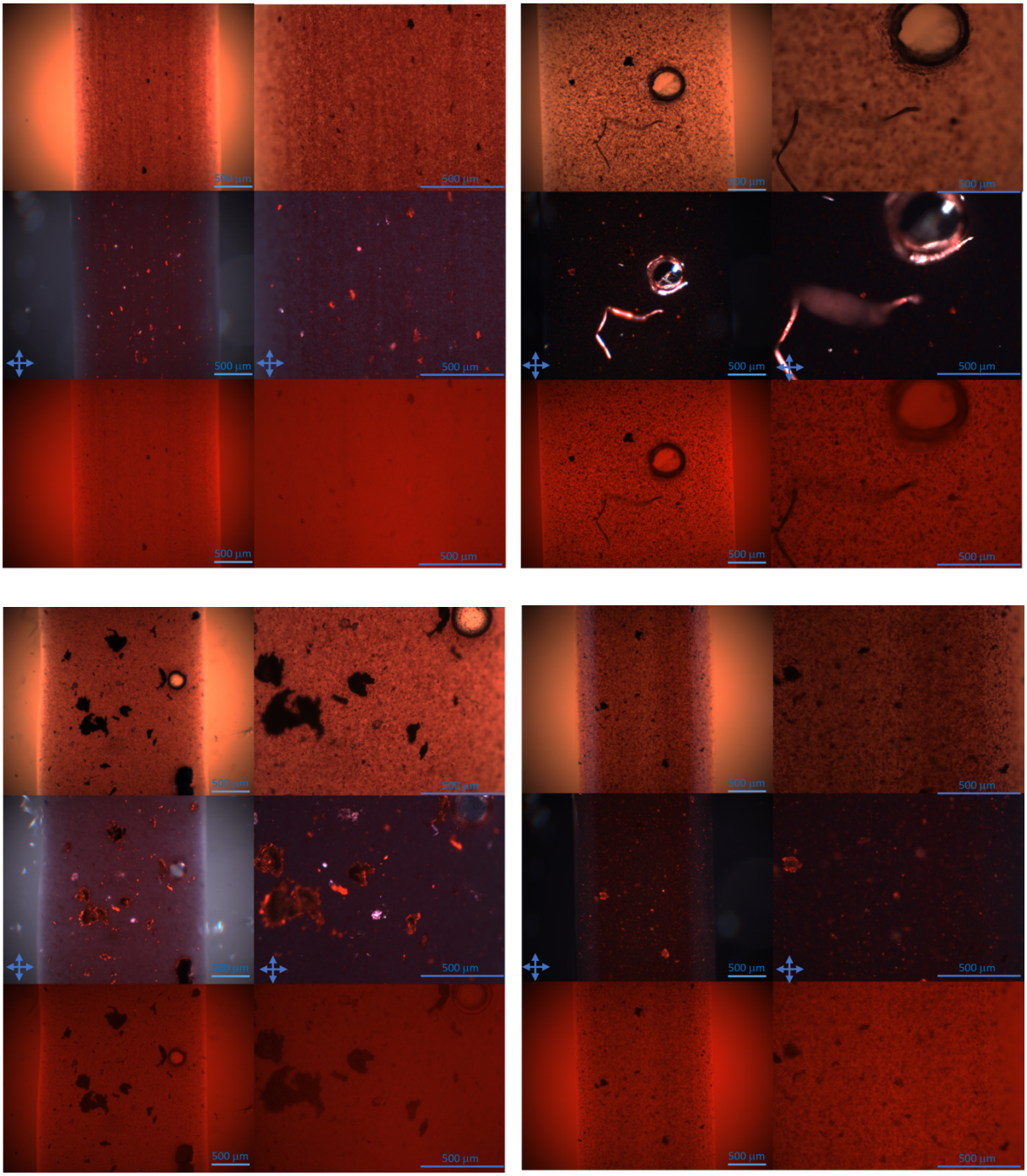

Figure 58. Optical microscope pictures of a PPC printed architectures. Top panels have 0.5% P3HT and the bottom have 1.0%. Left is low regioregular samples while the right is high regioregular. The left side within each of the four panels has a magnification of 5X and the right is 10X. Top pictures of the panels are bright field microscopy, middle pictures are cross polarized at 90° and the bottom pictures were completed with an epifluorescence filter.

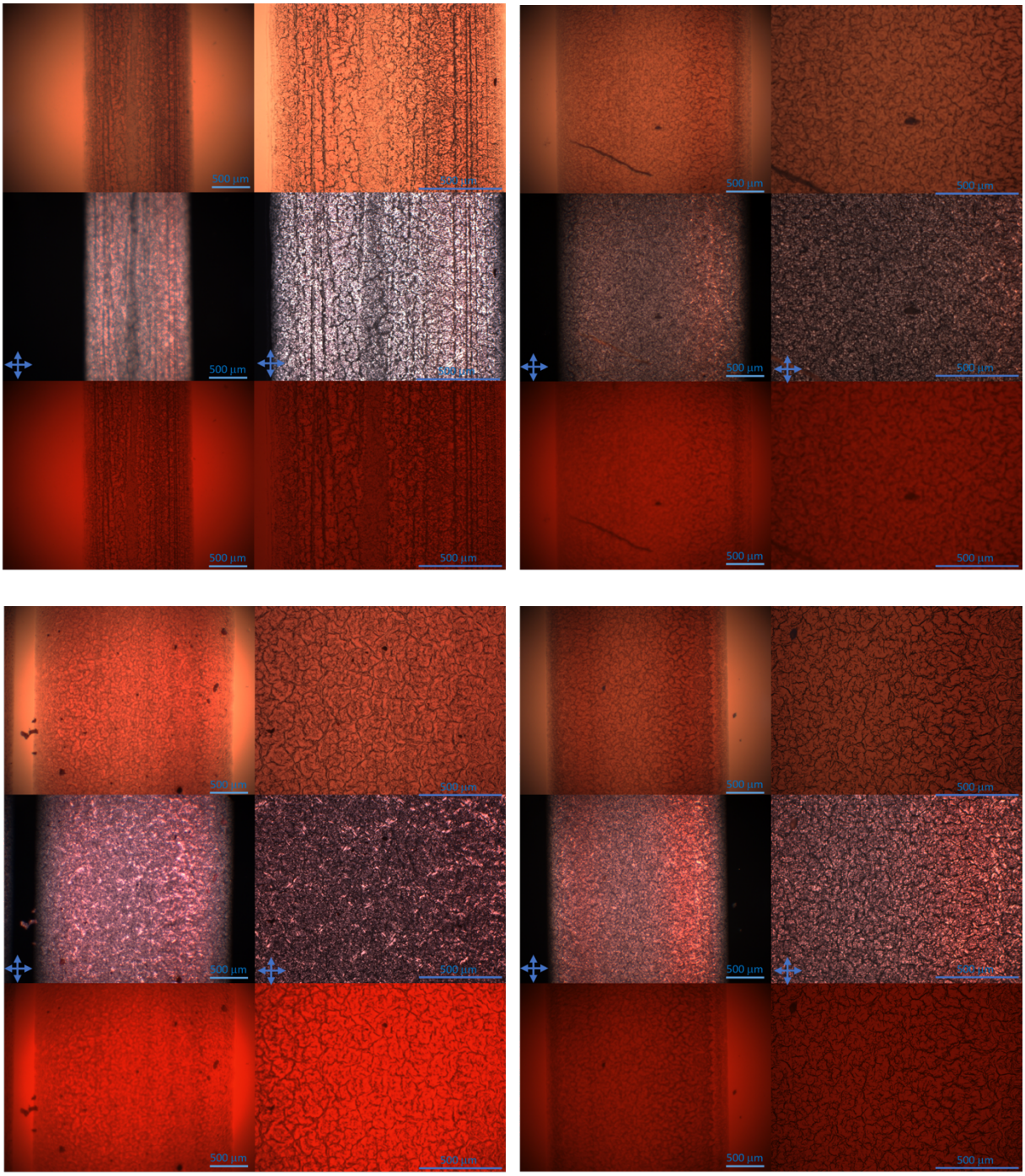

Figure 59. Optical microscope pictures of a PEO printed architectures. Top panels have 0.5% P3HT and the bottom have 1.0%. Left is low regioregular samples while the right is high regioregular. The left side within each of the four panels has a magnification of 5X and the right is 10X. Top pictures of the panels are bright field microscopy, middle pictures are cross polarized at 90° and the bottom pictures were completed with an epifluorescence filter.

For each pair of 0.5%, 1.0% high and low regioregular P3HT in the PMMA, PS, PPC, and PEO matrices, bright field, polarized, and epifluorescence microscope pictures were acquired and are displayed again. First, it should be noted that the varying thicknesses of each sample due to their varying solvent evaporation rates based on their affinity to chloroform may affect how bright the pictures appear. Overall, the PEO samples look significantly more textured in comparison to PMMA, PS, and PPC which is due to PEO's semicrystalline nature. In addition, P3HT aggregates are more noticeable in samples with the higher concentration of P3HT as well as the high regioregular samples when observing the bright field and polarized optical microscopy. This is consistent as low regioregular P3HT would be more miscible throughout the polymer. This is also the reason as to why P3HT aggregates are less noticeable in PMMA samples. The semicrystalline nature of PEO is confirmed by the textures it displays in its microscopy pictures in comparison to the three other amorphous polymers. For all samples, the epifluorescence pictures do not show much evidence of fluorescence from P3HT. This may be due to multiple reasons including the low percentage of P3HT used, the spreading of P3HT throughout the matrices and also the great thickness of the samples.

5.5 Conclusion

In this Chapter, the 3D printing of thermoplastics blended with two concentrations of two regioregular P3HT's was completed along with their printability, and phase separation behavior. In terms of the optoelectronic capabilities outlined by UV-vis and fluorescence spectroscopy, the results did not overly differ from the 2D counterparts. Indicating that the 3D processing of these materials would be just as electronically efficient as their 2D counterparts. Lamentably, the printability of the discussed inks was not within ideal values based on the calculated uniformity factors and contact angles. In the field of 3D processing this is a sacrifice one must deal with as these blends must be processed in solution. There is not a conceivable linear correlation between P3HT concentration of high or low regioregularity and their features of printability and transitions gathered from UV-vis and fluorescence spectroscopy. But it can be noted that based on this data, the author would recommend a blend between PS and low regioregular P3HT for the best printable and electronic properties. It should also be noted that PMMA is not recommended due to the high miscibility resulting in a lack of aggregation of P3HT.

Chapter 6 – Conclusion

In this work the analyses of optoelectronically active 3-dimensional architectures processed *via* direct-ink writing were completed. These analyses were conducted to understand the physical chemistry experienced by these formulations during the direct-ink writing process as little is understood to date and that it is needed because 3D printing is becoming ever more useful in processing futuristic devices. Initially, and as discussed in Chapter 4, the rheological properties and printability of the pristine thermoplastic matrices was studied. The inclusion of P3HT negligibly affected these properties as displayed in Chapter 5. Also in Chapter 5, the probing of the molecular organization and aggregation of P3HT embedded in the printed architectures was investigated. From this study it was found that polystyrene resulted in the best of the thermoplastics to process P3HT for both printability and optoelectronic capabilities. In addition, Chapter 2 introduced a part of a Roadmap on materials for energy harvesting technologies, which outlined a recent review of organic photovoltaics for indoor light conversion. This is of particular interest in combination with Chapters 4 and 5 as organic photovoltaics are concerned with the processing of conjugated polymers.

In Chapter 4 where the pristine matrices were analyzed, the thermoplastic which presented the best printable nature was the only semicrystalline polymer, PEO. This is considerably based on the comparison between the printed architectures uniformity factor. Originally it was also expected that the printability of PEO as well as the confinement that the semicrystalline nature of PEO when including P3HT would additionally result in the best electronic properties. Inherently, this was not the case. The work presented in Chapter 5 included the varying of concentrations of both high and low regioregular P3HT which were introduced into each of the matrices. This work resulted in the ideal combination being between PS and 1.0% low regioregular P3HT due to the printability combined with the optoelectronic factors. But the most compelling data from this work displayed that the electronic capabilities of the 3D printed architectures were very similar to the 2D films constructed from the same inks. This suggests that the direct-ink writing process does not inhibit the optoelectronic efficiencies.

From the work done in this thesis, it is expected that the $A_{0\text{-}0}/A_{0\text{-}1}$ or $I_{0\text{-}0}/I_{0\text{-}1}$ transitions would be directly related to the efficiency of a photoconductor constructed from these materials. In this work, a photoconductor was not constructed but for future considerations it would be simple to apply electrodes and a voltage to confirm this hypothesis, pending that the percolation ratio for P3HT is achieved. This would be a necessary study to conduct as it would be the beginning of forming optoelectronic devices *via* direct-ink writing.

For future works in this field, in may be perceivable to alter the additive manufacturing processing method in order to have better resolution and perhaps, better electronic properties. Studies by Boyer *et al*.[78] show the possibility of printing semicrystalline polymers by digital light processing where the structures displayed shape memory and strain-selective behaviour. In another article completed by Boyer *et al*.[79], they managed to use digital light processing to form conductive architectures by the developed technique of polymerization-induced microphase separation (PIMS). This approach allows for fine tuning of the mechanical and conductive properties independently. In this work, a rigid crosslinked, poly(isobornyl acrylate-*stat*-trimethylpropane triacrylate) provided the scaffold whilst the soft poly(oligoethylene glycol methyl ether acrylate) domains which 1-butyl-3-methylimidazolium bis-(trifluoromethyl sulfonyl)imide acted as an ionic liquid. Boyer *et al*. managed to produce this material into structures for energy storage applications with conductivities up to 1.2 mS cm^{-1} at 30°C. Based on the success seen in these past works, it can be noted that potentially trying other printing methods may be worth while to increase the resolution and conductivity of 3D architectures.

In addition to the 3D printing of an architecture suitable for a photoactive device, the analysis of P3HT embedded in the semicrystalline matrix, PEO, has led to further questions requiring probing. During the printing process, this specific solution undergoes a colour change from orange to purple presumably due to the experienced shear force. It has been noted in literature that the difference between orange and purple solutions of P3HT are conformational differences in the molecule that are respectively, dissolved polymer chains and aggregated P3HT.[80] This is noted as a visual measure that suggests the shear forces experienced during direct-ink writing have an effect on the supramolecular chemistry of the P3HT in solution. This system may then be further probed to discover the underlining factors that are causing such a change in

conformation. Therefore, UV-vis spectra of the solution before processing, combined with X-ray diffraction measurements conducted at the synchrotron during and after the extrusion process may be heavily investigated to explore the interactions experienced by the P3HT polymer during shearing.

References

(1) Qiu, Z.; Hammer, B. A. G.; Müllen, K. Conjugated Polymers – Problems and Promises. *Prog. Polym. Sci.* **2020**, *100*.

(2) Guo, X.; Baumgarten, M.; Müllen, K. Designing π-Conjugated Polymers for Organic Electronics. *Prog. Polym. Sci.* **2013**, *38* (12), 1832–1908.

(3) Forrest, S. R.; Thompson, M. E. Introduction: Organic Electronics and Optoelectronics. *Chem. Rev.* **2007**, *107* (4), 923–925.

(4) Meller, G.; Grasser, T. *Organic Electronics*, Springer, 2010; Vol. 223.

(5) Wu, W.; Bazan, G. C.; Liu, B. Conjugated-Polymer-Amplified Sensing, Imaging, and Therapy. *Chem* **2017**, *2* (6), 760–790.

(6) Heeger, A. J. Semiconducting Polymers: The Third Generation. *Chem. Soc. Rev.* **2010**, *39* (7), 2354–2371.

(7) Limonov, M. F.; Rybin, M. V.; Poddubny, A. N.; Kivshar, Y. S. Fano Resonances in Photonics. *Nat. Photonics* **2017**, *11* (9), 543–554.

(8) Moliton, A.; Hiorns, R. C. Review of Electronic and Optical Properties of Semiconducting π-Conjugated Polymers: Applications in Optoelectronics. *Polym. Int.* **2004**, *53* (10), 1397–1412.

(9) Bao, Z.; Dodabalapur, A.; Lovinger, A. J. Soluble and Processable Regioregular Poly(3-Hexylthiophene) for Thin Film Field-Effect Transistor Applications with High Mobility. *Appl. Phys. Lett.* **1996**, *69* (26), 4108–4110.

(10) Tremel, K.; Ludwigs, S. *P3HT Revisited – From Molecular Scale to Solar Cell Devices*, Springer, 2014; Vol. 265.

(11) Scharber, M. C.; Sariciftci, N. S. Low Band Gap Conjugated Semiconducting Polymers. *Adv. Mater. Technol.* **2021**, *6* (4), 2000857.

(12) Guo, X.; Facchetti, A. The Journey of Conducting Polymers from Discovery to Application. *Nat. Mater.* **2020**, *19* (9), 922–928.

(13) Braun, D. Semiconducting Polymer LEDs. *Mater. Today* **2002**, *5* (6), 32–39.

(14) Blakers, A. W.; Wang, A.; Milne, A. M.; Zhao, J.; Green, M. A. 22.8% Efficient Silicon Solar Cell. *Appl. Phys. Lett.* **1989**, *55* (13), 1363–1365.

(15) Wudl, F.; Kobayashi, M.; Heeger, A. J. Poly(Isothianaphthene). *J. Org. Chem.* **1984**, *49* (18), 3382–3384.

(16) Jortner, J. The Energy Gap Law for Non-Radiative Decay. *Molecular Physics* **1970**, *18* (2), 134–142.

(17) Gong, X.; Tong, M.; Xia, Y.; Cai, W.; Moon, J. S.; Cao, Y.; Yu, G.; Shieh, C. L.; Nilsson, B.; Heeger, A. J. High-Detectivity Polymer Photodetectors with Spectral Response from 300 nm to 1450 nm. *Science* **2009**, *325* (5948), 1665–1667.

(18) Rudenko, A. E.; Wiley, C. A.; Stone, S. M.; Tannaci, J. F.; Thompson, B. C. Semi-Random P3HT Analogs via Direct Arylation Polymerization. *J. Polym. Sci. Part A Polym. Chem.* **2012**, *50* (18), 3691–3697.

(19) Weiss, D. S.; Abkowitz, M. Advances in Organic Photoconductor Technology. *Chem. Rev.* **2010**, *110* (1), 479–526.

(20) Rogalski, A. Quantum Well Photoconductors in Infrared Detector Technology. *J. Appl. Phys.* **2003**, *93* (8), 4355–4391.

(21) Strohriegl, P.; Grazulevicius, J. V. Photoconductive Polymers. *Handb. Polym. Synth. Second Ed.* CRC Press, **2004**, 779–810.

(22) Baird, D. G. *Polymer Processing : Principles and Design*; John Wiley & Sons, 2014.

(23) Chhabra, R. P. Non-Newtonian Fluids: An Introduction. In *Rheology of Complex Fluids*; Krishnan, J. M., Deshpande, A. P., Kumar, P. B. S., Eds.; Springer New York: New York, NY, 2010; pp 3–34.

(24) Savagatrup, S.; Makaram, A. S.; Burke, D. J.; Lipomi, D. J. Mechanical Properties of Conjugated Polymers and Polymer-Fullerene Composites as a Function of Molecular Structure. *Adv. Funct. Mater.* **2014**, *24* (8), 1029–1181.

(25) Norrman, K.; Ghanbari-Siahkali, A.; Larsen, N. B. Studies of Spin-Coated Polymer Films. *Annu. Reports Prog. Chem. - Sect. C* **2005**, *101*, 174–201.

(26) Krebs, F. C. Fabrication and Processing of Polymer Solar Cells: A Review of Printing and Coating Techniques. *Sol. Energy Mater. Sol. Cells* **2009**, *93* (4), 394–412.

(27) Chang, C.; Pai, C.; Chen, W.; Jenekhe, S. A. Spin Coating of Conjugated Polymers for Electronic and Optoelectronic Applications. *Thin Solid Films* **2005**, *479*, 254–260.

(28) Tang, X.; Yan, X. Dip-Coating for Fibrous Materials: Mechanism, Methods and Applications. *J. Sol-Gel Sci. Technol.* **2017**, *81* (2), 378–404.

(29) Li, Q.; Yao, Z.; Lu, Y.; Zhang, S.; Ahmad, Z.; Wang, J.; Gu, X.; Pei, J. Achieving High Alignment of Conjugated Polymers by Controlled Dip-Coating. *Adv. Electron. Mater* **2020**, *6* (6), 2000080.

(30) Obregón, S.; Rodríguez-González, V. Photocatalytic TiO2 Thin Films and Coatings Prepared by Sol–Gel Processing: A Brief Review. *J. Sol-Gel Sci. Technol.* **2022**, *102* (1), 125–141.

(31) Dorling, B.; Vohra, V.; Dao, T. T.; Garriga, M.; Murata, H.; Compoy-Quiles, M. Uniaxial Macroscopic Alignment of Conjugated Polymer Systems by Directional Crystallization during Blade Coating. *J. Mater. Chem. C* **2014**, *2*, 3303–3310.

(32) Ye, L.; Xiong, Y.; Yao, H.; Gadisa, A.; Zhang, H.; Li, S.; Ghasemi, M.; Balar, N.; Hunt, A.; O'Connor, B. T.; et al. High Performance Organic Solar Cells Processed by Blade Coating in Air from a Benign Food Additive Solution. *Chem. Mater.* **2016**, *28* (20), 7451–7458.

(33) Ding, X.; Liu, J.; Harris, T. A. L. A Review of the Operating Limits in Slot Die Coating Processes. *AIChE J.* **2016**, *62* (7), 2508–2524.

(34) Patidar, R.; Burkitt, D.; Hooper, K.; Richards, D.; Watson, T. Slot-Die Coating of Perovskite Solar Cells: An Overview. *Mater. Today Commun.* **2020**, *22* (September 2019), 100808.

(35) Amb, C. M.; Craig, M. R.; Koldemir, U.; Subbiah, J.; Choudhury, K. R.; Gevorgyan, S. A.; Jørgensen, M.; Krebs, F. C.; So, F.; Reynolds, J. R. Aesthetically Pleasing Conjugated Polymer:Fullerene Blends for Blue-Green Solar Cells Via Roll-to-Roll Processing. *ACS Appl. Mater. Interfaces* **2012**, *4* (3), 1847–1853.

(36) Ligon, S. C.; Liska, R.; Stampfl, J.; Gurr, M.; Mülhaupt, R. Polymers for 3D Printing and Customized Additive Manufacturing. *Chem. Rev.* **2017**, *117* (15), 10212–10290.

(37) Singh, D. D.; Mahender, T.; Raji Reddy, A. Powder Bed Fusion Process: A Brief Review. *Mater. Today Proc.* **2021**, *46*, 350–355.

(38) Jordan, R. S.; Wang, Y. 3D Printing of Conjugated Polymers. *J. Polym. Sci. Part B Polym. Phys.* **2019**, *57* (23), 1549–1644.

(39) Wu, Y.; Chen, Y. X.; Yan, J.; Yang, S.; Dong, P.; Soman, P. Fabrication of Conductive Polyaniline Hydrogel Using Porogen Leaching and Projection Microstereolithography. *J. Mater. Chem. B* **2015**, *3* (26), 5352–5360.

(40) Pagac, M.; Hajnys, J.; Ma, Q.; Jancar, L.; Jansa, J.; Stefek, P.; Mesicek, J. A Review of Vat Photopolymerization Technology: Materials, Applications, Challenges, and Future Trends of 3D Printing. *Polymers (Basel).* **2021**, *13* (4), 598.

(41) Ullsperger, T.; Wencke, Y. L.; Yürekli, B.; Matthäus, G.; Rettenmayr, M.; Luinstra, G. A.; Nolte, S. Laser Powder Bed Fusion of Ultra-High Molecular Weight Polyethylene (UHMWPE) Using near-Infrared Ultrashort Laser Pulses. *Mater. Des.* **2021**, *210*, 1–12.

(42) Kritchman, E. M.; Zeytoun, L. (Objet Geometries Ltd.) Rapid Prototyping Apparatus. U.S. Patent 7896639, 2011.

(43) Gordon, T. J.; Yu, J.; Yang, C.; Holdcroft, S. Direct Thermal Patterning of a π-Conjugated Polymer. *Chem. Mater.* **2007**, *19* (9), 2155–2161.

(44) Saadi, M. A. S. R.; Maguire, A.; Pottackal, N. T.; Thakur, M. S. H.; Ikram, M. M.; Hart, A. J.; Ajayan, P. M.; Rahman, M. M. Direct Ink Writing: A 3D Printing Technology for Diverse Materials. *Adv. Mater.* **2022**, *34* (28) 2108855.

(45) Li, V. C.; Dunn, C. K.; Zhang, Z.; Deng, Y.; Qi, H. J. Direct Ink Write (DIW) 3D Printed Cellulose Nanocrystal Aerogel Structures. *Sci. Rep.* **2017**, *7*, 8018.

(46) Chortos, A. Extrusion 3D Printing of Conjugated Polymers. *J. Polym. Sci.* **2022**, *60* (3), 486–503.

(47) Dominguez-alfaro, A.; Gabirondo, E.; Alegret, N.; De Leon-Almazan, C. M.; Hernandez, R.; Vallejo-illarramendi, A.; Prato, M.; Mecerreyes, D. 3D Printable Conducting and Biocompatible PEDOT- Graft -PLA Copolymers by Direct Ink Writing. *Macromol. Rapid Commun.* **2021**, *42* (12), 1–8.

(48) Liu, W.; Wang, C.; Chen, Q.; Ding, J.; Zhu, G. Direct Writing of Aligned Conjugated Polymer Micro-Ribbons for High-Performance Organic Electronics. *ACS Appl. Electron. Mater.* **2023**, *5* (2), 1131–1139.

(49) Holness, F. B.; Price, A. D. Direct Ink Writing of 3D Conductive Polyaniline Structures and Rheological Modelling. *Smart Mater. Struct.* **2018**, *27* (1), 015006.

(50) Schwab, A.; Levato, R.; D'Este, M.; Piluso, S.; Eglin, D.; Malda, J. Printability and Shape Fidelity of Bioinks in 3D Bioprinting. *Chem. Rev.* **2020**, *120* (19), 11028–11055.

(51) Soltan, N.; Ning, L.; Mohabatpour, F.; Papagerakis, P.; Chen, X. Printability and Cell Viability in Bioprinting Alginate Dialdehyde- Gelatin Scaffolds. *ACS Biomater. Sci. Eng* **2019**, *5*, 2976–2987.

(52) Hartmann, L.; Tremel, K.; Uttiya, S.; Crossland, E.; Ludwigs, S.; Kayunkid, N.; Vergnat, C.; Brinkmann, M. 2D Versus 3D Crystalline Order in Thin Films of Regioregular Poly(3-Hexylthiophene) Oriented by Mechanical Rubbing and Epitaxy. *Adv. Funct. Mater.* **2011**, *21*, 4047–4057.

(53) Lee, Y.; Mongare, A.; Plant, A.; Ryu, D. Strain–Microstructure–Optoelectronic Inter-Relationship toward Engineering Mechano-Optoelectronic Conjugated Polymer Thin Films. *Polymers (Basel).* **2021**, *13* (6), 935.

(54) Persson, N. E.; Chu, P.; Mcbride, M.; Grover, M.; Reichmanis, E. Nucleation, Growth, and

Alignment of Poly(3-Hexylthiophene) Nanofibers for High-Performance OFETs. *Acc. Chem. Res.* **2017**, *50*, 932–942.

(55) Maleki, A.; Seidali, Z.; Zakerhamidi, M. S.; Ara, M. H. M. Dichroic Ratio and Order Parameters of Some Sudan Dyes Doped in Nematic Liquid Crystalline Matrix. *Optik (Stuttg).* **2015**, *126* (24), 5473–5477.

(56) Engel, T. *Quantum Chemistry and Spectroscopy Fourth Edition*, Pearson, 2019.

(57) Kundu, S.; Roy, P. P.; Fleming, G. R.; Makri, N. Franck − Condon and Herzberg − Teller Signatures in Molecular Absorption and Emission Spectra. *J. Phys. Chem. B* **2022**, *126*, 2899–2911.

(58) Herman, B. Fluorescence Microscopy. *Curr. Protoc. Cell Biol.* **2002**, 1–10.

(59) Jakubek, Z. J.; Chen, M.; Martinez Rubi, Y.; Simard, B.; Zou, S. Conformational Order in Aggregated Rra-P3HT as an Indicator of Quality of Boron Nitride Nanotubes. *J. Phys. Chem. Lett.* **2020**, *11* (10), 4179–4185.

(60) Dudenko, D.; Kiersnowski, A.; Shu, J.; Pisula, W.; Sebastiani, D.; Spiess, H. W.; Hansen, M. R. A Strategy for Revealing the Packing in Semicrystalline P-Conjugated Polymers: Crystal Structure of Bulk Poly-3-Hexyl-Thiophene (P3HT). *Angew. Chemie* **2012**, *124* (44), 11230–11234.

(61) Mahmood, A.; Wang, J. A Review of Grazing Incidence Small- and Wide-Angle X-Ray Scattering Techniques for Exploring the Film Morphology of Organic Solar Cells. *Sol. RRL* **2020**, *4* (10), 1–39.

(62) Goffri, S.; Muller, C.; Stingelin-stutzmann, N.; Breiby, D. W.; Radano, C. P.; Andreasen, J. W.; Thompson, R.; Janssen, R. A. J.; Neilsen, M. M.; Smith, P.; et al. Multicomponent Semiconducting Polymer Systems with Low Crystallization-Induced Percolation Threshhold. *Nat. Mater.* **2006**, *5*, 950–956.

(63) Chang, M.; Choi, D.; Wang, G.; Kleinhenz, N.; Persson, N.; Park, B.; Reichmanis, E. Photoinduced Anisotropic Assembly of Conjugated Polymers in Insulating Polymer Blends.

ACS Appl. Mater. Interfaces **2015**, *7* (25), 13723–14164.

(64) Choi, D.; Kim, H.; Persson, N.; Chu, P.; Chang, M.; Kang, J.; Graham, S.; Reichmanis, E. Elastomer − Polymer Semiconductor Blends for High-Performance Stretchable Charge Transport Networks. *Chem. Mater.* **2016**, *28* (4), 1003–1244.

(65) Jiang, Y.; Wang, X.; Plog, J.; Yarin, A. L.; Pan, Y. Electrowetting-Assisted Direct Ink Writing for Low-Viscosity Liquids. *J. Manuf. Process.* **2021**, *69*, 173–180.

(66) Lianyong, S.; Zhide, H.; Hua, Y.; Jun, D.; Hansong, Z. Study on Degradable Materials Poly(Propylene Carbonate) and Poly(Lactic Acid): Solubility Parameters and Compatibility. *Mater. Reports* **2018**, *32* (22), 3948-3953 .

(67) Gu, X.; Shaw, L.; Gu, K.; Toney, M. F.; Bao, Z. The Meniscus-Guided Deposition of Semiconducting Polymers. *Nat. Commun.* **2018**, *9* (1), 534.

(68) Zhang, J.; Tan, H. S.; Guo, X.; Facchetti, A.; Yan, H. Material Insights and Challenges for Non-Fullerene Organic Solar Cells Based on Small Molecular Acceptors. *Nat. Energy* **2018**, *3*, 720–731.

(69) Cheng, P.; Li, G.; Zhan, X.; Yang, Y. Next-Generation Organic Photovoltaics Based on Non-Fullerene Acceptors /639/301/299/946 /639/624/399 Review-Article. *Nat. Photonics* **2018**, *12* (3), 131–142.

(70) Hou, J.; Inganas, O.; Friend, R. H.; Gao, F. Organic Solar Cells Based on Non-Fullerene Acceptors. *Nat. Mater.* **2018**, *17* (2), 119–128.

(71) Mathews, I.; Kantareddy, S. N.; Buonassisi, T.; Peters, I. M. Technology and Market Perspective for Indoor Photovoltaic Cells. *Joule* **2019**, *3* (6), 1415–1426.

(72) You, Y. J.; Song, C. E.; Hoang, Q. V.; Kang, Y.; Goo, J. S.; Ko, D. H.; Lee, J. J.; Shin, W. S.; Shim, J. W. Highly Efficient Indoor Organic Photovoltaics with Spectrally Matched Fluorinated Phenylene-Alkoxybenzothiadiazole-Based Wide Bandgap Polymers. *Adv. Funct. Mater.* **2019**, *29* (27), 1901171.

(73) Shin, S. C.; Koh, C. W.; Vincent, P.; Goo, J. S.; Bae, J. H.; Lee, J. J.; Shin, C.; Kim, H.; Woo, H.

Y.; Shim, J. W. Ultra-Thick Semi-Crystalline Photoactive Donor Polymer for Efficient Indoor Organic Photovoltaics. *Nano Energy* **2019**, *58*, 466–475.

(74) Cui, Y.; Wang, Y.; Bergqvist, J.; Yao, H.; Xu, Y.; Gao, B.; Yang, C.; Zhang, S.; Inganäs, O.; Gao, F.; et al. Wide-Gap Non-Fullerene Acceptor Enabling High-Performance Organic Photovoltaic Cells for Indoor Applications. *Nat. Energy* **2019**, *4* (9), 768–775.

(75) Dayneko, S. V.; Pahlevani, M.; Welch, G. C. Indoor Photovoltaics: Photoactive Material Selection, Greener Ink Formulations, and Slot-Die Coated Active Layers. *ACS Appl. Mater. Interfaces* **2019**, *11* (49), 46017–46025.

(76) Tintori, F.; Laventure, A.; Koenig, J. D. B.; Welch, G. C. High Open-Circuit Voltage Roll-to-Roll Compatible Processed Organic Photovoltaics. *J. Mater. Chem. C* **2020**, *8* (38), 13430–13438.

(77) Osterwald, C. R. Translation of Device Performance Measurements to Reference Conditions. *Solar Cells*. 1986, pp 269–279.

(78) Rylski, A. K.; Maraliga, T.; Wu, Y.; Recker, E. A.; Arrowood, A. J.; Sanoja, G. E.; Page, Z. A. Digital Light Processing 3D Printing of Soft Semicrystalline Acrylates with Localized Shape Memory and Stiffness Control. *ACS Appl. Mater. Interfaces* **2023**, *15* (28), 34097–34107.

(79) Melodia, D.; Bhadra, A.; Lee, K.; Kuchel, R.; Kundu, D.; Corrigan, N.; Boyer, C. 3D Printed Solid Polymer Electrolytes with Bicontinuous Nanoscopic Domains for Ionic Liquid Conduction and Energy Storage. *Small* **2023**, 2206639.

(80) Oh, J. Y.; Shin, M.; Lee, T. Il; Jang, W. S.; Min, Y.; Myoung, J.; Baik, H. K.; Jeong, U. Self-Seeded Growth of Poly(3-Hexylthiophene) (P3HT) Nanofibrils by a Cycle of Cooling and Heating in Solutions. *Macromolecules* **2012**, *45* (18), 7504–7513.